ΕΘΝΙΚΟ ΜΕΤΣΟΒΙΟ ΠΟΛΥΤΕΧΝΕΙΟ

ΣΧΟΛΗ ΕΦΑΡΜΟΣΜΕΝΩΝ ΜΑΘΗΜΑΤΙΚΩΝ ΚΑΙ ΦΥΣΙΚΩΝ ΕΠΙΣΤΗΜΩΝ

ΣΧΟΛΗ ΜΗΧΑΝΟΛΟΓΩΝ ΜΗΧΑΝΙΚΩΝ

ΕΚΕΦΕ «ΔΗΜΟΚΡΙΤΟΣ»

ΙΝΣΤΙΤΟΥΤΟ ΝΑΝΟΕΠΙΣΤΗΜΗΣ ΚΑΙ ΝΑΝΟΤΕΧΝΟΛΟΓΙΑΣ

ΙΝΣΤΙΤΟΥΤΟ ΠΥΡΗΝΙΚΗΣ ΚΑΙ ΣΩΜΑΤΙΔΙΑΚΗΣ ΦΥΣΙΚΗΣ

Διατμηματικό Πρόγραμμα Μεταπτυχιακών Σπουδών

«Φυσική και Τεχνολογικές Εφαρμογές»

Χαρακτηρισμός ανιχνευτών πυριτίου για την αναβάθμιση στη φάση 2 του ανιχνευτή Τροχιών του πειράματος CMS

ΜΕΤΑΠΤΥΧΙΑΚΗ ΔΙΠΛΩΜΑΤΙΚΗ ΕΡΓΑΣΙΑ

του

Παναγιώτη Ασσιούρα

Ερευνητικός Επιβλέπων:	Ακαδημαϊκός Επιβλέπων:
Δημήτρης Λουκάς Ινστιτούτο Πυρηνικής και Σωματιδιακής Φυσικής, Ε.Κ.Ε.Φ.Ε. «Δημόκριτος»	Σταύρος Μαλτέζος Τομέας Φυσικής, ΣΕΜΦΕ, Ε.Μ.Π.

Αθήνα, Ιούνιος, 2017

NATIONAL TECHNICAL UNIVERSITY OF ATHENS

SCHOOL OF APPLIED MATHEMATICS AND PHYSICS

SCHOOL OF MECHANICAL ENGINEERING

NCSR «DEMOKRITOS»

INSTITUTE OF NANOSCIENCE AND NANOTECHNOLOGY

INSTITUTE OF NUCLEAR AND PARTICLE PHYSICS

Interdisciplinary Postgraduate Programme

«Physics and Technological Applications»

Characterization of silicon detectors for the phase II upgrade of the CMS experiment of LHC

MASTER THESIS

of

Panagiotis Assiouras

Research Supervisor:	Academic Supervisor:
Demitris Loukas Institute of Nuclear and Particle Physics, N.C.S.R «Demokritos»	Stavros Maltezos Faculty of Physics, School of Applied Mathematics and Physics, N.T.U.A

Athens, June, 2017

National Technical University of Athens
/ National Scientific Center of Research Demokritos
School of Applied Mathematics and Physics
Faculty of Physics

Characterization of Silicon detectors for the phase II upgrade of the CMS experiment of LHC

Master Thesis

of

Assiouras Panagiotis

Εγκρίθηκε από την τριμελή εξεταστική επιτροπή

(Υπογραφή)	*(Υπογραφή)*	*(Υπογραφή)*
.....	.....	.....
Δημήτρης Λουκάς	Θεόδωρος Αλεξόπουλος	Σταύρος Μαλτέζος
Διευθυντής Ερευνών , Ε.Κ.Ε.Φ.Ε Δημόκριτος	Καθηγητής Ε.Μ.Π.	Αναπληρωτής Καθηγητής Ε.Μ.Π.

Acknowledgements

Για την διεκπεραίωση της διπλωματικής μου εργασίας θα ήθελα να ευχαριστήσω τον Διευθυντή Ερευνών του ΕΚΕΦΕ «Δημόκριτος» Δημήτρη Λουκά για την ανάθεση αυτής της μεταπτυχιακής εργασίας και για την καθοδήγηση και στήριξη του κατά την διάρκεια εκπόνησης της. Επίσης θα ήθελα να ευχαριστήσω τον Γιάννη Καζά για τη βοήθεια του και για το χρόνο που αφιέρωσε στα πλαίσια εκπόνησης τηςεργασίας.

Τέλος, θα ήθελα να ευχαριστήσω τα μέλη της τριμελής επιτροπής, τον αν. καθηγητή του Ε.Μ.Π. Σταύρο Μαλτέζο και τον καθηγητή Θεόδωρο Αλεξόπουλο για την υποστήριξη τους.

Περίληψη

Το Compact Muon Solenoid, είναι ένας από τους δύο μεγάλους ανιχνευτές γενικής χρήσης που συνέβαλαν στην πρόσφατη ανακάλυψη του μποζόνιου Higgs καθώς και πολλές αλλές μελέτες στο κομάτι της σωματιδιακής φυσικής . Το εσωτερικό τμήμα του CMS ονομάζεται Tracker και είναι ένας ανιχνευτής πολύ υψηλής ακριβείας που μετρά τις τροχιές των σωματιδίων που δημιουργούνται απο τις συγκρούσεις του LHC. Αποτελείται από ανιχνευτές πυριτίου με υψηλή χωρική διακριτική ικανότητα και πολυ υψηλούς ρυθμούς απόκρισης ($< 20nsec$). Με συνολική επιφάνεια άνω των 200 τετραγωνικών μέτρών, είναι η μεγαλύτερη συσκευή τέτοιου είδους του που φτιάχτηκε ποτέ.

Η αύξηση της στιγμιαίας φωτεινότητας στον αναβαθμισμένο LHC θα οδηγήσει σε πολύ υψηλή αυξημένη πυκνότητα σωματιδίων καθώς επίσης σε ένα πολύ πιο απαιτητικό περιβάλλον από πλευράς ακτινοβολίας. Κατά συνέπεια, ο ανιχνευτής τροχιών του CMS θα χρειασθεί μια σημαντική αναβάθμιση και επανασχεδιασμό των αισθητήρων και των εξωτερικών ηλεκτρονικών συσκευών ανάγνωσης. Καθώς οι ανιχνευτές που έχουν εγκατασταθεί στα πρώτα στάδια της λειτουργίας του LHC δεν έχουν επαρκή αντοχή στην ακτινοβολία και δεν μπορούν να ανταποκριθούν με υψηλή ακρίβεια στο νέο απαιτητικό περιβάλλον. Οι αναβαθμίσεις θα γίνουν σε 2 φάσεις και ο αναβαθμισμένος LHC αναμένεται να είναι πλήρως λειτουργικός το 2026. Μετά τις αναβαθμίσεις θα λειτουργήσει για 10 χρόνια με φωτεινότητα που αναμένεται να φτάσει τα $3000 fb^{-1}$. Η αναβάθμιση φάσης 1 έχει ήδη πραγματοποιηθεί με την αντικατάσταση του εσωτερικού ανιχνευτή Pixel του CMS tarcker. Στη φάση 2 θα υπάρξουν σημαντικές αλλαγές στον εσωτεικό και στο εξωτερικο τμήμα του Tracker. Το εξωτερικό τμήμα αναμένεται να υπάρξουν 2 νέες μονάδες που ονομάζονται 2S και PS. Αυτοι οι ανιχνευτές θα έχουν 2 αισθητήρες σε πολύ μικρή απόσταση μεταξύ τους με ανιχνευτές strip (2S) και με ανιχνευτές strip και pixel (PS).Οι ανιχνευτές αυτοί θα έχουν την δυνατότητα να διακρίνουν γεγονοτα που είναι ιδιαίτερα σημαντικά απο πλευρά φυσικής με κατάλληλη συσχέτιση των γεγονότων η οποία μπορεί να δώσει πληροφορίες γα την εγκάρσια ορμή των σωματιδίων.

Για το λόγο αυτό ξεκίνησε μια μεγάλη εκστρατεία έρευνας και ανάπτυξης $R\&D$ από το CMS για τον προσδιορισμό του βέλτιστου σχεδιασμού ανιχνευτών με ιδιαίτερα αυξημένη αντοχή στην ακτινοβολία του μελλοντικού CMS Tracker.

Το κύριο μέρος αυτής της εργσιάς είναι ο ηλεκτρικός χαρακτηρισμός μικρών αισθητήρων και τέστ δομών από τα πρώτα πρωτότυπα wafers των 2S και PS μονάδων του εξωτερικού Tracker του CMS . Ο ηλεκτρικός χαρακτηρισμός αποτελεί σημαντικό μέρος του προγράμματος διασφάλισης ποιότητας του CMS. Προκειμένου να βρεθούν οι βέλτιστες γεωμετρίες και τα υλικά με τα οποία οι ανιχνευτές αυτοί θα καταφέρουν να ανταπεξέλθουν στις αυξημένες απαιτήσεις της αναβάθμισης του LHC.

Στο κεφάλαιο 1 γίνεται μια σύντομη εισαγωγή στη φυσική των ημιαγωγών και τα βασικά δομικά στοιχεία που χρησιμοποιούνται στους ανιχνευτές πυριτίου.

Στο Κεφάλαιο 2 γίνεται μια περιγραφή του LHC και του πειράματος CMS και των αναβαθμίσεων που θα ακολουθήσουν.

Στο Κεφάλαιο 3 γίνεται περιγραφή των βασικών χαρακτηριστικών των ανιχνευτών πυριτίου που χρησιμοποιούνται στη φυσική υψηλών ενεργειών.

Στο κεφάλαιο 4 παρουσιάζονται τα πειραματικά αποτελέσματα του ηλεκτρικού χαρακτηρισμού των δοκιμαστικών δομών και των μίνι αισθητήρων που έχει πραγματοποιηθεί στο εργαστήριο οργανολογίας ανιχνευτών του ΕΚΕΦΕ Δημόκριτος.

Abstract

The Large Hadron Collider at the European Council for Nuclear Research in Geneva is scheduled to undergo a major luminosity upgrade after its lifetime of ten years of operation,in order to maximize its scientific discovery potential. The total integrated luminosity will be increased by a factor of ten, which will dramatically change the conditions under which the four large detectors at the LHC will have to operate.

The Compact Muon Solenoid, is one of the two large general purpose detectors which has contributed to the recent discovery of the Higgs boson and many other physics results in particle physics. Its innermost part is called Tracker and it is a high- precision instrument that measures the created particles trajectories. It is composed of silicon detectors with high spatial resolution and rate capabilities. With a total surface of more than 200 square meters it is the largest device of its kind ever built.

The increase in instantaneous luminosity in the upgraded LHC will lead to very high increased track density at the interaction points of the colliding beams and thus also to a much more hostile radiation environment. As a consequence, the tracker of CMS will require a major upgrade and redesign of the sensors and read-out electronics, as the components installed at present do not have sufficient granularity and radiation tolerance. The upgrades will be done in 2 phases and the upgraded LHC is expected to be fully operational in 2026. After the upgrades it will operate for 10 years with a luminosity that is expected to reach $3000 fb^{-1}$. The Phase 1 upgrade has already been performed with the replacement of the inner Pixel Detector of the CMS tracker In Phase-2 there will be major changes in Inner Pixel Detector and the Outer Tracking system with new modules. The Outer Tracker is expected to have 2 new modules that is called 2S and PS module. This modules will have 2 very closely spaced sensors with strip detectors (2S) and with strip and pixel detectors (PS) and they will require discrimination logic of keeping the most interesting physics results depending of the longitudinal momentum of traversing particles.

An extensive $R\&D$ campaign has therefore been started by the CMS collaboration to identify radiation-hard silicon substrates and sensor technologies that could be implemented in the future tracker.

Electrical characterization of mini sensors and test strictures of the first prototype wafers of the 2S and PS module of the Outer Tracker of CMS has been performed. The Electrical characterization is an essential part of the quality assurance program of the CMS. In order to identify the geometries and the materials that fulfill the demanding requirements

In chapter 1 a brief introduction in the semiconductor physics and the basic building blocks that are used in silicon detectors is made.

Chapter 2 gives a description of the LHC and CMS experiment and the upgrades that CMS

tracker will undergo in order to operate with high efficiency in the harsh environment after the upgrade.

In Chapter 3 the basic characteristics of the silicon detectors that are used in high energy physics are discussed.

In Chapter 4 experimental results are shown of the Electrical characterization of test -structures and mini sensors that have been performed at laboratory of detector instrumentation of NCSR Demokritos.

Contents

Περίληψη 3

Abstract 5

Contents 8

1 Basic semiconductor properties and devices 9
- 1.1 Introduction . . . 9
- 1.2 Semiconductor Physics . . . 9
  - 1.2.1 Energy Bands . . . 10
  - 1.2.2 Intrinsic Semiconductors . . . 13
- 1.3 Extrinsic Semiconductor . . . 14
- 1.4 Carrier Transport in Semiconductors . . . 16
- 1.5 Generation of charged carriers . . . 17
- 1.6 Basic semiconductor Structures . . . 22
  - 1.6.1 p -n Junctions . . . 22
  - 1.6.2 Metal -Oxide -Semiconductor Capacitors (MOS) . . . 31

2 Silicon detectors in High Energy Physics 37
- 2.1 Introduction . . . 37
- 2.2 Silicon Tracking Detectors . . . 38
  - 2.2.1 Operation principle . . . 38
- 2.3 Componets of Silicon strip detectors . . . 40
- 2.4 Position resolution and localization . . . 43
- 2.5 Sensor Parameters . . . 44
  - 2.5.1 Global Parameters . . . 44
  - 2.5.2 Strip Parameters . . . 46
- 2.6 Hybrid Pixel devices . . . 49
- 2.7 Read-out electronics . . . 50
- 2.8 Radiation damage . . . 53

3 The LHC and CMS experiment 59
- 3.1 The Standard Model . . . 59
- 3.2 Physics motivation for upgrade . . . 61
- 3.3 The Large Hadron Collider (LHC) . . . 62

3.3.1 The LHC upgrade . . . 64
3.4 The Compact Muon Solenoid (CMS) . . . 65
3.4.1 The CMS Tracker . . . 67
3.4.2 Requirements for a new Tracker . . . 70
3.5 The CMS Tracker Upgrade . . . 73
3.5.1 Phase- I Upgrades . . . 73
3.5.2 Phase -II Upgrades . . . 75
3.5.3 Electrical specifications and quality assurance . . . 79

4 Electrical Characterization of silicon sensors and Test structures 81
4.1 Introduction . . . 81
4.1.1 The wafer and materials . . . 82
4.2 Experimental Setup . . . 83
4.3 Multi Geometry Silicon Strip Sensor MSSD . . . 84
4.3.1 Experimental Results . . . 85
4.4 Electrical characterization on 2S wafer prototype . . . 89
4.4.1 Diodes . . . 90
4.4.2 MOS . . . 95
4.4.3 Baby Sensors . . . 100
4.5 Electrical characterization on PS -p light sensors . . . 111
4.5.1 IV macropixel -scans . . . 113

5 Conclusion 121

Bibliography 122

Chapter 1

Basic semiconductor properties and devices

1.1 Introduction

Semiconductor devices and semiconductor technology have led to major technological advances. Since the mid -20th century semiconductor technology has developed very rapidly and now is the largest industry in the world producing a new technology almost every day. Semiconductor devices are used to computers, collar cells, telecommunications. The device feature size is shrinking continuously and the number of transistors on an integrated circuit (IC) chip is increasing rapidly, as predicted by Moore's law.

Semiconductors are used also as detectors in large variety of fields in science including nuclear physics, elementary particle physics, optical and x -ray astronomy, medicine and materials testing. The success of semiconductor detectors is due to several unique properties such as: the precise potion measurement, the readout speed, the simultaneous measurement of energy and position.

In this chapter a brief introduction to the semiconductor properties is made with emphasis in silicon and the basic devices that are used as building blocks for silicon detectors which are used in particle physics experiments.

1.2 Semiconductor Physics

Semiconductors are materials with electrical conductivity between good conductors such as metal (including copper, aluminum, tungsten, etc.) and good insulators such as rubber, plastic, and dry wood. The most commonly used semiconductor materials are silicon (Si) and germanium (Ge), both of which are located in column IVA of the periodic table of elements. One of the most important properties of a semiconductor is that its conductivity can be controlled by intentionally adding certain impurities, a process called doping, and by applying an electric field.

Si and Ge are group IV elements with 4 valence electrons and tend to form covalent bonds. Each atom is surrounded by four close neighbors in the lattice. Si atoms are arranged in a tetrahedron and each atom share its fourth valence electron with the neighboring atoms. A three dimensional and a two dimensional schematic is shown in 1.1.

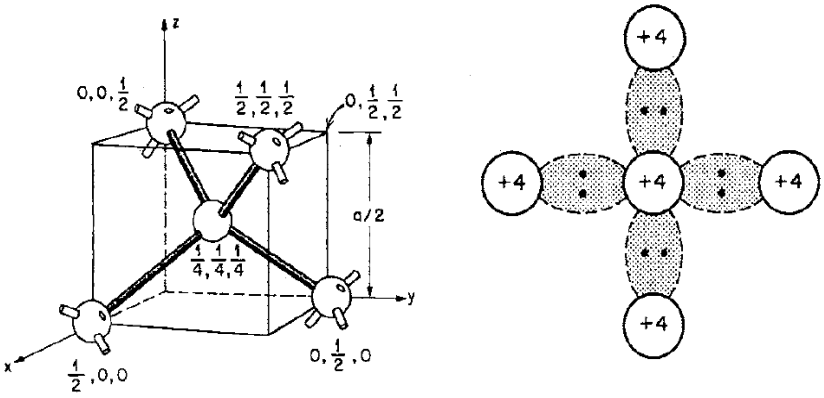

Figure 1.1: *Tetrahedron bond and schematic two-dimensional representation [1]*

1.2.1 Energy Bands

Isolated atoms have discrete energy levels. At large distances a Si atom have an electron configuration $(1s^2 2s^2 2p^6) 3s^2 3p^2$ where each state has one energy level $E_a(n,l)$. When the inter -atomic distance is getting smaller in order to form the crystal lattice of a solid, each atom is exposed to the sufficiently strong field of the neighboring atoms. In a crystal lattice containing N atoms, each energy level is repeated N times. In other words each energy state in the lattice has an N -fold degeneracy. But the interaction of each atom in the lattice with the neighboring atoms, removes the degeneracy. As a result each energy level is now split to N closely spaced sub -levels. For $N \rightarrow \infty$, the space between the sub -levels reduce even more. Consequently, they can be represented as energy bands. [2]

The separation between the sub -levels in a crystal of size $1\ cm^3$,($N \approx 10^{22}$ atoms), with a band width of about $1\ eV$ is about $10^{-22}\ eV$. The separation is so negligible that the bands may be regarded as being practically continuous.

Bands are generally localized over the entire crystal. That is to say that the orbitals of a crystal are no longer necessarily identified with individual atoms or individual covalent bonds but generally exist throughout the entire body of the solid. Even so, the band structure of crystal, at least in a broad sense, still corresponds to the formation of bonding and anti -bonding molecular orbitals just like the merging of two individual atoms in a molecule. A more analytical description can be found in [2]. The linear combination of all bonding and anti -bonding states leads to the formation of the Valence bad which correspond to the bonding states, the Conduction band which corresponds to the anti -bonding states and the forbidden gap with no available states. Figure 1.2 describes the formation of the energy bands when the density is increased (more atoms are introduced).

Considering the wave functions of the electrons,in the outer shells overlap so much as to produce an electron cloud of uniform density. Those electrons are called ”free electrons” but this is only a relative term because the electrons remain confined within the crystal. On the other hand the wave -functions of electrons in the inner shells do not overlap and are slightly perturbed by the neighboring atoms,the energy states remains practically the same as the individual atoms. Electrons in conducting bands can move relatively freely inside solid materials and can conduct

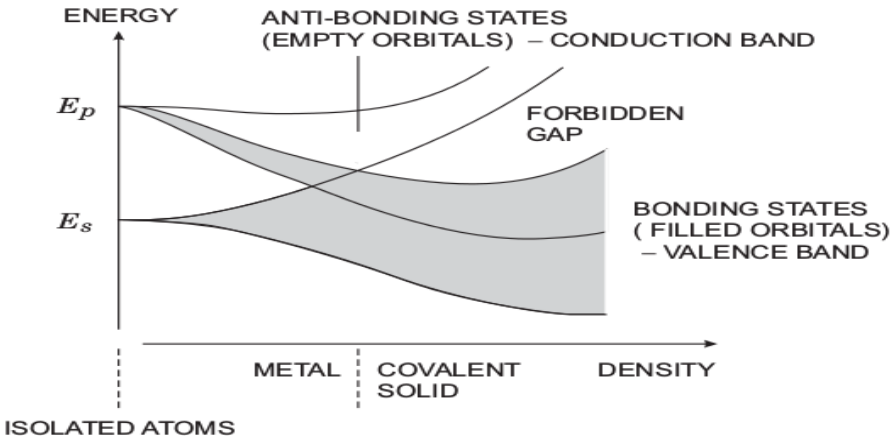

Figure 1.2: *As atoms are moved closer together the bonding and anti -bonding states spread to form the valence band, a forbidden gap, and a conduction band. [3]*

electric currents when an electric field is applied to the solid material. Electrons in the valence band are bound with the nuclei and cannot move freely, therefore, they cannot conduct electric currents. Since the valence band has lower electric potential, electrons always tend to stay in the valence band [2].

The valence band, the highest filled energy band with its upper energy border E_v and the conduction band, the lowest non filled energy band with its lower energy border E_c are separated by the band gap E_g. Where $E_g = E_c - E_v$.

In metals, the conducting band and valence band overlap and the conduction band is partially filled or the energy gap is very small, so small that electrons with thermal energy at room temperature $300K \approx 0.0259eV$) can be lifted from the valence band to the conduction band. Explaining why metals are always good electrical conductors. Figure 1.3.

In insulators, such as glass and plastic, the band -gap is so large that electrons cannot gain the required energy in order to jump from the valance band, to the conduction band so easily. Therefore a dielectric has very few electrons to conduct electric currents.

For semiconductors, the band -gap is somewhere between that of conductors and insulators. In a high purity silicon at 300 K and normal atmospheric pressure, the energy gap is $E_g = 1.12$ eV. At low temperatures $(T \approx 0K)$ the valence band is completely filled and the conduction band is empty therefore the semiconductor in this stage acts as an insulator. The electrons are strictly bound to their covalent bonds. At higher temperatures a small number of covalent bonds breaks and electrons and holes pairs are produced in the material.

Also if energy is imparted to a bond by incident radiation for example a photon or a transversing charge particle the bond can be broken. The electrons appear in the conduction band and can move freely throw the lattice. The holes appear in the valance band and it can also move with an indirect mechanism. The hole can be filled by an electron from the nearby atoms, thereby moving to another position. The motion of electron and hole can be directed by an electric field. Holes can move more slowly as the motion depends sequential transition probabilities. Figure 1.4. The minimum detectable energy is set by the band -gap A small band -gap increases the signal but

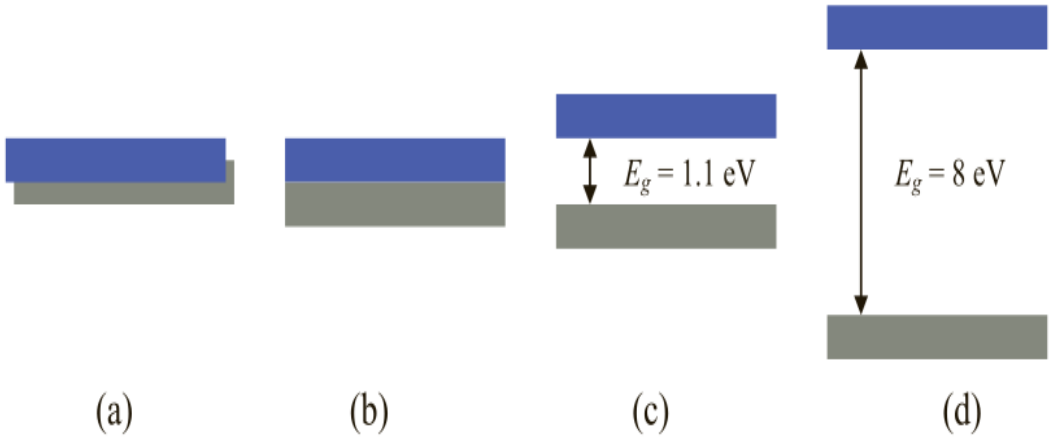

Figure 1.3: *Simplified band structures for metals, semiconductors and insulators. The energy gap in insulators are quite large. In semiconductors the conduction band is empty for $T = 0k$. the electrons in semiconductors acquire enough energy in order to move to the conduction band for $T > 0$ K. Conduction band and valence band overlap in metals with good conductivity such as Al or they form a very small band -gap like Na. [4]*

leads to an exponential increase of the background current. On the other hand a large band -gap greatly reduces the thermally excited signal, but also reduces the number of charge pairs that will be generated leading to a low signal. Also the conductivity of the sensor must be low in order to apply external voltage without having excessive current flow. The choice of the material in order to use as a semiconductor detector must compromise between those controversy requirements. As a result the rage of materials that can be used for detectors is quite limited. [3].

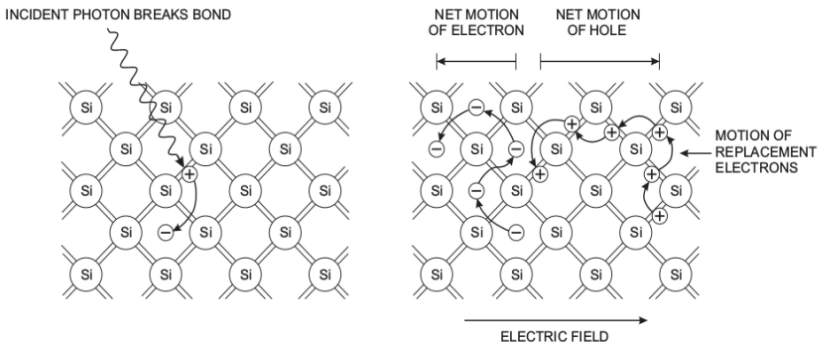

Figure 1.4: *The incident radiation on the material can give a valence electron enough energy in order the bond to be broken, creating a free electron and a vacancy (hole). The electric field can force the electrons to move. Also the vacant position can also move, by successively "borrowing" electrons from neighboring atoms. [3]*

1.2.2 Intrinsic Semiconductors

Intrinsic semiconductors contain no impurities, or very few compared to the thermally generated electrons and holes. Since electrons are fermions, are described by Fermi -Dirac statistics. In thermal equilibrium the probability for occupancy of one state E at a Temperature T is given by 1.1

$$f_e(E,T) = \frac{1}{1+e^{\left(\frac{E-E_E}{kT}\right)}} \tag{1.1}$$

where E_F is the Fermi level. The probability that a state is not occupied, or the probability of creating a hole state is then given by 1.2:

$$f_h(E,T) = 1 - f_e(E) = \frac{1}{1+e^{\left(\frac{E_F-E}{kT}\right)}} \tag{1.2}$$

The density of states near the conduction band, is given by 1.3

$$N_e(E) = \frac{(2m_e^*)^{3/2}}{2\pi^2\hbar^3}\sqrt{E-E_C} \tag{1.3}$$

where m_e^*, is the effective mass of the electron and E_C is the minimum energy in the conduction band. Similarly the density of states near the valence band is given by

$$N_h(E) = \frac{(2m_h^*)^{3/2}}{2\pi^2\hbar^3}\sqrt{E_V-E} \tag{1.4}$$

where m_h^*, is the effective mass of the electron and E_V is the maximum energy in the valence band

Then from 1.1 and 1.3 the total density of free electron carries is:

$$n = \int_{E_C}^{\infty} N_e(E) f_e(E,T) = \frac{2}{\hbar^3}(2\pi m_e^* k_{\mathrm{B}} T)^{3/2} e^{\left(-\frac{E_C-E_F}{k_B T}\right)} = N_C e^{\left(-\frac{E_C-E_F}{k_B T}\right)} \tag{1.5}$$

Respectively the density of free holes from the equations 1.2 and 1.4

$$p = \int_{E_o}^{E_V} N_h(E) f_h(E,T) = \frac{2}{\hbar^3}(2\pi m_h^* k_{\mathrm{B}} T)^{3/2} e^{\left(-\frac{E_F-E_V}{k_B T}\right)} = N_V e^{\left(-\frac{E_F-E_V}{k_B T}\right)} \tag{1.6}$$

where N_C and N_V are the effective density of states at the conduction and valence band respectively. The product of electrons and holes $np = N_C N_V e^{-\frac{E_C-E_V}{kT}}$, depends on the energy gap $E_g = E_C - E_V$ and is independent from the Fermi level E_F.

In an intrinsic semiconductor without any defects or dopants, the concentration of electrons and holes are equal in thermal equilibrium. $n = p = n_i$. The total density of charge carriers is given according to the mass action law 1.7:

$$n_i = pn = \sqrt{E_C E_V} e^{-\frac{E_C-E_V}{kT}} \tag{1.7}$$

Then the Fermi energy in the intrinsic case can be calculated by:

$$E_i = \frac{E_C + E_V}{2} + \frac{3k_B T}{4} ln\left(\frac{m_h^*}{m_e^*}\right) \tag{1.8}$$

Intrinsic silicon at room temperature (300 K), has about 1.5×10^{10} electrons per cubic centimeter in the conducting band. This means at room temperature, only about one in ten trillion electrons is in the conducting band, while the majority of electrons remain in the valence band. Therefore, intrinsic semiconductors can conduct electric currents at room temperature better than dielectrics, but not as well as conductors [4].

1.3 Extrinsic Semiconductor

Intrinsic semiconductors are rarely used in semiconductor devices. The properties of silicon can be changed by adding a small fraction of specific impurities. This procedure is called doping and can be performed in selected regions of the crystal. By incorporating elements from the neighboring groups of the periodic table into the silicon lattice, intermediate energy states will occur in the band gap and the Fermi energy level is shifted towards the edges of the valence or the conduction band. There are mainly two types of doping [5].

- *N-type:*

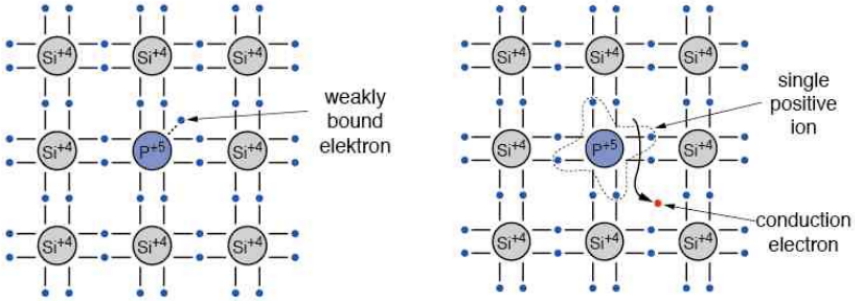

(α′) Doping process for N-type semiconductor

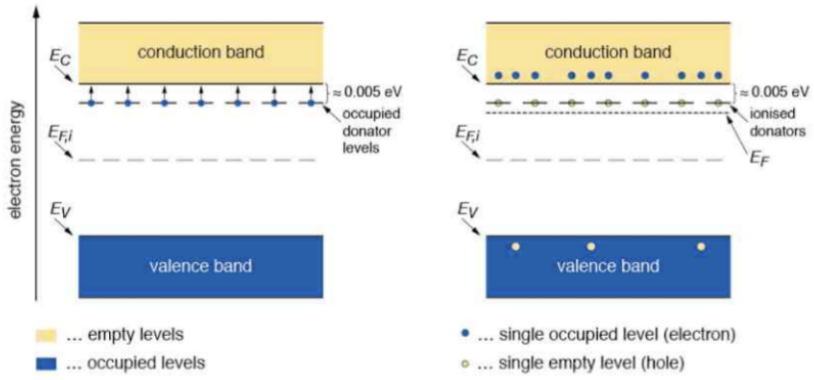

(β′) Energy Bands for N-type semiconductors [6]

This type of doping is made, by introducing a small concentration of a group V element of the periodic table, such as phosphorous. In this process a phosphorous atom is substituted with a silicon atom in the lattice. The phosphorous atom has 5 valence electrons, which 4 of them will form covalent bonds, with the 4 neighboring Si atoms in the lattice. The 4 electrons associated with the lattice bonding, are incorporated into the valence band just as they would be for a silicon atom. The fifth electron is localized in an intermediate

state near the conduction band and is weekly bound to its primary atom, actually 0.044 eV below the conduction band. These states is called *donor states* and the doping element of this type is called *donor*. Actually the doping element donates its excess electron to the conduction band of the semiconductor. In temperatures greater than just about 100 K the silicon lattice has sufficient vibrational energy due to random thermal motion to promote this excess electron to the conduction band where it becomes a mobile carrier. In the conduction band the excess electron is separated from the phosphorous atom and can be localized anywhere in the lattice (delocalized) and the phosphorus atom becomes a positively ionized impurity.

- *P-type:*

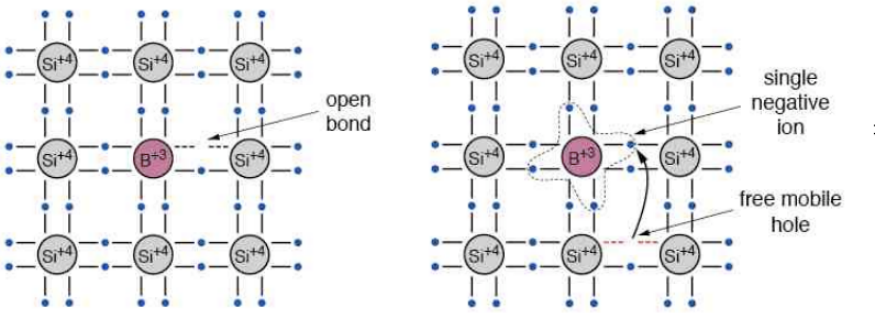

(α′) Doping process for P-type semiconductor

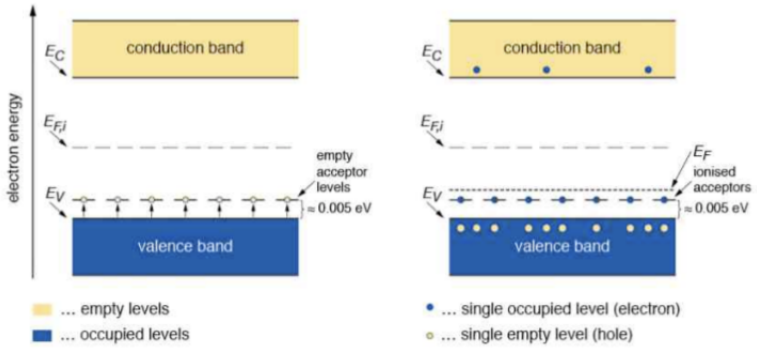

(β′) Energy Bands for P-type semiconductors [6]

Conversely, suppose that in a silicon substrate a small concentration of a group III is injected, for example Boron. The boron has 3 valence electrons. As a consequence, if a boron is substituted with a silicon atom then it will form covalent bonds with 3 neighboring Si atoms. One electron is missing in the covalent bonds and thus creating a hole. Considering the energy band model, the impurity atoms of group III in silicon will introduce energy levels close to the valence band maximum. This energy states is called *acceptor states*. The vibrational energy of the silicon lattice easily promotes electrons from the valence band into the acceptor states. Again the energy required to ionize the boron atom is small in comparison the band gap and is of the same magnitude as kT, so all the boron atoms in the lattice is ionized.

1.4 Carrier Transport in Semiconductors

Electrons and holes are essentially free particles. In order for a semiconductor crystal to have a significant conductance, it must have a large number of mobile carriers. Without an external applied voltage and with uniform concentration the carriers have a random thermal motion and their average displacement is zero. However if an external potential difference is applied, the generated electric field that it will be formed, will force the carriers to move in one specific direction, resulting in a net current flow and consequently mobile carries will acquire an average drift velocity.

There are mainly two mechanisms associated with carries motion, drift and diffusion [5].

Drift

Under the influence of an electric field carriers will be accelerated in a direction determined by the electric field. During their motion carriers scatter on imperfections within the lattice. The average velocity can be obtained by

$$v_e = -\mu_e E \quad \textit{and} \quad v_h = \mu_h E \tag{1.9}$$

where, $\mu_n = \frac{q\tau_c}{m_n}$ is the mobility of electrons and μ_p is the mobility for holes. For both carriers is given by

$$\mu_{e,h} = \frac{e\tau_s}{m^*_{e,h}} \tag{1.10}$$

where $m^*_{e,h}$ is the effective mass for electrons and holes and τ_s is the average time between scattering processes.

Diffusion

Diffusion is the second mechanism of carrier motion. It is caused by an inhomogeneous distribution of free charge carriers in a semiconductor crystal. For simplicity we are considering that there are no electrical effects on the carries. We thus threatening electrons and holes as if they were electrically neutral. Carrier will move from areas with higher concentration to areas with lower concentration. This effect will result to a smoothening of the charge distribution. The diffusion equation is given by:

$$F_e = -D_e \nabla n \quad \textit{and} F_h = -D_h \nabla p \tag{1.11}$$

where D_e and D_h is the diffusion parameter and is given by $D = \frac{kT}{q}\mu$.

Combining the two mechanisms the current densities are obtained.

$$J_n = q\mu_n nE + qD_n \nabla n \tag{1.12}$$

$$J_p = q\mu_p nE + qD_p \nabla p \tag{1.13}$$

1.5 Generation of charged carriers

Generation of free charged carriers can be made by excitation of electrons from the conduction band to the valence band. The number of holes and electrons that are created are equal in number. The energy that is needed in oder to have this transition can be given by various mechanisms such as optical excitation, thermal agitation or ionizing by charged particles.

These processes disturbs the semiconductor system from the equilibrium ($pn > n_i^2$) and the recombination mechanisms counteract them in order to return the system back to the thermal equilibrium condition where ($pn = n_i^2$). In recombination holes and electrons interact with each other and annihilate. The electrons fall in one or multiple steps into the empty state that is associated with the hole.

Also it is possible to form regions in semiconductor systems with ($pn > n_i^2$) or ($pn < n_i^2$) by injecting carriers of one type like the forward-biasing diode or by depleting the semiconductor volume like the reversed-biasing diode [5].

In the following sections the different mechanisms for the combination and the recombination processes are disused.

Generation mechanisms

Thermal generation

Thermal generated carriers can affect the functionality of the detector as they are source of noise and can affect the produced desired signal. In thermal excitation electrons from the valence band by acquiring a sufficient amount of thermal energy can overcame the Energy band gap and transit from the valence band to the conduction band.

In direct semiconductors like GaAs the excitation of an electron from the conduction band to the valence band can be done directly by one step , but GaAs has a very large band gap and the probability of direct excitation is very low. In direct semiconductors with a small band gap the direct excitation is more probable and the created free charged carriers will affect the signal.

In indirect semiconductors like Si and Ge the minimum energy needed for excitation depends not only to the width of the band-gap because the maximum of the conduction band and the minimum of the valence band are located at different momenta. Figure 1.7 Thus an additional momentum has to be transfered in the process for direct excitation. The excitation has then to be done using the intermediate states created by impurities. Such intermediate states in the band gap appear due to defects and imperfections in the lattice or by doping. In Si the probability of direct excitation is extremely low. But in some indirect semiconductors like Ge the energy gap is very small so that the probability of excitation of the electrons only by thermal energy by one step is very high. Therefore these detectors have to be operated at low temperatures.

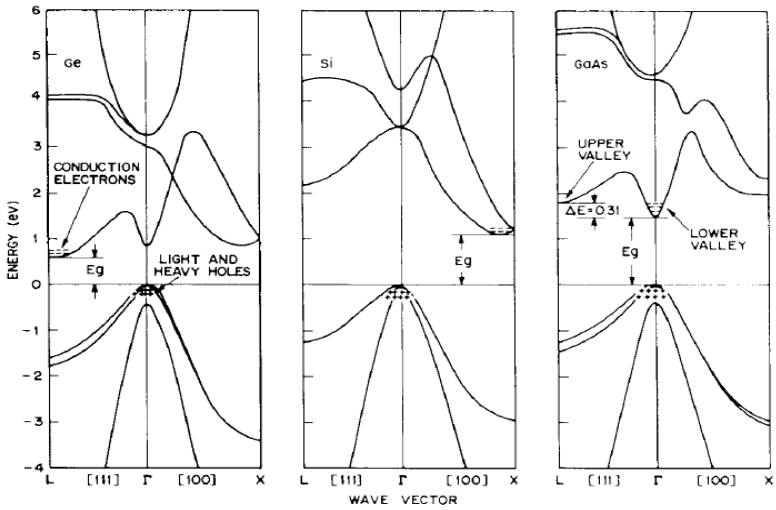

Figure 1.7: *Band structure vs wave-vector. In the Si and Ge the band -gap is associated with a non zero wave vector while in GaAs the transition occurs with zero momentum [3].*

Generation by Charged Particles

The working principle of all detectors is based in the generation of free charged carries that are produced from a charged particle that is passing throw the volume of the detector for example a gas or semiconductor. Charged particles that traversing throw the material lose part of their kinetic energy throw elastic collisions with the electrons of the medium. During this process the atoms of the medium get ionized. The average kinetic loss of charged particles that traversing throw matter was first examined by Bohr. A semi -quantum mechanical theory came later by Bethe -Both. The Bethe -Bloch formula with the corrections for density and shell effects is given by 1.14. A more analytical description can be found in [7]

$$-\frac{dE}{dx} = 2\pi N_A r_e^2 m_e c^2 \frac{Z}{A}\frac{1}{\beta^2}\left[ln\left(\frac{2m_e c^2\beta^2\gamma^2 \mathrm{T}_{max}}{I^2}\right) - \beta^2 - \delta(\gamma) - 2\frac{C}{Z}\right] \tag{1.14}$$

Where:

- N_A Avogadro's number
- m_e, r_e electron mass and the radius of the electron in classical theory
- Z, A the atomic number and the atomic mass
- $\beta = \frac{v}{c}$ and $\gamma = \frac{1}{\sqrt{1-(\frac{v}{c})^2}}$ the relative velocity and Lorentz factor
- $Tmax$ is the maximum kinetic energy that can be transfered from the traversing electron to the imparted in a single collision
- I the mean excitation energy of the imparted electron
- δ, C the density effect correction and the sell effect corrections

The maximum kinetic energy that can be transfered is given by a knock -on collision. For an incident particle of mass M the kinetic energy is given by

$$T_{max} = \frac{2m_e c^2 n^2}{1 + 2s\sqrt{1+n^2} + s^2} \tag{1.15}$$

where $s = \frac{m_e}{M}$ and $n = \beta\gamma$ Moreover if $M \gg m_e$, then

$$T_{max} = 2m_e c^2 n^2 \tag{1.16}$$

The quantities δ and C are corrections to the Bethe Bloch formula which are becoming more important at high and low energies respectively. The density effect (δ) arises from the fact that the electric field of the particle also tends to polarize the atoms among its path. The polarization of the atoms in the medium forms an electric field which shields the electrons far away from the path of the incident particle. The shell effect correction C is associated to the non-participation of electrons of inner shells (K, L, . . .) in the collision loss process, when (in an absorber with atomic number Z) the incoming velocity is no longer much larger than that of the bound atomic electrons.

At no -relativistic energies the energy loss $\frac{dE}{dx}$ is dependent by $\frac{1}{\beta^2}$ and decreases with increasing velocity until $\beta\gamma = 3$ is reached which is about $u = 0.96c$ where the energy loss reach a minimum. This is the minimum deposited energy of the medium and particles with this energy are called Minimum Ionizing Particles (MIPs). The minimum value of $\frac{dE}{dx}$ is the same for all particles with the same charge. The noise of a detector in High energy Physics experiments must be kept below the energy of minimum ionizing particles.

As the energy increases beyond that point the term $\frac{1}{\beta^2}$ becomes constant and $\frac{dE}{dx}$ rises again due to the logarithmic dependence of 1.14 with the Lorentz factor γ. This relativistic uprising of the $\frac{dE}{dx}$ for higher energies is corrected by the density factor. For lower energies than the minimum, every particle exhibits a distinct $\frac{dE}{dx}$ curve and the $\frac{dE}{dx}$ characteristics at lower energies can be used for particle identification.

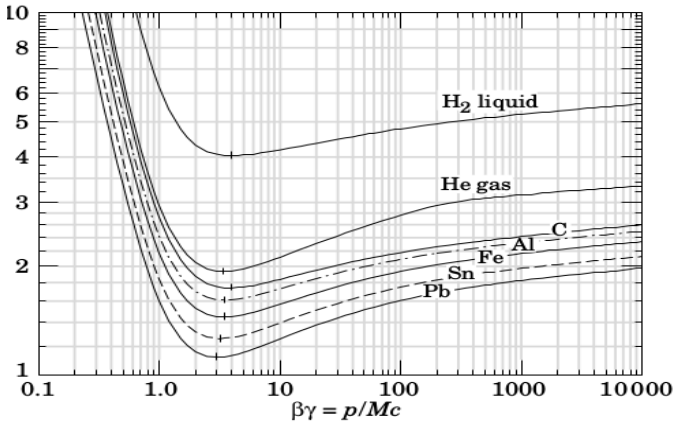

Figure 1.8: *Energy loss rate in liquid hydrogen, gaseous helium, carbon, aluminum, iron, tin, and lead.*

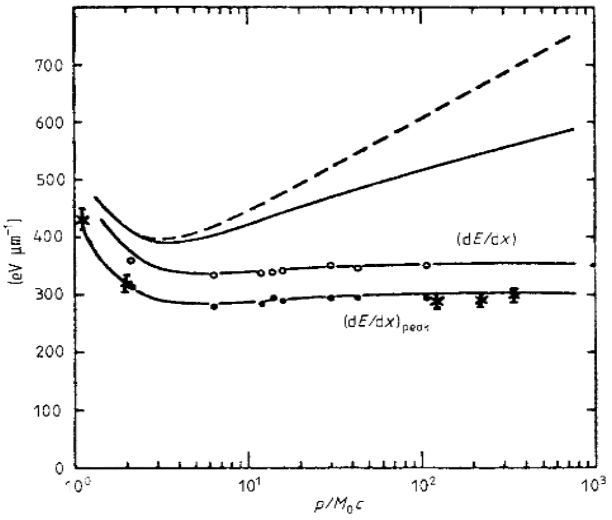

Figure 1.9: *Energy loss in silicon (in $eVpm^{-1}$) as a function of the parameter ($p/M_o \cdot c$). The curves are (from the top) the average stopping power without (broken curve) and with (full curve) the density effect. The following two other curves show the average stopping power with both the restriction (Sternheimer 1971) and the density effect taken into account and the prediction of the most probable energy loss compared with the experimental points. For more details see [8].*

Each interaction of an incoming particle with atomic electrons can transfer a different amount of kinetic energy. Equation 1.14 allows one to compute the average energy -loss, but this value undergoes statistical fluctuations. The number of collisions in a finite medium responsible for energy loses are a series of independent successive events. The number of collisions can be described with a Poisson distribution while the energy that is lost by a particle, along a given traversed path x, will be characterized by an energy distribution function called the energy-loss distribution function or energy straggling function first deduced by Landau.

The energy transfered from the incoming particle to the atomic electrons can produce recoil particles which has sufficient energy in order to produce secondary ionization very similar to the primary one. The electrons that are produced by secondary electrons are called δ -rays or δ -electrons or simply secondary electrons. Those δ -rays are very energetic and can travel large distances throw the medium and even escape from it and are responsible for the asymmetric long tale that is shown in the Landau distribution. Typical solid state detectors are not thick enough to fully absorb secondary δ -rays. The energy loss by the incoming particle differs from the deposited energy inside the detecting medium and it is needed to define an effective detectable maximum transferred energy . often a restricted energy loss is used to estimate the deposited energy in a detector using instead of T_{max} the effective detectable max transferred energy (= effective average max δ -rays energy that can be absorbed inside the device).

Figure 1.10 show the energy loss distribution in silicon detectors with different thicknesses. For detectors with moderate thickness,the energy loss probability distribution for the energy that is lost by a particle in a single hit is described by the Landau curve, whose tail at high energies is due to the so called delta rays, which are very energetic but rare events. As the detector thickness increases, the Landau curve gains a more Gaussian shape, since the material thickness allows

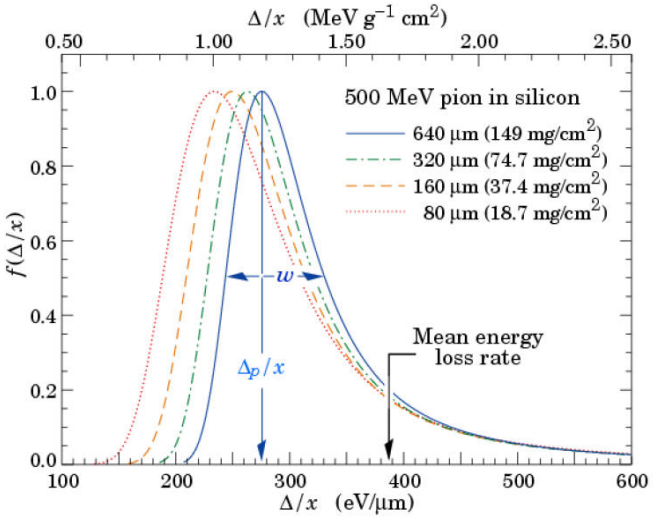

Figure 1.10: *Straggling functions in silicon for 500 MeV pions, normalized to unity at the most probable value Δ/x. The width w is the full width at half maximum [9].*

many hits with atomic electrons.

Generation of Charge Carriers by Electromagnetic Radiation

An other way of forming excess free carriers is by Electromagnetic radiation. A photon is absorbed giving its energy to an electron in the valence band.if the energy is just above the energy gap $E = E_g$. The electron is then excited from the valence to the conduction band leaving behind a hole in the valence band. If the photon has an energy above the energy gap $E = E_g$ an electron for lower states in the valence band will be excited to higher states in the conduction band (far from the energy gap). In this case the electron and hole will subtract each other coming closer and closer to the energy gap by emitting their excess energy in the form of phonons (lattice vibrations) and lower energetic photons.

Also an excitation by photon with an energy below the energy gap $E < E_g$ is possible if there are energy states in the energy band gap due to lattice imperfections, defects or doping

1.6 Basic semiconductor Structures

1.6.1 p -n Junctions

The p -n junction is of great importance for modern electronic application it is the basis for all semiconductor electronics as well as for detectors. In a silicon substrate a big number of free charged carriers is produced at intermediate temperatures ($10^9\ cm^{-3}$). This big number of thermal generated particles cause the produced signal from a ionizing particle to be lost. In order to use silicon as a detector the number of those thermal charged carriers must be reduced by cooling the device to very low temperature, so the production rate of free charged carries minimizes, or by depleting the volume of the detector. In large experiments reaching very low temperatures would be difficult. So the most convenient way is to use an abrupt reversed-bias p-n junction. For more details see [1],[2],[5], [10]

A p -n junction is a two terminal device and it consists of two extrinsic semiconductors with opposite doping. Such structure can conduct current mainly in one direction.

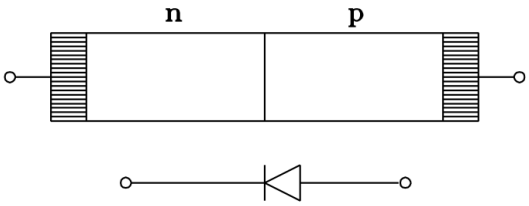

Figure 1.11: *A p-n diode structure schematic [5].*

p-n in Thermal Equilibrium

At first, let assume that the two homogeneously doped regions p and n are separated. The two volumes are electrically neutral and the electrons and holes are homogeneously distributed at each other, the concentration is constant(no gradient). Bringing the two regions together, the majority carriers in each area, electrons and holes respectively, will diffuse to the regions of lesser concentration due to the concentration gradient that is formed following Frick's first law [1]:

$$j_{Diff} = -eD\nabla n$$

where n is the concentration, D is the diffusion constant and e the electron charge unit.

In thermal equilibrium detailed balance must exist. This means that there is no external influences such as applied field, electrical currents, optical excitations or any energy transfer.

Electrons move to the p region and holes move the n region and recombine. This process forms an area around the boundary with surplus of ionized charged dopant atoms. The surplus of ionized donors and acceptors create a potential distribution V_{bi}. The height of the potential depends to the temperature and the doping levels. Also an Electric Field $\mathcal{E}$ that counteracts the diffusion, is formed. The electric field sweeps away any thermal generated charged carrier pair that is formed in this area. This area is a space -charge region and is free of movable charged particles.

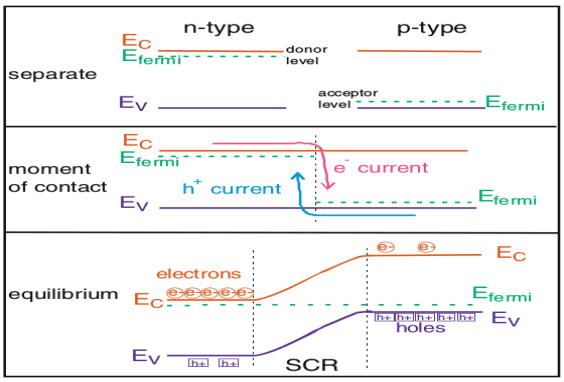

Figure 1.12: When $p-$ and $n-$ type semiconductors are brought together electrons move to the lower Fermi level and holes to the higher, building up a space charge region. In equilibrium the Fermi level is constant. *[11].*

The above process creates an dynamic thermal equilibrium with detailed balance for both holes crossing the junction and for electrons. This means that the hole currents to left and right must be equal to each other. Diffusion flow and field current are compensating each other at the pn -junction. From the current equation of drift and diffusion there is :

$$J_n = q\mu_n \left(n\mathcal{E} + \frac{kT}{q}\frac{dn}{dx} \right) = \mu_n n \frac{dE_F}{dx} = 0 \tag{1.17}$$

$$J_p = q\mu_p \left(p\mathcal{E} + \frac{kT}{q}\frac{dn}{dx} \right) = \mu_p p \frac{dE_F}{dx} = 0 \tag{1.18}$$

Therefore.

$$\frac{dE_F}{dx} = 0 \tag{1.19}$$

The Fermi energy level must be constant through the device. Considering the energy band model the requirement that the energy Fermi is constant means that the energy bands must bend near the junction. The band bending depends on the potential distribution that is created between the two parts. The potential distribution is called built -in potential, or diffusion potential and can be calculated as:

$$V_{bi} = \frac{1}{q}\left(E_i^p - E_i^n\right) \tag{1.20}$$

where E_i^p and E_i^n are the intrinsic energy levels on the p and n side (not in the depleted area, in the area of each side that the bands remain constant). Supposing that the majority carriers are equal to acceptors and donors concentrations respectively (complete ionization) we have:

$$n = N_D = n_i e^{\frac{E_F - E_i^n}{kT}} \quad \text{and} \quad p = N_A = n_i e^{\frac{E_i^p - E_F}{kT}} \tag{1.21}$$

Therefore the above equation 1.20 from 1.21 becomes:

$$V_{bi} = \frac{kT}{q} ln \left(\frac{N_A N_D}{n_i^2} \right) \tag{1.22}$$

The space charge density has a width w that is equal with $w = x_n + x_p$ the sum of the absolute values of the depleted region width in both sides. In order to calculate this width first lets consider the Poisson equation that is described by

$$\frac{\partial^2 V}{\partial x^2} = -\frac{1}{\varepsilon_{sc}\varepsilon_0}\rho(x) \tag{1.23}$$

where ε_{sc} is the electrical permittivity for the silicon ε_0 is the electrical permittivity of vacuum and $\rho(x)$ the charge density described by

$$\rho(x) = -q[n(x) - p(x) + N_A - N_D] \tag{1.24}$$

By integrating the Poisson equation, the electrical field strength emerges. For simplicity it is assumed that there is an abrupt change between the depleted region and the neutral regions (The regions of the device that hasn't depleted). Meaning that the Electric field at the boundaries of the depleted area will be zero. [1]. Also the device in total is electrical neutral, so the total charge per unit area on the p side must be equal to the total charge per unit area in the n side resulting to:

$$N_A x_p = N_D x_n \tag{1.25}$$

The depletion region is free of mobile charges, so $n(x) \approx p(x) \approx 0$

$$\mathcal{E}(x) = -\frac{qN_A(x + x_p)}{\varepsilon_{sc}\varepsilon_0} \quad -x_p \leq x \leq 0 \tag{1.26}$$

$$\mathcal{E}(x) - \mathcal{E}_{max} = -\frac{qN_D(x)}{\varepsilon_{sc}\varepsilon_0} \tag{1.27}$$

$$\mathcal{E}(x) = -\frac{qN_D(x_n - x)}{\varepsilon_{sc}\varepsilon_0} \quad 0 \leq x \leq x_n \tag{1.28}$$

where from 1.25 the $\mathcal{E}_{max}$ at $x = 0$ is given by

$$\mid \mathcal{E}_{max} \mid = \frac{qN_A x_p}{\varepsilon_{sc}\varepsilon_0} = \frac{qN_D x_n}{\varepsilon_{sc}\varepsilon_0} \tag{1.29}$$

Integrating the electric field leads to the potential $\varphi_(\chi)$ which will have a parabolic behavior with boundary condition $\varphi_(x) = 0$. The potential will be constant outside the depleted area. From equations 1.28 it derives that the potential is given by the equations below 1.30 , 1.31.

$$\int_{-x}^{0} \mathcal{E}(x) = -\frac{qN_D}{2\varepsilon_{sc}\varepsilon_0} \int_{-x}^{0} (x + x_p) \cdot dx \Rightarrow$$

$$\varphi_0 - \varphi_p(-x) = -\frac{qN_A}{2\varepsilon_{sc}\varepsilon_0} \left(2xx_p - x^2\right) \Rightarrow$$

$$\varphi_p(x) = -\frac{1}{2}|E_{max}|x_p \left[\left(\frac{x}{x_p}\right)^2 + 2\frac{x}{x_p}\right] \qquad for \quad -x_p \leqslant x \leqslant 0 \tag{1.30}$$

$$\int_{0}^{x} E(x) = -\frac{qN_D}{2\varepsilon_{sc}\varepsilon_0} \int_{0}^{x} (x_n - x) \cdot dx \Rightarrow$$

$$\varphi_n(x) = \varphi(0) + \frac{qN_A}{2\varepsilon_{sc}\varepsilon_0} \left(x^2 - 2xx_n\right) \Rightarrow$$

$$\varphi_n(x) = \frac{1}{2}|E_{max}|x_n \left[\left(\frac{x}{x_n}\right)^2 - 2\frac{x}{x_n}\right] \qquad for \quad 0 \leqslant x \leqslant x_n \tag{1.31}$$

From the above equations and equation 1.29 it derives that the potential in each region is given by

$$V_p = \varphi_p(-x_p) = \frac{|\mathcal{E}_{max}| \cdot x_p}{2} = \frac{1}{\varepsilon_{si}\varepsilon_0}\frac{qN_A x_p^2}{2} = \frac{1}{\varepsilon_{si}\varepsilon_0}\frac{qN_D x_p x_n}{2} \tag{1.32}$$

and

$$V_n = \varphi_n(x_n) = \frac{|\mathcal{E}_{max}| \cdot x_n}{2} = \frac{1}{\varepsilon_{si}\varepsilon_0}\frac{qN_D x_n^2}{2} = \frac{1}{\varepsilon_{si}\varepsilon_0}\frac{qN_A x_n x_p}{2} \tag{1.33}$$

Then the total potential difference in the whole depleted region is given by 1.35:

$$V_{bi} = \varphi_n(x_n) - \varphi_p(-x_p) = \frac{1}{2}|E_{max}|(x_p + x_n) \tag{1.34}$$

$$V_{bi} = \frac{1}{2}|E_{max}|w \tag{1.35}$$

The above equation can also be written as 1.37 by using equations 1.29 and 1.25.

$$V_{bi} = \frac{1}{2}\frac{qN_D x_n}{\varepsilon_{si}\varepsilon_0} \cdot x_p + \frac{1}{2}\frac{qN_A x_p}{\varepsilon_{si}\varepsilon_0} \cdot x_n$$

$$V_{bi} = \frac{1}{2}\frac{q}{\varepsilon_{si}\varepsilon_0}(N_D + N_A)x_p x_n$$

$$V_{bi} = \frac{1}{2}\frac{q}{\varepsilon_{si}\varepsilon_0}\frac{(N_D + N_A)N_A x_p^2}{N_D} \tag{1.36}$$

$$= \frac{1}{2}\frac{q}{\varepsilon_{si}\varepsilon_0}\frac{(N_D + N_A)N_D x_n^2}{N_A} \tag{1.37}$$

The depletion width in each region and the total depletion width is then given by 1.40:

$$x_n = \sqrt{\frac{2\varepsilon_{si}\varepsilon_0}{q}\frac{N_D}{N_A(N_A + N_D)}V_{bi}} \tag{1.38}$$

$$x_p = \sqrt{\frac{2\varepsilon_{si}\varepsilon_0}{q}\frac{N_A}{N_D(N_A + N_D)}V_{bi}} \tag{1.39}$$

$$w = \sqrt{\frac{2\varepsilon_{si}\varepsilon_0(N_A + N_D)}{qN_D N_A}V_{bi}} \tag{1.40}$$

In the case where one region is more heavily doped than the other for example $N_A \gg N_D$. The equation for the depletion region width is simplified then to 1.41:

$$w = \sqrt{\frac{2\varepsilon_{si}\varepsilon_0}{qN_D}V_{bi}} \tag{1.41}$$

In the above analysis the assumption that the charge distribution has a box profile was made. This means that the distribution change abruptly between the space charge region and the neutral regions.

Applying an external Voltage

By applying an external voltage the equilibrium condition will be disturbed and the above analysis can only be applied in an approximate way. The potential variation across the junction is given by $V_{bi} - V$ and is decreased or increased depending on the polarity. Consequently the depletion width decreases or increases depending on the external applied voltage. The above equation 1.41 is then described by

$$w = \sqrt{\frac{2\varepsilon_{si}\varepsilon_0}{qN_D}(V_{bi} - V)} \tag{1.42}$$

Forward bias

When the external applied Voltage has the same polarity with the doping profile $V > 0$ the Voltage across the junction will decrease from the equilibrium value V_{bi} to $V_{bi} - V$, called forward bias. For example applying a negative Voltage to the n side and a positive Voltage to the p side of the junction, causes a large increase in the flow of electrons from the n side to the p side and a large flow of holes from the p side to the n side respectively . This process is called minority carrier injection , because the minority concentration at each neutral region will increase . Also the depletion width will decrease.

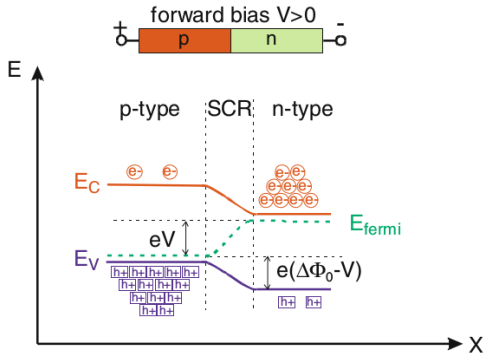

(α′) *Forward bias voltage: In the forward case, the barrier decreases.*

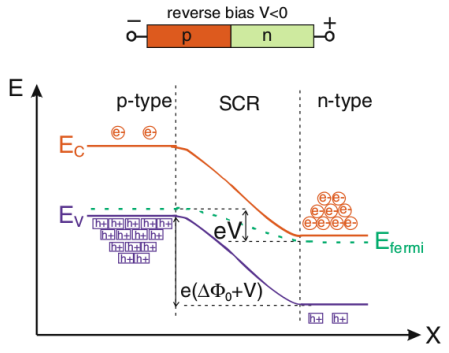

(β′) *Reverse bias voltage: In the reverse bias case, the potential barrier and the depletion width increases.*

Figure 1.13: Forward and Reverse bias in pn diodes [11].

Reversed bias

In detector technology the reversed bias operation of the junction is most important. In this case an external voltage is applied with different polarity $V < 0$ than the doping profile, so the voltage variation across the junction will increase from V_{bi} to $V_{bi} + V$. Accordingly the depletion width will increase forming an ionization chamber. Free carriers that are generated in the depleted region will be swept by the electric field while charge collected on the non-depleted regions recombine with the majority carriers. In order the junction to be used as a detector the depletion region must extend to almost all the volume in order the detector to be fully depleted $V_{bias} \gg V_{bi}$.

In the fully depleted case the equation 1.42 for the depletion width is simplified to

$$w = \sqrt{\frac{2\varepsilon_{si}\varepsilon_0}{qN_D} V_{bias}} \tag{1.43}$$

And the voltage at the full depletion is then given by

$$V_{fd} = \frac{D^2}{2\varepsilon_{si}\varepsilon_0 \rho\mu} \tag{1.44}$$

Where in full depletion the depletion width extends throw the whole volume of the detector $w = D$ and $\rho = \frac{1}{e\mu N_d}$ is the resistivity.

Current -Voltage characteristics

At the thermal equilibrium case the concentrations of holes and electrons deriving from Boltzmann statistics is given by 1.45

$$n = n_i e^{\frac{E_F - E_i}{kT}} \quad and \quad p = p_i e^{\frac{E_i - E_F}{kT}} \tag{1.45}$$

And the product of the two concentrations in the thermal equilibrium is equal to n_i^2. When the voltage is applied the minority carriers densities on both sides of the junction is changed. The concentrations are now expressed as 1.46.

$$n = n_i e^{\frac{E_{Fn} - E_i}{kT}} \quad and \quad p = p_i e^{\frac{E_i - E_{Fp}}{kT}} \tag{1.46}$$

where E_{Fn},E_{Fp} are the quasi-Fermi level for electrons and holes respectively. And the product of the two concentrations is now given by 1.47

$$pn = n_i^2 e^{\frac{E_{Fn} - E_{Fp}}{kT}} \tag{1.47}$$

Quasi -Fermi energies are used when the electrons and holes are not in thermal equilibrium with each other. But even though the electrons and holes are not in thermal equilibrium with each other, they still are in thermal equilibrium with themselves and can still be described by a Fermi energy which is now different for the electrons and the holes.

For a forward bias $E_{Fn} - E_{Fp} > 0$ and also $pn > n_i^2$ and for the reversed bias $E_{Fn} - E_{Fp} < 0$ and $pn < n_i^2$

As discussed previously two basic mechanisms compensate each other the drift current and the diffusion current. The net current for the non -equilibrium condition is expressed in relation with the quasi Fermi levels as 1.48

$$J_n = \mu_n n \nabla E_{Fn} \quad and \quad J_p = \mu_p p \nabla E_{Fp} \tag{1.48}$$

Of course in the equilibrium case where $E_{Fn} = E_{Fp} = E_F$ and $J_n = J_n = 0$. From the equations 1.46 it derives that the current for the minority carries at each side of the junction is given by 1.49

$$J_p = -qD_p \frac{dp_n}{dx}|_{x_n} \quad and \quad J_n = -qD_n \frac{dn_p}{dx}|_{-x_p} \tag{1.49}$$

By calculating the gradients from the continuity equations the Shockley equation is derived which is the ideal diode law 1.50.

$$J = J_n + J_p = J_0 \left[exp\left(\frac{qV}{kT} - 1\right)\right] \tag{1.50}$$

Where J_0 is the saturation current and is given by 1.51.

$$J_0 = \frac{qD_p p_{n0}}{L_p} + \frac{qD_n n_{n0}}{L_n} = \frac{qD_p n_i^2}{L_p N_D} + \frac{qD_n n_i^2}{L_p N_A} \tag{1.51}$$

The Shockley equation predicts the Current -Voltage characteristics of a germanium p -n junctions at low current densities, but for Si and GaAS can only give qualitative results.

Deriving from the ideal case a lot of deferent parameters has to be taken into account such as (i) the generation and recombinaton of carriers, (ii) the high injection conditions that may occur and (iii) the parasitic drop due series resistance (iv) the tunneling of carriers between states in the band -gap [1]

In reversed bias conditions with $(pn \ll n_i^2)$ which is the condition that the silicon detectors operate the thermal generation dominates. The rate of generation of electron hole pairs is given by the Shockley -Read -Hall process [12] , [13] , [1]. The current due to generation in the depletion region is given by 1.52:

$$J_{ge} = \int_0^{W_D} q|U|dx \approx \frac{qn_i W_D}{\tau_g} \tag{1.52}$$

Supposing a surface A of the junction, the total generation current also called leakage current is then described by 1.53

$$I_L = \int_0^{W_D} q|U|dx \approx \frac{qn_i W_D}{\tau_g} A \tag{1.53}$$

The leakage current is strongly dependent to the effective lifetime τ_g which is the generation lifetime of minority carriers which in turn depends in the concentration of impurity states N_t near the mid-gap. The current increases linearly with $W_D \propto \sqrt{V_{bias} + V_{bi}}$ until the detector is fully depleted. At higher bias Voltage an electrical breakdown is observed, where the current starts to increase dramatically. This abrupt increase occur due charge multiplication in charge collisions (avalanche breakdown) or due to tunneling effect (Zener breakdown) 1.14.

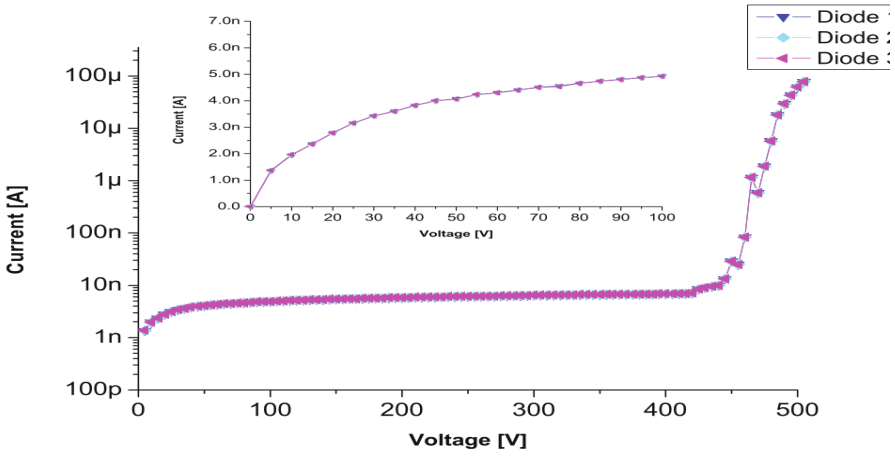

Figure 1.14: *Current -Voltage characteristics of Si diodes [11].*

Leakage current is a few $nA\ cm^{-2}$, for good quality detectors. This current is increasing up to several tens of μA and even more for irradiated detectors depending on the irradiation flux. The leakage current depends strongly on the temperature and follows the expression 1.54 [10] , [14].

$$I_L = T^2 exp(\left(-\frac{E_g}{2k_B T}\right) \tag{1.54}$$

If $T = 20^oC \approx 293K$ is taken as the normalization temperature of reference and T_m is the temperature at which the leakage current measurement has been performed, the necessary temperature correction to the leakage current is done using the equation 1.55.

$$I_L(293) = I(T_m)\left(\frac{293}{T_m}\right)^2 exp\left(-\frac{E_g}{\left[2k_B\left(\frac{1}{293}-\frac{1}{T_m}\right)\right]}\right) \tag{1.55}$$

Capacitance -Voltage characteristics

The capacitance of the sensor can be calculated by regarding the two planes of the space charge region that is formed as plates of a capacitor with a dielectric inside. The capacitance then will decrease linearly with w and consequently with $\sqrt{V}$. In order to find Capacitance - Voltage characteristics of a p -n diode it is necessary to consider the change of the voltage and surface charge when the width of the space charge region is increased from x to $w = x + dx$. For simplicity we can consider a heavily doped diode p^+n (which in fact is a common situation in detectors). In this case we can assume without deriving two much from the reality that the space charge region width will be fully contained to the low-doped substrate. A change dx in the space charge region width will cause a qN_Ddx change in charge, a $\frac{qN_Ddx}{\varepsilon\varepsilon_0}$ change in electric field and a $\frac{qN_Ddx}{\varepsilon\varepsilon_0}\cdot x$ change in the potential variation of the surfaces. Of course w can take a maximum value in the full depletion case and it will extend almost to the whole width of the diode [5] , [1].

Integrating the total field over the depleted region the total potential change is derived.

$$\psi_n = -\int_0^{W_D}\mathcal{E}(x)dx = [-x\mathcal{E}(x)dx]_0^{W_D} + \int_{\mathcal{E}(0)}^{\mathcal{E}_{W_\mathcal{D}}} xd\mathcal{E} \tag{1.56}$$

The first term is zero since in the surfaces the electrical field is zero. The total potential is then

$$\psi_n = \int_{\mathcal{E}(0)}^{\mathcal{E}_{W_\mathcal{D}}} x\frac{d\mathcal{E}}{dx}dx = \int_{\mathcal{E}(0)}^{\mathcal{E}_{W_\mathcal{D}}} x\frac{q}{\varepsilon_{si}\varepsilon_0}N_D(x)dx = \frac{q}{\varepsilon_{Si}\varepsilon_0}N_D(W_D)\frac{W_D^2}{2} \tag{1.57}$$

The applied external voltage will be the sum of the built -in potential V_{bi} and the ψ_n , $V = V_{bi} - \psi_n$.

Also the total charge in the depletion region is

$$Q_D = q\int_0^{W_D} qN_D(x)dx = qN_D(W_D)W_D \tag{1.58}$$

The capacitance per unit area for the junction is then given by

$$C_D = |\frac{dQ_D}{dV}| = |\frac{dQ}{dW}\frac{dW}{dV}| = \frac{\varepsilon_{Si}\varepsilon_0}{W_D} \tag{1.59}$$

For the measurement of the doping concentration, we must look at the variation of the inverse square of capacitance with the applied voltage.

$$\frac{d(\frac{1}{C_D^2})}{dV} = \frac{d(\frac{1}{C_D^2})}{dW_D}\frac{dW_D}{dV} = -\frac{2}{q\varepsilon_{Si}\varepsilon_0 N_D(W_D)} \tag{1.60}$$

The C -V measurements can be used to measure the doping profile of p -n diodes, by calculating the slope of a $1/C_D^2 - V$ plot. The slope of the plot will be analogous to $\propto \frac{1}{N_D}$.

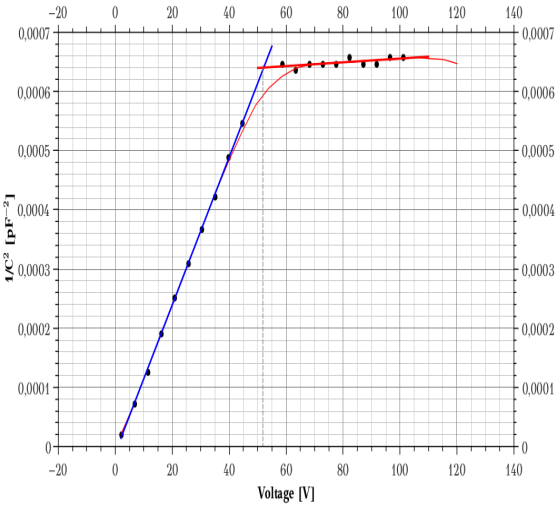

(α′) $1/C^2$ *versus voltage for diodes. From the slope of the curve the substrate concentration can be calculated.*

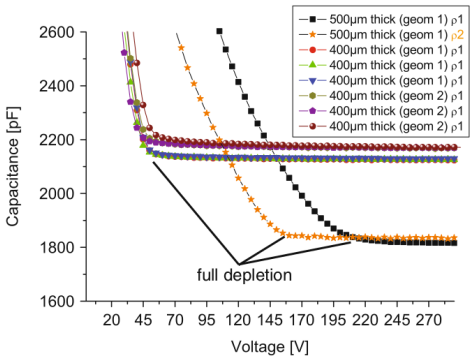

(β′) *Measurement plots that shows the capacitance versus voltage for diodes with different thicknesses areas and resistivity . The capacitance drops with the voltage until depletion is reached where it remains stable. The two upper curves have the same thickness with slightly different areas and the same resistivity. The two lower curves have higher thickness at* $d = 500$ *μm and different resistivities [11].*

1.6.2 Metal -Oxide -Semiconductor Capacitors (MOS)

The understating of the mechanisms between the interfaces of the metal -insulator -semiconductor structures is very important for the study of semiconductor detector systems and in semiconductor devices in general. The stability of all the semiconductor devices is largely related to the conditions that derive to the surfaces of those interfaces. The MIS (metal -insulator -semiconductor) structure has proved to be an extremely useful structure for the investigation of semiconductor surface effects.

The MIS structure is more frequently refereed to as MOS (Metal Oxide Semiconductor) since the most common insulator in the case of silicon is SiO_2. The MOS structure is commonly used to the charged coupled devices (CCD) for optical imaging and also it is an essential part of MOS-transistor.

Ideal MOS Capacitor

The metal oxide structure is shown in 1.16. The structure consists of a semiconductor volume with the one surface covered with an insulator layer SiO_2 and a metal surface on top of the oxide to be connected with the readout electronics, called AC coupled. In real modern silicon structures the ”metal” plate is a heavily doped p^+ or n^+ ploy -silicon layer, respectively, which behaves as a metal. The ploy -silicon is called the Gate (G) while the semiconductor is called Body (B). Typically a voltage is applied to the gate while the body is grounded.

The energy band diagrams of an ideal MOS structure is shown in 1.17 without bias for both n -type and p -type.

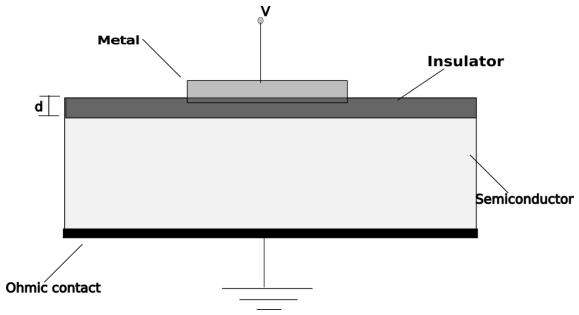

Figure 1.16: *Schematic of a MOS capacitor*

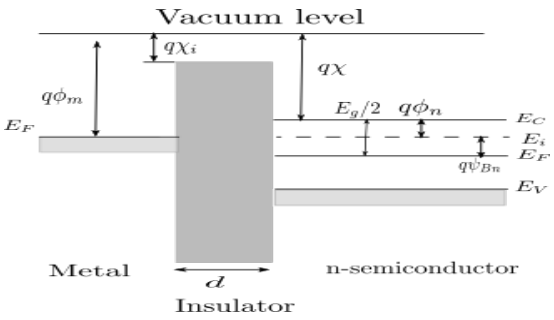

(α′) *Energy diagram for an MOS n -type without external applied Voltage*

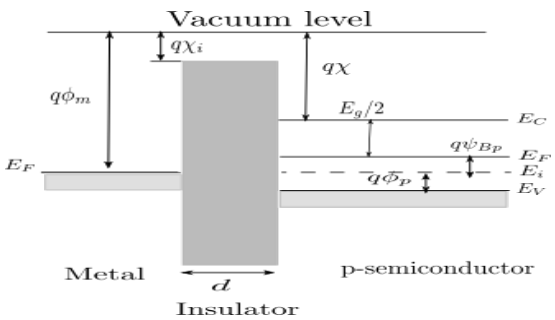

(β′) *Energy diagram for an MOS p -type without external applied Voltage*

Figure 1.17

In the ideal case it is considered that the difference between the work function of the semiconductor and the work function of the metal is zero. $\varphi_{ms} = \varphi_m - \varphi_s = 0$.

The energy band diagrams and the above conditions conclude in the fallowing relations 1.62. As referred to [1]

$$\varphi_{ms} = \varphi_m - \left(\chi + \frac{E_g}{2q} - \psi_{\mathrm{B}n}\right) = \varphi_m - (x + \varphi_n) = 0 \qquad \textit{n-type} \tag{1.61}$$

$$\varphi_{ms} = \varphi_m - \left(\chi + \frac{E_g}{2q} + \psi_{\mathrm{B}p}\right) = \varphi_m - (x + \frac{Eg}{2} - \varphi_p) = 0 \qquad \textit{p-type} \tag{1.62}$$

Where φ_m is the metal work function, χ is the electron affinity of the insulator, E_g is the energy gap of the semiconductor and $\psi_{\mathrm{B}n}$,$\psi_{\mathrm{B}p}$,φ_n,φ_p are the Fermi potentials with respect to the mid -gap and band edges.

In the ideal case, the energy bands remain flat, when there is no applied voltage flat band condition. The majority carriers are homogeneously distributed to the whole bulk of the semiconductor and the Electric field through the semiconductor is zero. As metal and semiconductor are separated from an insulator layer, charge carriers will have infinitely small probability for crossing between the semiconductor and the metal and therefore the current is zero, so the Fermi level remains flat in the semiconductor.

If an external voltage with different polarity , with respect to the semiconductor bulk is applied to the metal, then the majority carries will be attracted to the semiconductor surface adjacent to the oxide. Considering the p -type semiconductor for example applying an external

negative voltage to the metal plate will attract holes to the semiconductor -oxide interface and a thin layer of positive charge will be formed at the boundary. The valence band E_V bends upward near the surface and is closer to the Fermi level. The Fermi level remains constant in the semiconductor bulk because there is no possible compensating current . The majority density depends exponentially on the energy difference $(E_F - E_V)$, so the band bending cause the accumulation of holes near the semiconductor surface. This case is called accumulation.

In the case that the external voltage has the same polarity with the majority carriers of the bulk ($V > 0$ for the p -type), the majority carriers will be pushed away from the interface and a negative space-charge region will be formed. The bands bend downward, the energy difference $E_F - E_V$ increase and the majority carriers are depleted. This case is called *surface depletion* and is stable when the voltage is small.

If the voltage increase further the depletion width will increase also. This is the over -depleted case. This situation is unstable. Thermally generated electron -hole pairs will be separated by the electric field in the space -charge region, the holes moving towards the bulk and the electrons accumulating at the semiconductor -insulator interface. With very low majority carriers concentration in the depletion case the minority carriers concentration increase and finally the minority carriers are becoming the majority carriers in the surface by applying higher voltage. For the p -type semiconductor and in the ideal case applying $V \gg 0$ will result to greater number of electrons in the surface than holes the surface is then inverted. The negative charge layer near the surface of the semiconductor is called inversion layer, and this is the inversion case .

In the most general case the work function of the semiconductor is different from the work function of the metal and the flat -band case it can only be achieved by applying an external voltage equal to this difference $V_{flat-band} = \varphi_m - \varphi_s$. A low $V_{flat-band}$ is a quality factor of the oxide and refers to a low contamination layer. In general (no ideal case) all the above configuration can be summarized for the p -type semiconductor as:

- accumulation $(V < V_{flat-band})$

  The majority carriers are attracted towards the insulator -semiconductor interface.

- Flat -band $(V = V_{flat-band})$ The semicoductor is at a uniform condition.

- surface depletion $(V > V_{flat-band})$ The majority carriers are repelled from the insulator -semiconductor interface forming an insulating depleted region, whose thickness depends from the applied voltage

- inversion $(V \gg V_{flat-band})$ The minority carriers become majority carriers near the insulator -semiconductor interface forming a thin conducting layer near the semiconductor surface and a larger insulating space -charge layer independent from the applied voltage.

Similar results can be obtained for the n -type semiconductor, the polarity however should be changed

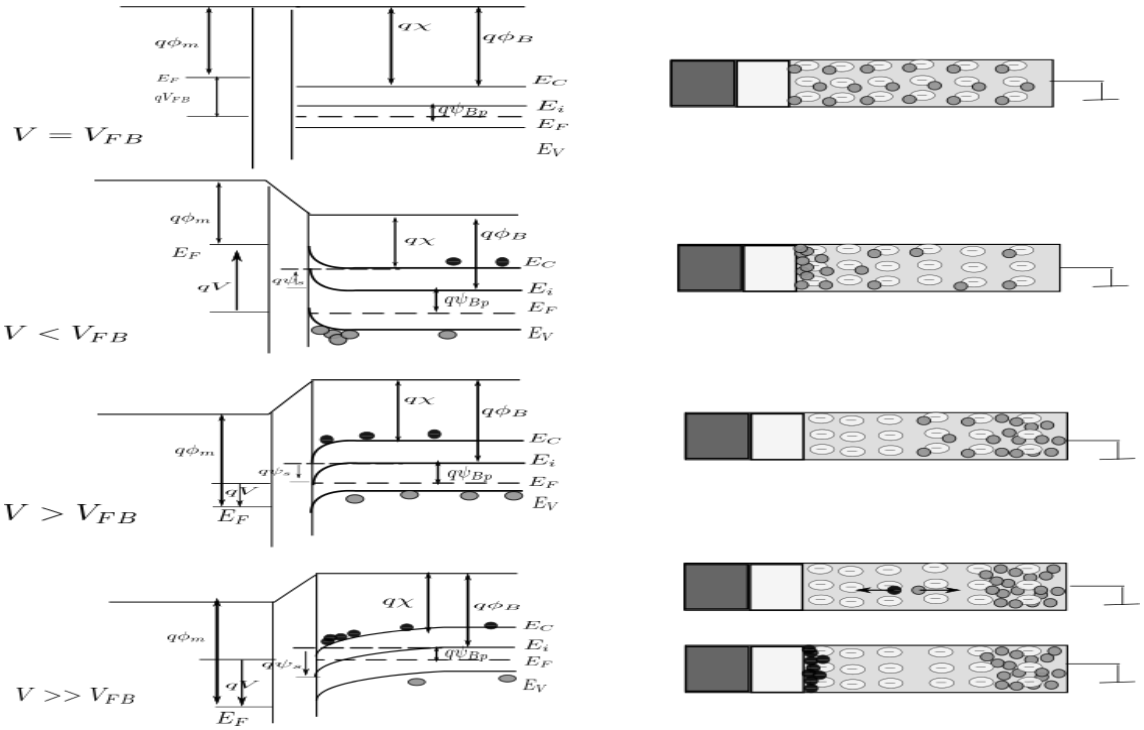

Figure 1.18: *The diagrams show the different cases of a MOS structure Flat -Band condition, accumulation, surface depletion, inversion. The left part show the energy bands for an n -type MOS. The right part show the free -charged carriers move inside the volume of the MOS in the 4 different cases.*

Capacitance-Voltage Characteristics

MOS structures on the sensor wafer provide diagnostic information not only for the semiconductor but also for the insulator and the insulator -semiconductor interface. CV characteristics provide means in order to check the oxide quality and also measure the oxide thickness.

As discussed in the previous section the capacitance depends on the Voltage that is applied to the gate (with respect to the body). There are four characteristic situations depending on the applied bias voltage. Capacitance -Voltage measurements are made by varying the bias voltage in order the MOS structure to pass through all those four situations changing from accumulation through the flat -band to depletion and inversion.

When the applied voltage is varying with time it is substantial to consider the time that the MOS structure needs in order to reach thermal equilibrium. In the accumulation case the time needed in order to reach equilibrium is relatively fast because it depends mostly in drifts and mobilities of the majority carries. The same apply to the depletion case. On the other hand, inversion can take a longer time to reach thermal equilibrium. This is due to the fact that inversion depends on the thermal production and recombination of the carriers at the depletion region. Thus, the time needed to reach equilibrium depends in the carrier generation lifetime of the semiconductor (approaching milliseconds to seconds).

The total capacitance C of the system, is a series combination of the insulator capacitance C_i

and the semiconductor depletion layer capacitance C_D.

$$C = \frac{C_i C_D}{C_i + C_D} \tag{1.63}$$

For a given insulator thickness d, the value C_i is constant and corresponds to the maximum capacitance of the system with value given by the relation below.

$$C_i = \varepsilon_i / d \tag{1.64}$$

The semiconductor capacitance on the other hand, depends on the bias and also on the frequency of the measurement.

Low-frequency measurements (quasi-static)

As the absolute value of the applied voltage increase, the MOS structure get from accumulation to depletion and finally to inversion. During this procedure, the displacement current is measured as a function of time. This displacement current, is the charging current of the capacitor. In the ideal case, no current can flow through the oxide layer but in real measurements a small amount of leakage current can flow.

Integrating the charging current over time, gives the charge stored in the MOS capacitor and consequently the capacitance with respect the voltage is measured.

The expected capacitance in each condition is expected to be:

- *accumulation* $C = C_i$

  The measured capacitance is just equal to the capacitance of the oxide layer. The majority carriers accumulate just beneath the surface. This leads to a capacitor with thickness equal to the thickness of the oxide.

- *depletion* $C_{Depletion} = \frac{C_i C_D}{C_i + C_D}$

  In this case the semiconductor is depleted, and majority carriers form a layer not near the surface of the semiconductor but underneath the depletion region. This leads to a series combination of the oxide capacitance C_i and the semiconductor capacitance C_D of the depletion layer. The total capacitance decrease. The depletion capacitance can be estimated by the relationship

  $$C_D = \frac{\varepsilon_s}{W_D}$$

  Where W_D is the depletion width, given by the relation below:

  $$W_D = \sqrt{\frac{\varepsilon_s^2}{C_{ox}^2} + \frac{2\varepsilon_s V}{qN_D}} - \frac{\varepsilon_s}{C_{ox}} \tag{1.65}$$

  With further increase on the absolute value of the voltage, the depletion region widens and the total capacitance continue to decrease until it reaches the minimum which corresponds to the maximum depletion width.

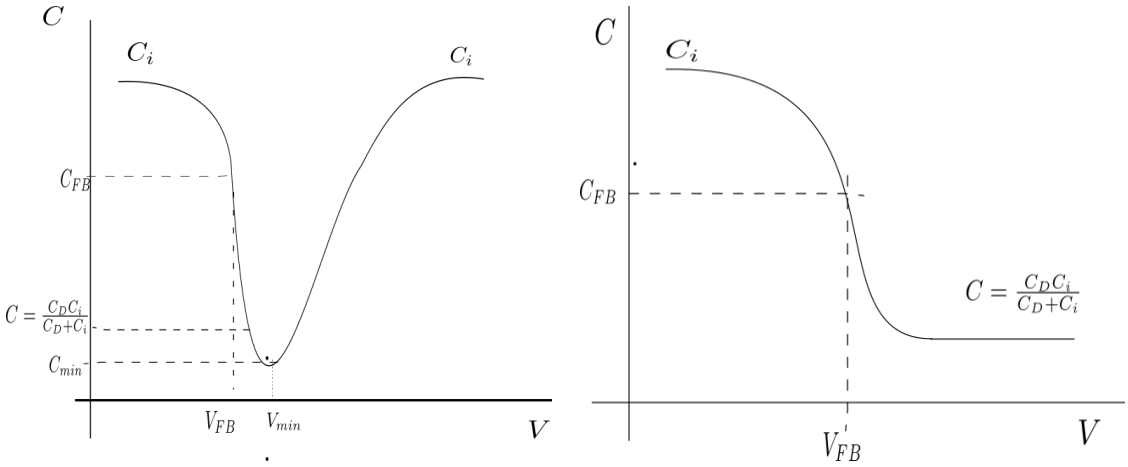

(α′) *CV curve for a p -type semiconductor with low frequency*

(β′) *CV curve for a p -type semiconductor with high frequency*

Figure 1.19

- *inversion* $C = C_i$

  The inversion layer that is formed, is gaining dominance over the depletion layer. The capacitance increase again in the inversion condition ,as the minority carries form an inversion layer at the surface of the semiconductor resulting to a larger capacitance. This increase can only be depicted in the low frequency measurement

A schematic representation of the CV characteristics with low frequencies is shown in 1.19α′

High Frequency measurements

High frequency CV measurements are made by superimposing a small AC signal on the voltage sweep and measuring the corresponding impedance directly. In the conditions of accumulation and depletion, the capacitance measurements are expected to have the same behavior as in the quasi -static (low frequency case).

Capacitance measurements are expected to have different behavior in the inversion condition. This is a consequence of the non -equilibrium state of the inversion condition. The generation -recombination rates can not keep up with the high signal variation in high frequencies. The Flat -Band Voltage is expected to be the inflection of the CV curve [11].

A schematic representation of the behavior of the CV measurements for high frequency is illustrated in the 1.19β′

Chapter 2

Silicon detectors in High Energy Physics

2.1 Introduction

Semiconductor detectors, and in particular silicon detectors, have unique properties that make them very suitable for the detection of ionizing radiation. The uniqueness of the silicon compared with other semiconductor are: the band gap energy (1.12 eV at room temperature) is small and it leads to a large number of charge carriers per unit energy loss of the ionizing particles to be detected. The density (2.33 g/cm3) of the silicon is high and it leads to a large energy loss per traversed length of the ionizing particle and high mobility (1450 cm2/Vs) of electrons provides fast charge collection time. Thus the silicon sensors are the most widely used for various sensing purposes such as imaging sensors in medical science, silicon tracking detectors in experimental particle physics, and etc.

The first idea of ionizing semiconductor detectors had been proposed from P. I Van Heerden around 1943. The idea was that if a crystal reacts with the photons as the photoelectric phenomenon explains it could also react with β and a particles.

Semiconductor detectors were used to energy spectroscopy for gamma ray and charged particles in 1960. They were consisted of one single sensor, often cooled by liquid nitrogen and they were optimized for energy resolution and count-rate capability. In the early 1980s a new development began and instead on emphasizing in energy resolution, these systems took advantage of the micron-scale patterning capabilities which came along with the new advances in the semiconductor technology which led to detectors with high position resolution

2.2 Silicon Tracking Detectors

Silicon detectors are used in order to provide a tracking mechanisms of the incident particles in experiments of High Energy Physics. A fundamental requirement in order to create a device with high position sensitivity is to have a situation that the created signal can be split in more than one electrodes. Each electrode then will collect charges in a ratio that depends on the position of the traversing particle.

2.2.1 Operation principle

The basic principle of a silicon tracking device is shown in the Figure 2.1. The device consists of one n-doped silicon substrate in which the one surface is segmented in strips with regions with highly doped silicon p^+. The segmented region of p^+ and the substrate n forms a highly doped diode. The device could be regarded as an array of p^+n diodes. A reverse bias voltage is applied to the silicon sensor and then depleted region is formed. The thermally generated free charged pairs of electrons and holes are swept from the electric field creating an ionization chamber. A position of passage of the charged particles is obtained by dividing the large area diode into many small strip regions, the location of the strips showing signals will provide information of position. The other surface is an n^{++} region which works as an ohmic contact.

When an ionizing particle traverses through the device it will lose part of its energy according to the Bethe-Bloch formula described in section 1.5. The part of energy that is lost is conversed by forming free pairs of electrons and holes. A minimum ionizing particle deposits about $100keV$ in a $380\mu m$ thick layer of silicon. With $3.62eV$ per electron hole pair, this corresponds to about 28000 electron hole pairs. The generated holes drift along the electric filed to the p^+ strips while the electrons drift to the n^{++} backplane. The $p+$ implants on top of the sensor will collect the signal and induce it to the aluminum strips which is connected with the read-out electronics where amplification and signal processing take place. The signal is generated by the movement of the charges in the electromagnetic field and is proportional to the carrier mobilities. The current that it is formed due to the carrier mobility is given by the equation 2.1 [11] [15].

$$J_0 = \frac{q_e}{d}\left(\sum u_n + \sum u_p\right) \tag{2.1}$$

where q_e is the elementary charge ,d the detector thickness and u_n , u_p are the drift velocities of e^- and h^+ . Then from equation 2.1 the maximum charge that can be collected is calculated by the time integral over the generated current.

$$Q_0 = \int_0^{tint} J_0 dt = \int_0^{tint} \frac{q_e}{d}\left(\sum u_n + \sum u_p\right) dt \tag{2.2}$$

where $t_i nt$ is the integration time.

The position that the particle penetrated the detector is then calculated by the pulse-height distribution of the affected strips. The charge that is created is not collected by only one strip but to several strips. Also the charge is shared by the individual strips with capacitive coupling

The layout of the detector is designed in order the segmented areas to form strips or pixels. Those are the most commonly used layouts of silicon detectors. The strips or pixels are formed of a sandwich of a $p+$ or $n+$ semiconductor with a SiO_2 layer in the middle and metal layer above

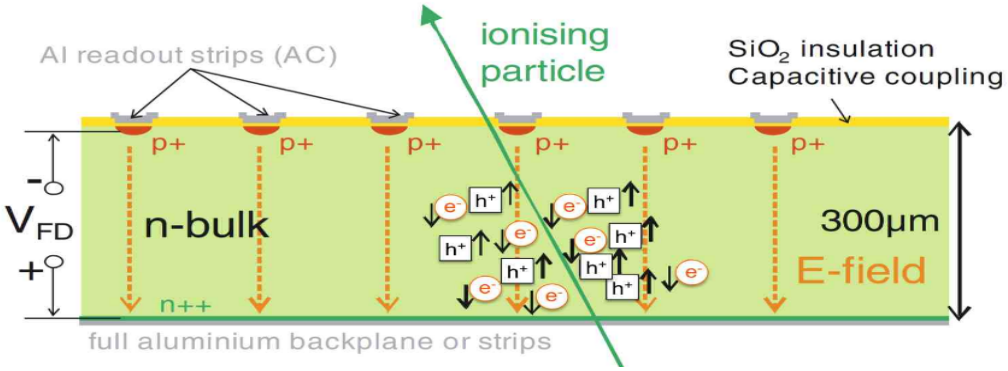

Figure 2.1: *Working principle of a silicon strip detector [11].*

the SiO_2. this structure forms a capacitor integrated within the detector. This device is then called an AC-coupled senor (or DC-blocked). Otherwise is called DC-coupled and the capacitor is integrated to the read out chip or in-between. In the DC-coupled there is a direct contact with the p+ strip. The first silicon detector designed for High Energy Physics experiments (NA11) was a dc coupled detector. But the AC coupled silicon detector is considered a new standard for all High energy experiments. A 3D schematic of an AC-coupled sensor is shown in the Figure 2.2.

AC coupling, also known as capacitive coupling is the connection of a signal from one circuit to another in a manner that rejects DC components. The propagation of the AC signal can be visualized as a periodic charging and discharging of the capacitor. Capacitive coupling of electronics to silicon detector (AC-coupled) has the advantage of shielding electronics from dark current. The coupling capacitor is defined between aluminum strips and the $p+$ implants and the inter-strip capacity between neighboring strips.

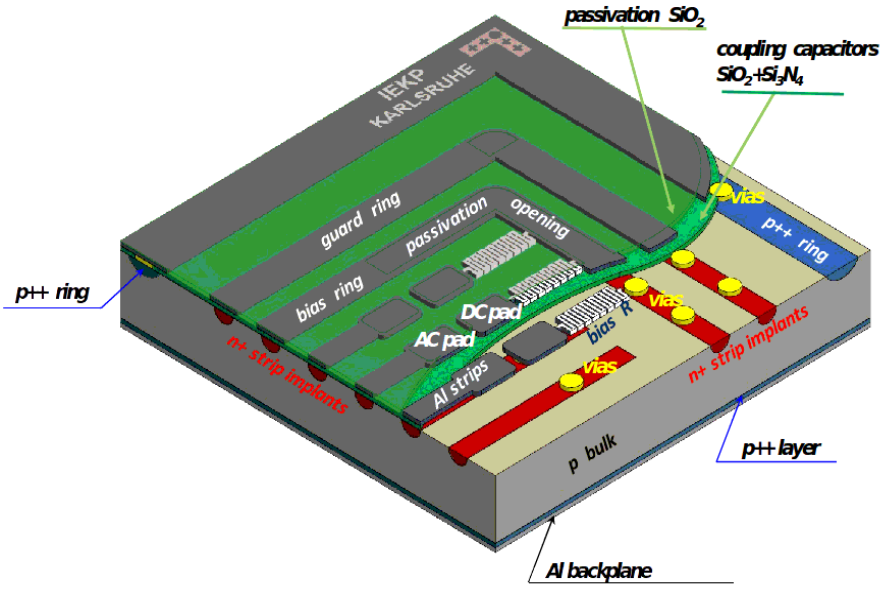

Figure 2.2: *3D -schematic of an n-type silicon strip sensor [11].*

2.3 Componets of Silicon strip detectors

Strip implants

The most usual structure for the use of silicon detectors in high energy physics was an p-on-n structure with $p+$ implants on a n-substrate. This structure was used for the CMS experiment. However the n-on-p structure has shown promising results for radiation hardness. One advantage of the *n-on-p* structure over the more conventional *p-on-n* is that the strips collect electrons which have slightly larger trapping time and mobility in silicon compared to holes.

Backplane

The back side of the detector is not segmented and it has a n^{++} layer in order to provide an ohmic contact between the sensor bulk and the aluminum layer on the backplane to which a high potential can be applied. The $n++$ defines the volume and prevents high field in the real cut edge regions.6). The heavily n-doped layer is not depleted since the voltage in the lower doped bulk region drops. For this reason, the effective readout thickness of the sensors is less than the wafer thickness.

Bias ring

The bias ring circulates all the active area of the detector and with the backplane consist the main contacts in order to apply bias voltage. The bias ring produce a homogeneous potential for all strips. It can be connected with a bias voltage source and provide biasing to all the strips and the backplane to the ground or it can be connected to ground voltage and the backplane to the bias voltage source. It is connected with the strips with polysilicon bias resistors.

The guard ring

The guard ring splits the front surface of the detector in two areas, one central area used as the sensitive area of the detector, and one outer surrounding area that it consists by the guard ring and the $n++$ ring. The guard ring structure is devised in order to clear the device from surface leakage current effects and also to shape the field inside the sensitive area of the detector. The guard ring geometry should also establish a uniform potential drop along the silicon surface in order to avoid local avalanche breakdowns at voltages much lower than the bias voltage required for detector operations. Since no or only very small voltage drop exist between the active area of the detector and the guard ring there is no current that flows outside the central region.

The guard ring encloses the bias ring and like the bias ring it has a $p+$ ring implant and an aluminium ring which are connected to each other with vias. Its inner side has to shape the electric field around the bias ring. Together, the bias ring and the guard ring form an electric field in order to obtain an electric field for the outer strips in the same way as an electric field is provided for the inner strips by their neighbors The outer side of the guard ring has to adjust the electric field distribution towards the edges of the sensors. In contrast to the bias ring, the guard ring is operated in floating mode, i.e. it is not connected to a preset potential. Normally, multiple guard ring designs are used to adjust the voltage drop step by step. Thanks to the metal overhang

design (see Section 4.3) just one extended guard ring is necessary for smoothly adjusting the potential [16].

Sensor edges

A $n++$ ring encloses the sensitive area including the guard ring and the bias ring. It is operated in floating mode like the guard ring and its mission is to avoid the flow of high currents from the outer edges into the active inner area of the sensor. The cracks caused by the cutting process at the edges introduce energy levels in the forbidden gap leading to an increase in the leakage current. The $n++$ ring implant is connected to an aluminum structure above the isolating layer which contains special marks for alignment and the strip numbers.

Bias resistor

The polysilicon resistor connects the bias ring with the strip implants. Due to thermal noise that depends at the factor $\sqrt{\frac{k_B T}{R}}$ the bias resistor must have a high value. If the resistor varies between individual strips this will produce a voltage drop between them and shape a non-uniform electric field. These ohmic resistors are made of heavily doped ploy -crystalline silicon. The lower resistor limit of the bias resistor is determined by noise considerations. For CMS a specification is 1.0-2.0 $M\Omega$ with a spread within one sensor 0.3 $M\Omega$ [11].

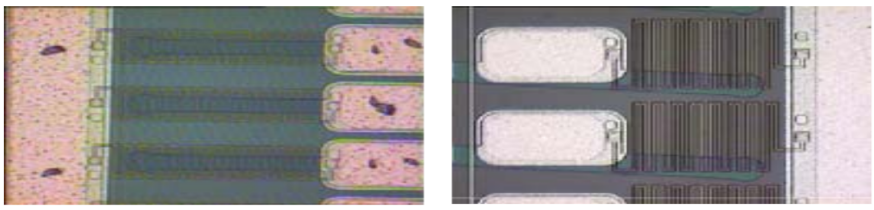

Figure 2.3: *Close view of polysilicon bias resistor of the CMS sensors [11].*

DC pads and AC pads

The pads are used for electrical access to the strips implant and the metal layer. The width of the pads is about twice as large as the strip width.

There are two kinds of pads, which are also is shown in Figure 2.2. DC pads provide electrical connection directly to the implant. Their existence is not actually for the operation of the detector but they are used for probing measurements. On the other hand AC pads are essential components for detecting operations, as they are used to provide electrical connection to the readout metal layer. The readout chip is bonded to the AC pad area.

Intermediate strips

Intermediate strips allow the construction of detectors with improved resolution with fewer read out channels. Having two many read-out channels is cost effective and work intensive. Also is to difficult to have read-out channels with very small pitches.

The signal received from the indeterminate strips is capacitively coupled to the two nearest read-out strips. The signal is distributed more evenly in the strips than in the case of a wide read-out strip geometry. Charge division reduces the read-out channels as only a fraction of strips is connected to the amplifiers. The charge collected from the interpolated strips is shared to the read-out strips according to the position.

This is accomplished with capacitive charge division which takes advantage of the inter strip capacitance that is created due to the geometrical structure. As described above the inter-strip capacitor that is formed can be charged end discharged periodically according to the signal propagation thus signal shearing can be achieved. The strip to ground capacitance and the capacitance due non-neighboring strips (second neighbors) will distort the signal from linearity.

The intermediate strips are kept to the same potential as the read-out strips in order to collect signal and achieve charge shearing. This can be achieved by connecting very high resistors to between the intermediate strips and the read-out strips.

isolation: p -stop and p -spray

Fixed charges in the SiO_2 interface attract mobile electrons. This forms an accumulation layer just beneath the interface of $Si - SiO_2$ which could sort out the strip implantations. In order to minimize this effect, there are some isolation techniques that must be used.

An additional separate *p+* implantation is used surrounding the strips. This technique is called *p -stop*. The additional *p+* implants dissipate the accumulation layer. Thus the additional implants should cover as much area is possible between the strips without contacting them. This doubles the number of structures that are needed and considering also the intermediate strips that could be in the sensor this technique increases the number of structures.

Another technique is the *p -spray* technique. In this technique the whole area between the strips is implanted forming a diffuse layer of *p-dopants*. This option has the advantage of not introducing more structures. However the *p -stop* technique is easier and more controllable during the manufacturing process which make the *p -stop* technique more widely used. Also a combination of both techniques can be used.

Strip isolation can also been achieved by increasing the Al strip widths in order to cover some area in the gap between the strips. The applied potential will repel the accumulated electrons from the interface. The Figure 2.4 describes the the different isolation methods.

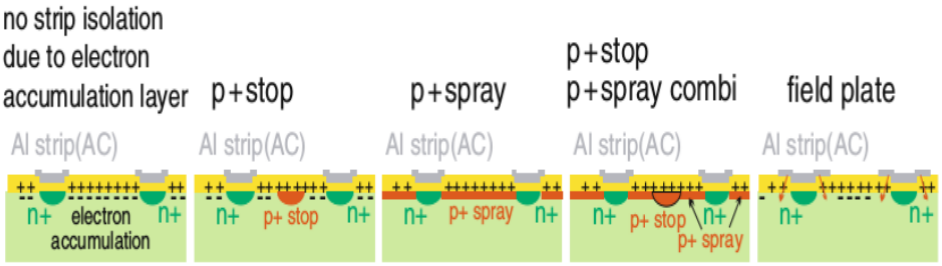

Figure 2.4: *Basic techniques to avoid and repel the accumulation layer of electrons that is formed due to fixed oxide charges in the SiO_2. [11]*

This techniques are also an essential part of the $n-on-p$ sensors that are currently under investigation for the phase 2 upgrade of the CMS tracker.

Passivation layer

To protect the sensor from environmental effects such as mechanical damages from scratches or chemical contamination of the silicon bulk, an additional layer of SiO_2 is created in the top of about $1\mu m$ thickness. At certain areas the passivation layer is etched, to provide an electric contact to the underlying metal layer.

2.4 Position resolution and localization

The spatial resolution of micro -strip detectors depends on both physical and external parameters. The physical parameters are the statistical fluctuations of the energy loss and the diffusion of carriers during the drift. External parameters include the readout strip pitch and the noise of the readout electronics.

Due to secondary ionization the distribution of the energy loss is asymmetric. Also the electrons and holes diffuse during the drift to the electrodes by multiple scattering with the lattice. The distribution of the charge carriers around the track can be described by a Gaussian distribution. The charge clouds arriving at the strips are considered to be Gaussian with a standard deviation given by 2.3 [11]:

$$\sigma_{diff} = \sqrt{2Dt_D} \tag{2.3}$$

where D is the Diffusion coefficient and t_D is the drift time which depends in the type of carrier as it is inversely proportional to the mobility. The charge is spreading a long distance from the particle track. The signal will be collected on more than one strip due to diffusion and secondary ionization.

The key of position sensitive silicon detectors is the segmentation of the silicon wafer. The geometrical characteristics of the read-out segments such as the width of pixel w and the separation width between adjacent pixels s for a pixel-detector or the pitch $p = w + s$, the sum of the width and separation between adjacent strips for a micro-strip detector are very important and must be very carefully chosen in order to have the acquired position resolution and signal to noise ratio. Also the ability of charge sharing between the strips is an important parameter of good spatial resolution

The precision of the potion measurement is defined as the root-mean-square distance of the measured coordinate from the true hit position.

If the signal charge is collected in a single strip or pixel (the track passes throw a specific strip or pixel) or for digital readout (binary form) the measurement is considered the center of th hit-strip. The position resolution is then calculated as

$$< \Delta x^2 > = \frac{1}{p} \int_{p/2}^{p/2} x^2 dx = \frac{p^2}{12} \Rightarrow \tag{2.4}$$

$$\sigma_x = \frac{p}{\sqrt{12}} \tag{2.5}$$

It is defined from the geometrical characteristics of the read-out segments. Digital(yes/no) readout is used when there in no need for energy information and when a large positional resolution is sufficient.

A spatial resolution significantly better could be obtained for tracks that generate enough charge on two strips. The passage of a particle track in the detector is seen as a charge cluster of adjacent strips. In this case the resolution and the validity of the position measurements is dominated by the signal to noise ratio. The signal should be shared between the two strips or pixels in that way that both segments receive signals that exceed the threshold value. The most precise position measurements are made for tracks that traversing through the middle of the detector where the signal is equally shared between the segments. The localization is made by using the center of gravity method or by using cluster finding algorithms depending on the geometry of the detectors and the track angle namely n-algorithms. More details can be found at [17] , [18] , [19] , [20]

In the center of gravity method the position is calculated by the relation:

$$x_{cog} = \frac{\sum_{i=0}^{i=l} S_i x_i}{\sum_{i=0}^{i=l} S_i} \tag{2.6}$$

where x_i is the position of the ith strip included in the cluster and S_i the signal on that strip. If the cluster width is equal to 1 then the position resolution is reduced to the equation 2.5.

However if the particle pass throw the implantation all the charge remain within the strip. Only a small portion of the charge will be capacitively coupled to the two neighboring strips. So in order to optimize the resolution for a given pitch the implantation width should be small. On the other hand if the implantation width is very small there will be large gaps between implantations which can cause loss of charge signal.

The pitch of the detector is chosen such that the resolution of the detector is small. Also the pitch can not be made arbitrarily small because this will increase the input capacitance seen from the read-out electronics which will lead to a noise increase.

2.5 Sensor Parameters

2.5.1 Global Parameters

Total Current

When a reverse voltage is applied to a Si detector, a small amount of current flows throw the detector, this is called leakage current or dark current just like the leakage current of a p-n diode. Section 1.6.1

Leakage Current is a source of noise and deteriorates the overall performance and quality of the sensor. Thus leakage current should be kept as low as possible. The leakage current is proportional to the depletion layer thickness d of the sensor which is proportional to $\sqrt{V_{FD}}$, where the V_{FD} is the depletion voltage. After reaching V_{FD} the leakage current should be constant. Deviations from this rule indicate bulk impurities [11].

Two types of leakage currents appear in reverse biased detectors: leakage current in the bulk and surface currents.

Bulk currents derives from thermal electron hole generation. This carries can recombine with existing defects acting as traps. The sensors in a high energy experiment environment suffer from harsh radiation which generates new traps in the bulk influencing the leakage currents. Surface leakage currents result from manufacturing processes and surface damage like scratches. Bulk leakage current is strongly dependent from the temperature, while surface currents are less dependent. More details about temperature dependence of the bulk leakage current can be found at[21]. Therefore the whole CMS tracker is cooled down to about -10℃. After the upcoming two upgrades the CMS tracker will be cooled down to even -20℃ improving the sensor efficiency.

Bulk and surface damage are both increased due to radiation. Radiation creates bulk defects which leads to apply higher voltage to fully deplete a device. But the increase of voltage also negatively influences the leakage current. This fact led to irradiation studies of different silicon processing techniques .

Depletion Voltage

.

One of the sensor parameters which characterizes the sensors performance is the full depletion voltage respectively the sensor bulk capacitance.

As explained in Section 1.6.1, the full depletion voltage V_{fd} of p-n diode is defined by the depletion width w and it can be considered as a plate capacitor in the fully depleted case. This gives a characteristic behavior of the capacitance over voltage expressed in the following equations.

$$C_{bulk} = \begin{cases} \sqrt{\frac{q\varepsilon_{Si}|N_{eff}|}{2V_{bias}}} & with \quad V_{bias} \leq V_{FD} \\ \frac{\varepsilon_{Si}}{D} & with \quad V_{bias} \geq V_{FD} \end{cases} \tag{2.7}$$

where N_{eff} is the effective charge carrier density (the number of donors minus the number of acceptors), q is the absolute value of the electron charge and $w = D$ is the depletion width.

The value of V_{FD} is directly observable in a CV plot. The capacitance becomes constant after reaching the the full depletion voltage and the curve flattens.

The Depletion voltage mainly depends on the resistivity ρ and thus from N_{eff}. The applied voltage influence the collection time of the ionized electron-hole pairs. Also in large experiments in high energy physics like CMS a lot of sensors are connected to one high voltage power supply. Therefore V_{FD} should not vary and in an ideal case should be homogeneous to all the sensors [11].

In the case of strip array which is closer to the detector design the full depletion voltage varies from the one of planar diodes due to the strip geometrical deviation from a full plate capacitor.

A semi-analytical solution of Poisson's equation predicts that [22], [23].

$$V_{FD} = V_{FD0}\left[1 + \frac{2p}{d} f(w/p)\right] \tag{2.8}$$

where V_{FD0} is the depletion voltage of one planar diode and V_{FD} is the detector depletion voltage, p and w is the pitch and width respectively. The function $f(w/p)$ is a correction function expressed as:

$$f(x) = -0.00111x^{-2} + 5.86 \cdot 10^{-2}x^{-1} + 0.240 - 0.651x + 0.355x^2 \tag{2.9}$$

where x=w/p. Hence, compared to a diode one expects a higher depletion voltage and a lower backplane capacitance for the strip, this correction becoming smaller for larger values of w/p

2.5.2 Strip Parameters

The strips in the full depletion case define parallel plate capacitors between themselves, the backplane, the Al.

In double-sided, AC-coupled silicon micro -strip detectors, the signal to noise ratio is a function of detector capacitances : the coupling capacitance influences the signal strength, and the interstrip and backplane capacitances the noise level . In addition, the resistance of the metal strip can influence the signal strength for fast shaping

Coupling Capacitances ($C_{coupling}$)

Layers of SiO_2 and Si_3N_4 cover the whole textured side of the bulk and isolate the implants from the aluminum strips above. The implant strips are then AC coupled to the readout electronics.

The coupling capacitance is formed between the implant with the Al and the read-out electronics. As mentioned previously the capacitor that is formed is used to propagate the signal from the implants to the read-out by periodically charging and discharging. This capacitance has to be large in order to avoid parasitic currents. Also the signal is directly proportional to the coupling capacitance. A very large capacitance means a thin isolation layer between the Al strip and the implants [11]. For noise reasons, the magnitude of the coupling capacitance must exceed the sum of the two interstrip capacitances between two adjacent strips and the strip's capacitance between the strip implant and the backplane

Since the capacitance has to be large, the thickness of the dielectric has to be as low as possible. For this reason it is not possible to apply a high voltage drop at the coupling capacitances.

Backplane Capacitance (C_b)

The backplane capacitance is formed between the implant strip and the backplane. Plotting C_{back} as a function of the bias voltage for one can identify the depletion voltage. It is an excellent identification tool for strip defects. A broken strip show a lower capacitance. By measuring the values for every single strip approximate the load uniformity to the preamplifier.

In literature, a semi-analytical solution of the Poisson's equation predicts a backplane capacitance of a micro -strip detector dependent on the segmentation [22].

$$C_{back} = \varepsilon_0 \varepsilon_{si} \frac{p}{d} \left(\frac{1}{1 + p/df(w/p)} \right) \tag{2.10}$$

where ε_0 is the electrical permitivity in vacuum, ε_{si} the electrical permitivity in silicon,p is the implant pitch and d is the detector thickness. The function $f(w/p)$ is a series function of w/p.

For the backplane capacitance measurements all the strips are bonded together and the capacitance is measured between the strips and the backplane. A special circuit is used to decouple the high voltage from the input of the meter.

Inter-strip Capacitance (C_{int})

The inter -strip capacitance is the main contributor to the noise. The implant of a strip does not only have a capacitance towards the backplane of the sensor but also to other strips. This inter -strip capacitance determines the charge sharing between the strips and, together with the backplane capacitance of a single strip, the load capacitance of the amplifier and thus the detector noise. It is therefore vital to understand the behavior of the inter -strip capacitance before and after irradiation, as it is sensitive to surface damage that deteriorates the oxide and consequently decreases strip isolation. The inter-strip capacitance (C int) has a basic contribution the capacitance load into the amplifier and thus to the detector noise. Compared to the coupling capacitance the values for C_{int} have to be small, with a ratio between $C_{int}/C_{coupl} = 1/30, 1/60$ [11].

In the range $0.10 < w/p < 0.50$ a good approximation is given by

$$C_{intd\to\infty} = \left(0.8 + 1.9 \frac{w}{p} \right) pF/cm \tag{2.11}$$

This equation refeq:Cintaprox assumes a very large detector thickness and cannot be applied in the planar case which is the most common in the use of silicon detectors in high energy experiments. The approximation give poor results for $pitch > 120\mu m$. A better approximation for the silicon sensors of CMS was found to be 2.12:

$$C_{intd\to\infty} = \left(0.03 + 1.62 \frac{w + 20}{p} \right) pF/cm \tag{2.12}$$

Total Capacitance ($C_{tot} = C_b + C_{int}$)

The total capacitance is then the sum of the total inter -strip capacitance of a strip against neighbor strips and the backplane capacitance. This is the total capacitance load to the read-out amplifier. It is a main source of noise. A single strip typically shows a total capacitance of 1 $pFcm^{-1}$. Total capacitance is a major source of noise and the CMS set a limit of $1.2pF/cm$ for all strip sensors [11].

Investigations on prototypes for the CMS silicon tracker [24] [25], [26] [22] revealed that the actual value of the total capacitance with constant w/p ratio (where w is the width strip and p is the pitch(width+separation width)) is independent on the detector thickness in the range of

300-500 μm thickness, because the inter -strip capacitance decreases with the same manner as the backplane increases and vice versa. However, the total strip capacitance does depend on the aspect ratio of the strip implant. The total capacitance and the dependence from the strip width w and the pitch p can be shown from the empirical equation

$$C_{tot} = \left(0.83 + 1.67\frac{w}{p}\right)\left[\frac{pF}{cm}\right] \tag{2.13}$$

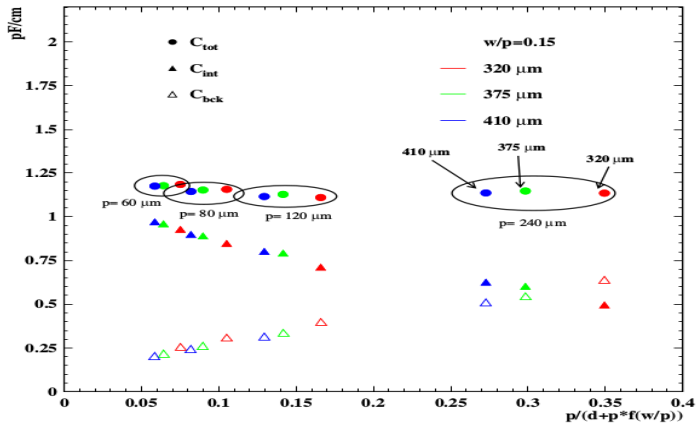

Figure 2.5: *Backplane capacitance Inter -strip capacitance and the sum of two with different w/p ratio [24].*

For measuring the total strip capacitance we bond all strips together, leaving one, in the center, free. The bias voltage is applied to the backplane of the sensor and the capacitance is measured between the central strip while all the others are kept to ground potential.

The measured total strip capacitance,C_{tot}, is related to the inter -strip capacitance, C_{int} and to the backplane capacitance C_b by the equation

$$C_{tot} = 2C_b + \frac{n-1}{n}C_{int} \tag{2.14}$$

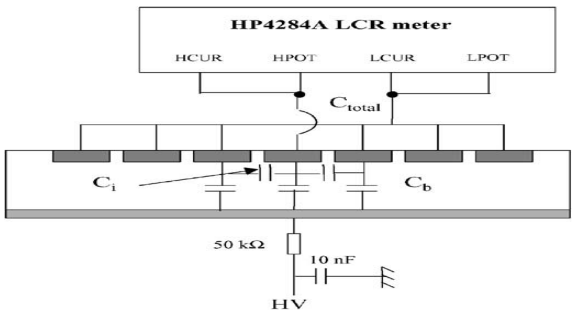

Figure 2.6: *Total Strip Capacitance measurement Schematic [27].*

Inter-Strip Resistance

In order to attain an isolation between the strips a high resistance between them is needed. R_{int} should be of several $G\Omega$.

The value of the inter -strip resistance along with the inter -strip capacitance determines a number of strips over which the charge produced by an ionizing particle is distributed and, consequently, the spatial resolution of the detector. Inter -strip Resistance depends to a lot of parameters such as the oxide static charges or the passivation and the accumulation of charge carries in the surface.

2.6 Hybrid Pixel devices

In the LHC environment and close to the interaction point where the number of incident particles becomes very large the probability of having two tracks hit the same strip sensor is high. Making the use of the strip detectors in the region close to the interaction point not very capable to determine which strip corresponds to which particle.

Pixel detectors are more robust to this environment since they offer high signal to noise ratio due to the small capacitance at the input of the amplifier due to the small size of the pixels in contrast with the strips. The name is derived from their geometry. They consist of small quadratic or rectangular sensor elements, called pixel, and provide inherent two dimensional spatial resolution. All elements are read out separately by a dedicated amplifier. The elements have a size in the order of $100\mu m$. This results in a very high pixel density per sensor area. The sensor electrodes are patterned as a checkerboard forming a monolithic matrix of reversed bias diodes. Pixel detectors may be broadly categorized into two broad varieties: Charge Coupled Devices and Active Pixel sensors, the latter can be sub-dived into monolithic devices and hybrid detectors.

The contact between the sensor pixel and the electronics is not possible to be achieved with wire-bonding as in the case of the strip detector. In this case the detector and the electronics are fabricated on different wafers In this technique one solber ball(bumps) is used to connect the pixel of the detector with the electronics.

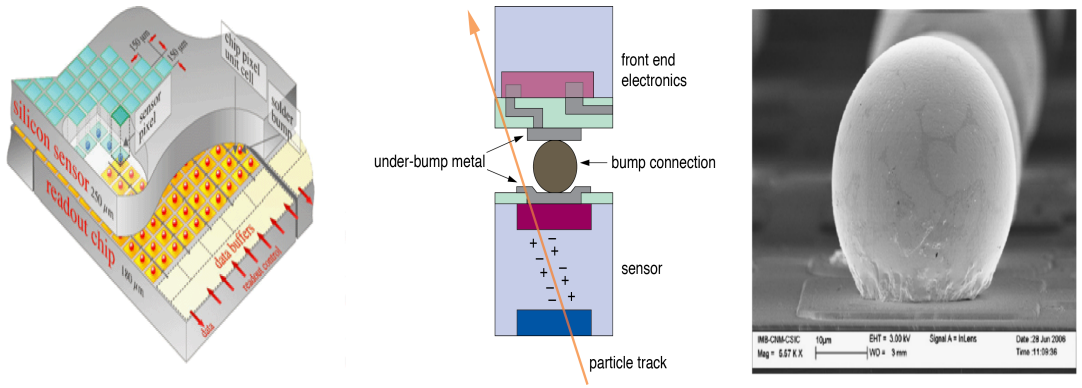

(α′) (β′) (γ′)

Figure 2.7: Hybrid Pixel detectors
Schematic view of pixels detector 2.7α′ [28].2.7β′. Close view of sober ball 2.7γ′ [29].

2.7 Read-out electronics

A crucial element for a detector final signal is its read-out electronics, which amplifies, shapes the sensor signal and converts it into a digital sequence. The basic processing stages of the signal throw he detector are shown in Figure 2.8. All semiconductor systems include the same basic operations. The signal of each sensor must be amplified and processed.

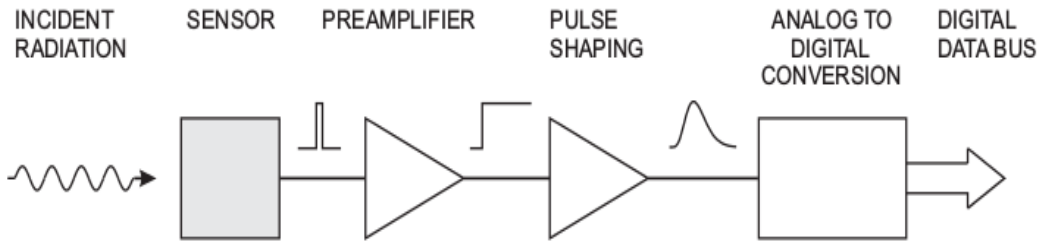

Figure 2.8: *Basic detector functions. Energy is absorbed in the volume of the detector and is transformed into an electrical signal (square pulse). The signal is amplified by a preamplifier, then fed to a pulse-shaper and then to an analogue to digital convert. [3].*

- *Sensor*

  The sensor converts the deposited energy of the particle to an electrical signal. The number of electron-holes pairs are proportional to the absorbed energy. The free charged carriers are swept by the high voltage applied to the electrodes under the influence of the external field which result to an induced low signal current in the external circuit. By integrating the signal current the total charge is obtained.

  Preamplifier

  The signal produced by a sensor is typically a short current pulse: since the total charge, given by the integral of the signal current I(t), contains the information about the energy deposited in the sensor, one needs to integrate the current. Also the signal charge pulses can be quite small of about 50 aC ($5 \cdot 10^{-17} C$) for x-rays and 3.6 fC for a minimum ionizing particle for a 300 μm thick silicon detector. So the first step is to amplify and integrate the small signal current [3].

  The basic component that is used for amplifying the signal in silicon detector systems is the charge sensitive amplifier (CSA) or feedback amplifier. A scheme of an ideal charge-sensitive amplifier is shown in Figure 2.9. It , consists of an inverting amplifying circuit which (in the ideal case)delivers an output voltage proportional to the input ($Uout = -AU_{in}$) it is characterized by a high input impedance $R_i \to \infty$ and a feedback capacitor C_f . In addition, a high-resistance feedback or a switch is needed in the feedback loop, in order to bring the circuit into its operating condition. C_D represents the capacitive load of the detector at the input, C_i the input capacitance of the amplifier.

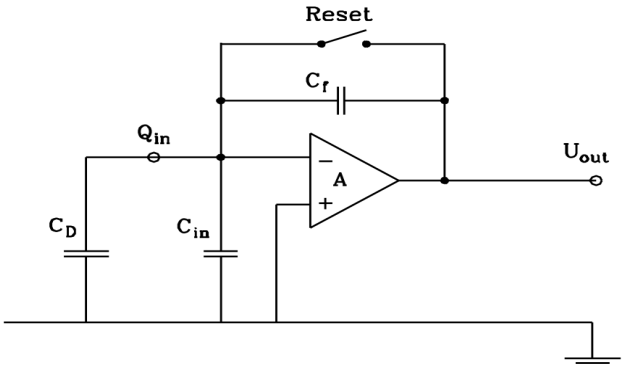

Figure 2.9: *The Charge sensitive amplifier[5].*

A signal Q_i at the detector will result in an output voltage change of:

$$u_{out} = -\frac{Q_{in}}{C_f + \frac{C_D + C_i + C_f}{A}} \longrightarrow \frac{-Q_{in}}{C_f} \tag{2.15}$$

A more realistic amplifier, instead, responds to a current pulse with a finite speed and then its response affects the pulse shape: the output voltage cannot be a step but is moduled by a negative exponential and depends on the circuit time constant $\tau = R_L C_o$, since the internal capacitances of the amplifier have to charge up before allowing the output voltage to change. The response of a signal step of magnitude V_o is:

$$u_o(t) = \frac{-Q_{in}}{C_f}(1 - e^{-t/\tau}) \tag{2.16}$$

Pulse Shaper

The basic operation of a pulse shaper is to improve the signal to noise ratio. The noise spectrum expands to a much larger spectrum than the noise due to the fact that it depends in uncorrelated events. We can therefore use appropriate filters to limit noise to the benefit of the signal. However Changing the frequency response of a pulse changes and the time and thus the shape of the pulse, this process is called signal shaping. The reduction in signal bandwidth improves the signal to noise ratio but also increases the duration of the pulse. Thus a square pulse that is formed by the detector is transformed into a broader pulse with a characteristic peaking time T_p 2.10.

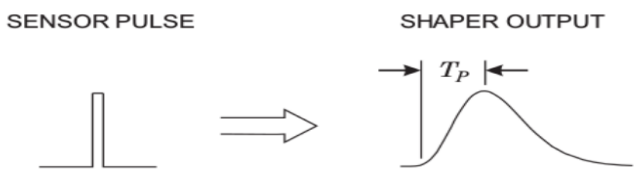

Figure 2.10: *The signal coming from the detector is transformed into a larger pulse with a characteristic rise time (T_p) [3].*

Usually we are interested in measuring multiple pulses successively and often in a very high rate . Therefore the large width of a pulse leads to the pile-up effect in which piece Part of the pulse interfere with the next pulse by increasing its amplitude. If The pulse rate is high, this leads to its erroneous result of the amplitude This phenomenon can be reduced by reducing the pulse width.

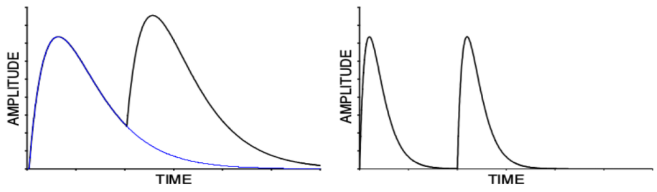

Figure 2.11: *Amplitude pile-up occurs when two pulses overlap. Reducing the shaping time allows the first pulse to return to the baseline before the second pulse arrives [3].*

Signal shaping (or pulse processing) has two conflicting objectives:

- reducing the bandwidth to match the measurement time, since a too large bandwidth increases the noise without increasing the signal.
- avoiding signal pile-up, i.e. constraining the pulse width in order to mea- sure successive signal pulses without overlapping. Reducing the pulse duration increases the signal rate but leads to heavier electronic noise contribution.

Shaping can be done internally to the preamplifier stage or by using of a RC- CR filter (eventually in a sequence $(RC-(CR))^n$). A front-end sequence with preamplifier (first stage) followed by a shaper is shown in Figure : the charge sensitive amplified receives the signal from the sensor, the second stage is a CR (high-pass) filter or differentiator which brings the CSA output back to the baseline with a quick and sharp fall, while the third stage is a RC (low-pass) filter or integrator which softens the signal variation around the maximum.

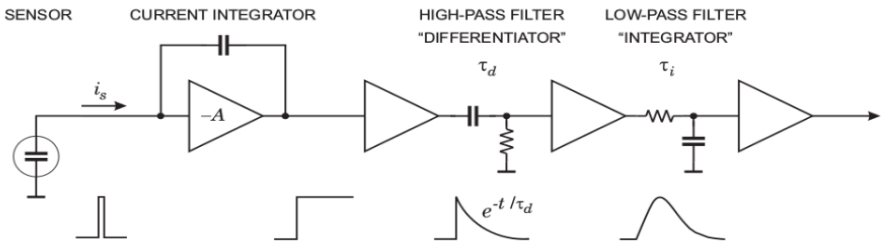

Figure 2.12: *Components of the pulse shaping system. The signal is integrated from the sensor which leads to a step pulse with long decay. Next the signal puss throw the high-pass filter (differentiator) which limits the pulse width and the low pass filter which increases the rise-time to form a pulse with a smooth cusp. [3].*

2.8 Radiation damage

The high flux of particles in the tracker can cause malfunctions to the detectors due to the radiation that is deposited to them. The radiation effects at the silicon detectors are called radiation damage. In order to ensure the proper operation of the detectors throughout the hole lifetime of an experiment the radiation effects on silicon detectors must be well understood. The mechanisms that have been taken into account is [11]:

- the damage to the lattice created by traverse particles.
- the following diffusion process annealing

Traversing particles interact with the electron cloud, but also with the nuclei in the lattice. The interaction with the electron cloud is in fact used for detection but the interaction with the lattice can lead to permanent material changes. These defects can be simple empty lattice locations (vacancies) or silicon atoms between lattice locations (interstitials), or more complex defects also in connection with impurity atoms present in the bulk.

These defects introduce new energy levels within the band gap between the valence band and the conduction band of the semiconductor. These additional levels are the cause for the change of detector parameters, i.e. the increase of the leakage current, the modification of the effective doping concentration, and the creation of trapping centers reducing the lifetime of the charge carriers.

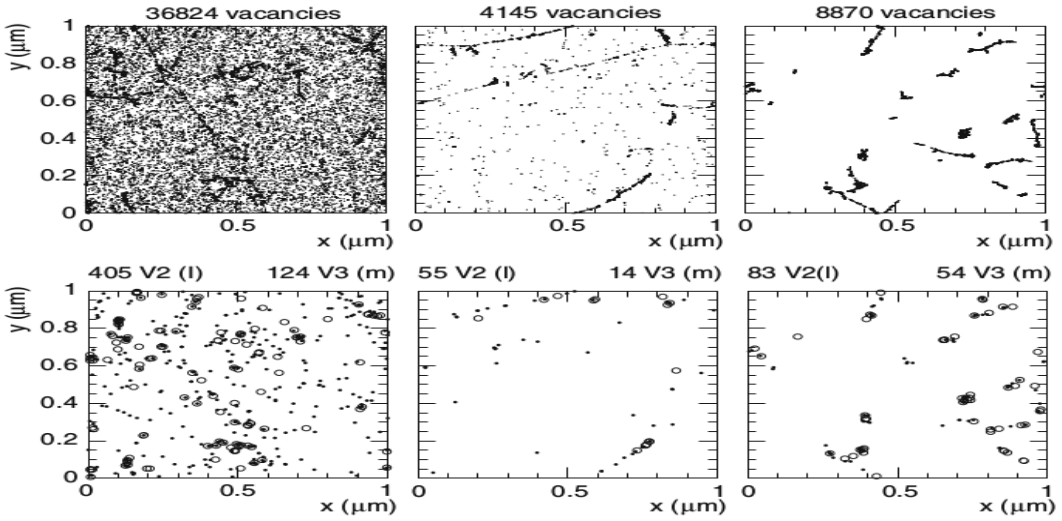

Figure 2.13: *Simulation of defect formation with radiation and diffusion. The upper three simulations show the microscopic picture of defect distribution. About 10 MeV protons (left) produce a quite homogeneous vacancy distribution, while more energetic protons with 24 GeV (middle) form more clustered and discrete defects. Neutrons with 1 MeV (right), interacting only due to strong interac- tion, do produce more isolated clustered defects. . The lower three figures are displaying the final position of the defects after a certain annealing time. [11].*

Leakage Current

The increase of the leakage current can be well described by equation:

$$\frac{\Delta I}{V} = a\Phi_{eq} \tag{2.17}$$

where a is called the current-related damage rate and Φ_{eq} is the particle flux normalized to 1 MeV neutrons. This a convenient definition to enable the comparison of the damage by different particles and energies.

The particle flux increase the leakage current linearly. This allow the usage of several diodes to determine the particle flux by the increase of the leakage current [11]. The measure increase of the leakage current depends on the ambient temperature during the irradiation and during the period before the measurement is taken.

Annealing effects decrease the currents, until saturation is reached. The constant α describes the annealing behavior derived and it is derived from measurements, is about $\alpha \sim 4 \cdot 10^{17} A/cm$ (after 80 minutes annealing time at $60^o C$) [11]. This number is valid for all standard structures and silicon materials tested. The annealing decreases the leakage current and this therefore is beneficial. In Figure 2.14 the linear dependence of the leakage current increase with the particle flux is shown (left) and dependence of the α parameter with the annealing time to the right.

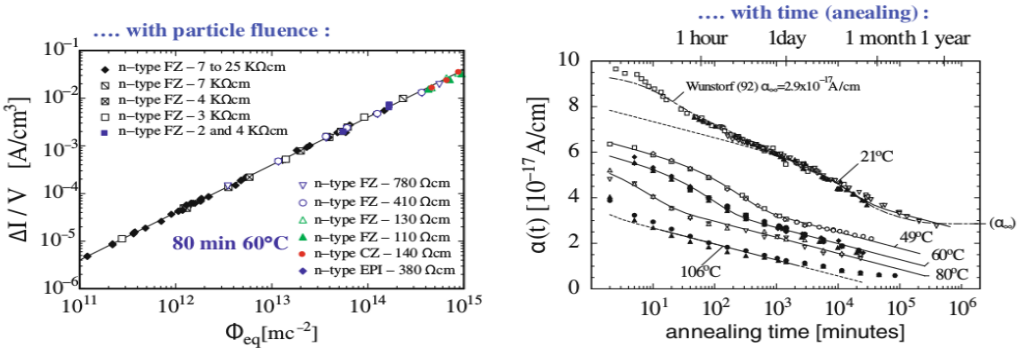

Figure 2.14: *Leakage current vs fluence and annealing time[11].*

Depletion Voltage

Depletion Voltage depends on the effective doping N_{eff}. In a n-type doped silicon bulk radiation constantly removes donors and at the same time increase acceptor like defects. Due to the fact that radiation dominantly creates acceptor like defects and only to a smaller extent donors, the silicon becomes increasingly p-doped. The dependence of the effective doping concentration Neff and the full depletion voltage on the radiation fluence is shown in Figure 2.15 on the right. The behavior can be parametrize as:

$$N_{eff} = N_{D,0} e^{-c_D \Phi_{eq}} - N_{A,0} e^{-c_A \Phi_{eq}} - b\Phi_{eq} \tag{2.18}$$

with $N_{D,0}$ and $N_{A,0}$ being the initial donor and acceptor concentrations, c_A and c_D the acceptor and donor removal rates, $b\Phi_{eq}$ the acceptor creation term.

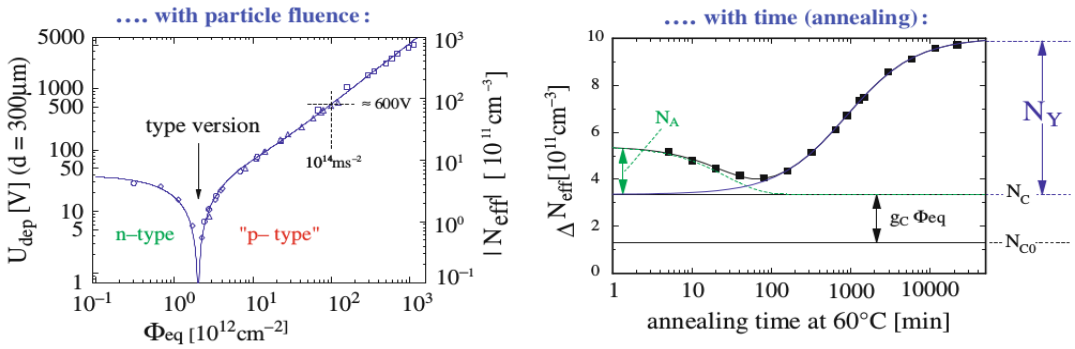

Figure 2.15: *Depletion Voltage vs fluence and annealing time [11].*

In addition, N_{eff} is subject to a temperature dependent diffusion with time this is shown in Figure 2.15 on the right and is parametrized as:

$$\Delta N_{eff}(\Phi_{eq}, t, T) = N_{c,0}(\Phi_{eq}) + N_A(\Phi_{eq}, t, T) + N_Y(\Phi_{eq}, t, T) \tag{2.19}$$

The above description is called the Hamburg model. The term $N_{c,0}$ depicts the donor removal and the acceptor creation rate. This depends strongly on oxygen concentration where oxygen can bind vacancies, which otherwise combine with phosphorus [11]. Oxygen rich sensors have been proved, from experiments, to be more radiation tolerant. The term $N_{A,0}$ is a beneficial factor and is can be seen in 2.15 it reduces the $\Delta N_{eff]}$. The introduced acceptors decay and inverted sensors with negative charge become less negative while sensors that are not type inverted with positive space charge region become more positive (acceptors are introducing negative, donors are introducing positive space charge). In the LHC experiments the beneficial annealing can be used in maintenance periods to heal short range defects. The term N_Y is the reversed one. After long annealing times acceptor like defects have developed by a secondary processes. This term needs to be suppressed by freezing-out at subzero temperatures.

In n-type detectors after type inversion the pn-junction is moved to the backside formed by the n+ backside implantation and the now p-bulk. As long as a bias voltage can be applied as required by the increasing depletion voltage and the sensor remains fully depleted it remains also essentially functioning. However, due to a longtime effect called reverse annealing, the effective doping concentration continues to increase even after irradiation. The consequence for the experiments is, that once the sensors have been irradiated they have to remain at low temperature even in periods where the experiment is not operated to prevent this effect from progressing.

Charge Trapping

Damage by irradiation creates trapping centers inside the silicon: the concentration of these new trapping centers N_i can be approximated by the relation:

$$N_i = g_i \Phi_{eq} f_i(t) \Rightarrow \frac{1}{\tau_{eff}} = \gamma \Phi_{eq} \tag{2.20}$$

where the product g_i is the introduction rate and $f_i(t)$ describes the evolution of annealing with time. Charge that would normally contribute to the signal of the detector is trapped in these levels

for a time. exceeding the integration time of the readout system. The degradation of the collection efficiency can be parametrized by an exponential decay, depending on the trapping time τ_{eff} , which is different for electrons and holes due to their different mobility. The degradation of charge can be described by:

$$Q_{e,h}(t) = Q_0 exp(-\frac{1}{\tau_{eff}}t) \tag{2.21}$$

In Figure 2.16 on the left the dependence of the reverse annealing time with the particle flux is depicted which is different for electrons holes due to the deferent mobilities. On the right of Figure 2.16 the annealing of the trapping time is depicted and as it can be seen the inverse trapping time decrease for electrons while increase for holes.

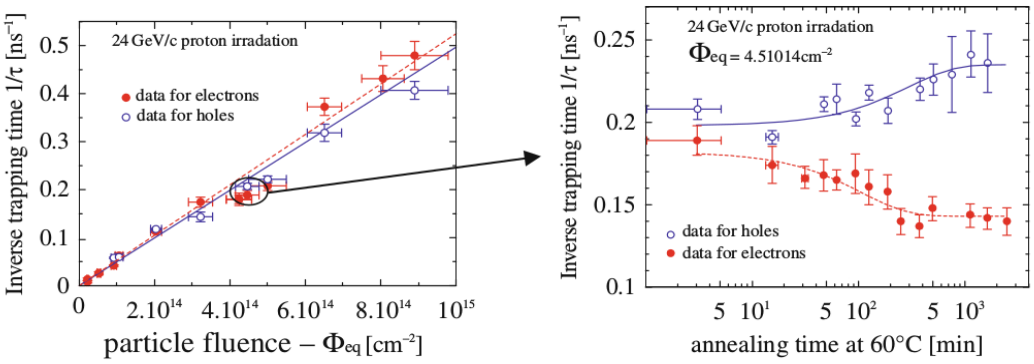

Figure 2.16: *Inverse trapping time vs fluence and annealing time [11].*

Leakage current, charge collection efficiency and depletion voltage evolve with the radiation as [11]:

- leakage current always decreases.
- charge collection efficiency decreases for holes and increases for electrons.
- acceptor levels decay in the beneficial annealing phase and increase later with reverse annealing.

The new sensors that are currently under testing for the Phase-II upgrade of the CMS Tracker are planned to be n-on-p sensors while the Tracker until now has p-on-n sensors. Charge collection by electrons using $n+$ strips provides equivelent or higher signals after irradiation than achieved for p-in-n sensors.

Surface Damage

Surface damage is caused from radiation-induced effects on the silicon dioxide layer and the interface between the bulk and the oxide.

Since SiO_2 is an insulator, the creation of electron-hole pairs is not fully reversible, which leads to polarization effects and to the accumulation of static positive charges at the interface ,

which in turn can accumulate charge carriers from the bulk and thus decrease inter -strip resistance and increase inter -strip capacitance. The increase of inter-strip capacitance increase the noise and the decrease of the inter-strip resistance increasing the cross talk [11].

The introduced charge concentration increasing the Flat-band Voltage Measuring flat-band Voltage is a diagnostic tool for measuring the surface damage.

Chapter 3

The LHC and CMS experiment

3.1 The Standard Model

Over the past decades the Standard Model (SM) of Elementary Particle Physics has been proven a powerful and reliable theory. It relies on gauge invariance and symmetries and has allowed physicists to make precise predictions of new particles that have been confirmed experimentally with high accuracy.

The Standard Model consists of fermions (with spin $1/2$), gauge bosons (with spin 1) and the Higgs boson (with spin 0). Fermions can be divided into subgroups the Leptons and the Quarks. Every subgroup has 3 generations of particles which differ in mass. Ordinary matter is entirely made up from the first generation fermions. The heavier families are unstable and decay into the lightest one. Each fermion has a corresponding anti-particle with opposite charge [30].

The interaction forces differ between leptons and quarks. Leptons interact via the weak force and if charged via the electromagnetic force,while the quarks interact with the strong force and cannot exist separated as free quarks but are confined in hadrons.

Quarks can have different configurations dividing the hadrons into baryons and mesons. Baryons are made by three quarks while mesons are composed of a quark and an anti-quark pair.

The gauge bosons are associated to the three forces (electromagnetic, strong and weak) which are responsible for particle interactions. The photon is the exchange-particle of electromagnetic force, the W and Z bosons are the ones for weak force and the gluons transmit the strong force.

There has been no experimental contradiction of the Standard Model and it is able to describe three out of four of nature's fundamental forces. Electromagnetic force, which can be unified with the weak force to form the electroweak model, and the nuclear force, which is described by quantum Chromodynamics. The unification of the electroweak- and strong force is predicted at a higher energy range than is accessible today.

However, the Standard Model cannot explain other evidences of physics problems (often called New Physics) such as: the existence of Dark Matter, the matter-antimatter asymmetry in our Universe and neutrino masses and oscillations. New Physics theories predict the existence of new particles that would have played a key role in the high-energy phase of the early Universe. All these evidences of New physics give several reasons to believe that the Standard Model is only the low energy limit of a more fundamental theory.

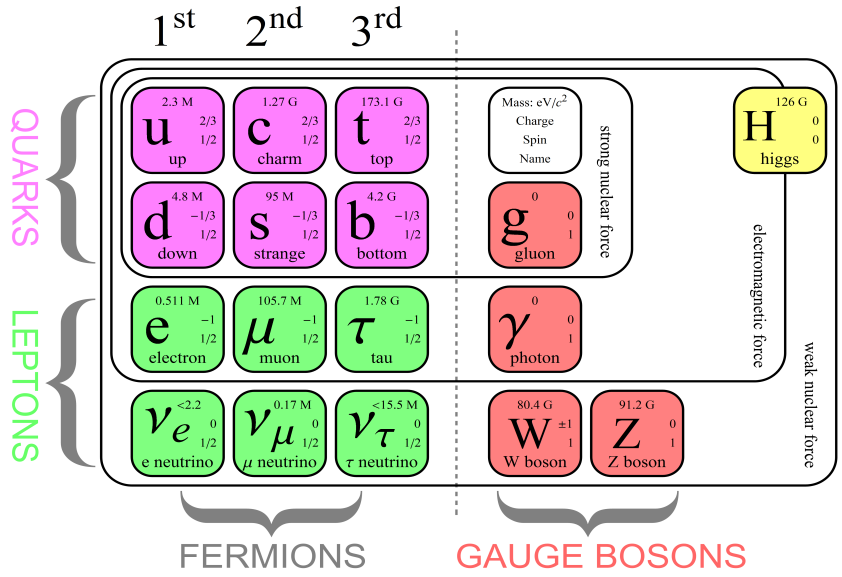

Figure 3.1: *The fundamental particles of Standard Model. Each generation consists of a lepton with charge 1 (electron,muon,tau) and its corresponding neutrino with charge 0 and also two quarks with charges $+2/3$ and $-1/3$ called up and down (first generation), strange and charm (second generation) and bottom and top (third generation) [31]*

The quanta of the weak interaction, the $W\pm$ and $Z0$ bosons, should be massless and the range of the weak interaction should be infinite, but their mass has been measured at precisely $80.4\,GeV/c^2$ and $91.2\,GeV/c^2$ respectively, which yields a very short range. This contradicts the symmetry underlying the electroweak interaction. To resolve this discrepancy the Brout -Englert -Higgs formalism has been introduced, which explains the particles' mass by their coupling to a scalar field -the Higgs field -and spontaneous symmetry breaking. As each field requires an exchange quantum an additional particle, the Higgs boson, must exist.

The predicted mass of the Higgs boson was very large , thus very large accelerators was needed in order to reach this large quantities of energies and produce this particles. The Large Hadron Collider (LHC) that was built at CERN in Geneva was designed in order to produce these particles It is the collider with the highest center -of -mass energy in the world and has already produced a very promising results such as the discovery of the Higgs boson with a mass of ~ 125 GeV/c^2 .

3.2 Physics motivation for upgrade

The LHC is designed to provide a maximum luminosity of $1 \times 10^{34}\ cm^{-2}s^{-1}$ and a maximum integrated luminosity of $40 fb^{-1}$ that leads to 1 billion proton-proton interactions per second. In the first physics run at 2011 and 2012 the collider reached a peak luminosity of 7.7×10^{33} $cm^{-2}s^{-1}$ more than 75% of its maximum luminosity and delivered an integrated luminosity of $25\ fb^{-1}$ per year to each of the two general purpose detectors, the ATLAS and CMS and less to the other two detectors ALICE and LHCb. The vast amount of data collected from the first run led to a lot of physics results. In 2012 the primary goal of the LHC was achieved with the observation of a new particle with a mass of $125\ GeV$. The particle was identified to be as the Standard Model Higgs Boson. In addition the decays of the new boson to the gauge boson of the Standard Model W,Z and photon were studied in detail.

The main motivation for a luminosity upgrade is to deliver more statistics to improve physics studies beyond those possible at LHC. To benefit, it is essential that detector performance remains similar to that at LHC, while higher luminosity implies higher particle fluxes and radiation damage. The physics potential after the upgrade could be divided into four main topics [32],[33]:

- Improvements of accuracy in the determination of Standard Model parameters.
- Search for signatures of physics beyond the Standard Model. Determination of parameters of New Physics.
- Extension of the discovery reach in high mass region. (e.g. quark composites, new heavy gauge bosons, multi -TeV squarks and gluinos, Extra -dimensions)
- Extension in the sensitivity of rare processes.

3.3 The Large Hadron Collider (LHC)

The Large Hadron Collider 3.2 at CERN located in Geneva is a circular accelerator with a circumference of 27 km, between 50 and 175 m underground, previously contracted for the large electron positron collider (LEP) [34].

It is designed to provide proton-proton collisions with maximum luminosity $10^{34}\ cm^{-2}s^{-1}$ and a center of mass energy of 14 TeV for the study of rare events such as the production of Higgs particle. It is the largest and highest energy particle accelerator, designed to collide counter beams of protons at four interaction points at a foreseen energy of 7 TeV per beam, or heavy ions at 2.75 TeV per nucleon.

The counter beams travel in separated beam pipes at a speed close to the speed of light. They are guided around the accelerator ring by a strong magnetic field, supplied by using superconducting electromagnets that are cooled down to about -271.3^oC . In 2012 the LHC has run at proton beams of 4 TeV and delivered an integrated luminosity of about 23.3 fb^{-1} .

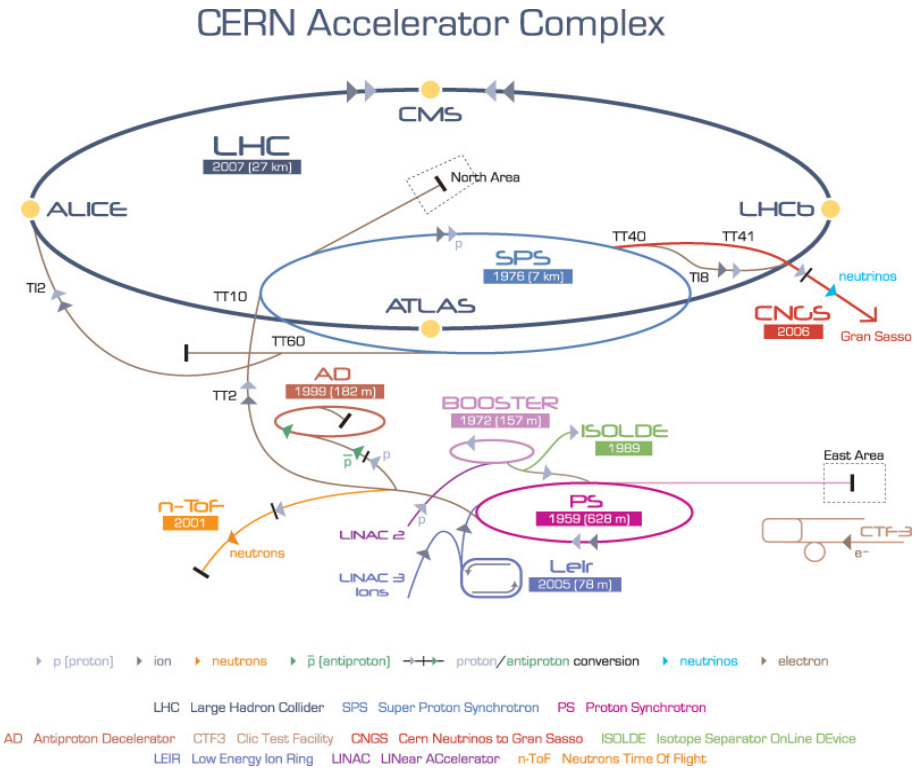

Figure 3.2: *Overview of the LHC experiments. The LHC houses two multipurpose experiments ATLAS and CMS accompanied by two special experiments LHCb and ALICE. Protons are created from gaseous hydrogen in a proton source and are then accelerated to* 50 MeV *in a linear accelerator. Next they are passed to the Proton Synchrotron (PS) through the Proton Synchrotron Booster (PSB) where they reach a total energy of* 25 GeV*. Before the injection into the LHC is the Super Proton Synchrotron, which accelerates the particles to* 450 GeV*.[35]*

At each of the four interaction points at least one experiment is operating. There are two large experiments, ATLAS and CMS and two medium-sized specialized experiments ALICE and LHCb. The motivation to have two general propose detectors such as Atlas and CMS with similar characteristics is that the systematic errors could lead to false results if there was only one

detector.

The CERN accelerator complex is a succession of particle accelerators that can reach increasingly higher energies 3.2. Each accelerator boosts the speed of a beam of particles, before injecting it into the next one in the sequence. Protons are created from gaseous hydrogen. The orbiting electrons get stripped of the hydrogen atoms and the protons are accelerated in the LINAC2 to $50\ MeV$ before they reach the PS Booster. The Booster accelerates them to $1.4\ GeV$ and the following Proton Synchrotron (PS) to $25\ GeV$. The final per -accelerator Super Proton Synchrotron (SPS) accelerates to $450\ GeV$ before the bunch of protons reaches the LHC where it can reach its final energy of $7\ TeV$ after several minutes. The collisions take place at the four intersection points inside the four main experiments.

The number of events per second generated by beam -beam collisions for given process is given by 3.1 [34]:

$$N = L\sigma \tag{3.1}$$

where σ is the cross section of a given process (the probability that an event occurs.) and L is the Luminosity which depends on the beam parameters.

The luminosity is one of the most important parameters of an accelerator. It is a measurement of the number of collisions that can be produced in a detector per cm^2 and per $second$. The bigger is the value of L, the higher is the number of collisions. To calculate the number of collisions we need also to consider the cross section. For the study of rare events the luminosity must be as high as possible.

The designed luminosity ($10^{34}\ cm^{-2}s^{-1}$) means that in the LHC detectors might produce 10^{34} collisions per second and per cm^2. It is achieved by dividing the beam into $2,808$ bunches with 115 billion protons in each bunch and a collision rate of $40\ MHz$. The luminosity for a Gaussian beam profile can be written as 3.2 [34]:

$$L = \frac{N_b^2 n f_t \gamma}{4\pi\varepsilon_n \beta^8} \tag{3.2}$$

with N_b the number of particles per bunch, n the number of bunches per beam, f_t the bunch crossing frequency of a bunch, ɣ the relativistic factor, ε_n the normalized transverse emittance of the beam (the average spread of particle coordinates in position-and-momentum phase space, keeping the emittance small means that the likelihood of particle interactions will be greater resulting in higher luminosity.), and β^* the beta function at the collision point (Beta is roughly the width of the beam squared divided by the emittance. If Beta is low, the beam is narrower, " squeezed ". If Beta is high, the beam is wide and straight.).

The integral of the delivered luminosity over time is called integrated luminosity. It is a measurement of the collected data size, and it is an important value to characterize the performance of an accelerator.

$$I = \int L dt \tag{3.3}$$

It is expressed in inverse of cross section (i.e. $femtobarn^{-1}$).

3.3.1 The LHC upgrade

CERN began planning to increase the luminosity of the LHC above the original design even before the machine went into operation. This will undergo a period of machine maintenance (long shutdown, referred to LS1, LS2, LS3), during which all the detectors will adjust their performance to cope the new machine conditions. The periods of data-taking (referred to as Run-II, Run-III, Run-IV). This twenty year period of upgrading the LHC can be divided roughly into two equal parts. The outcome of both will lead to the high luminosity LHC (HL-LHC). This will be done in two steps during the Longterm Shutdown LS2 (often called Phase 1) and LS3 (often called Phase 2).

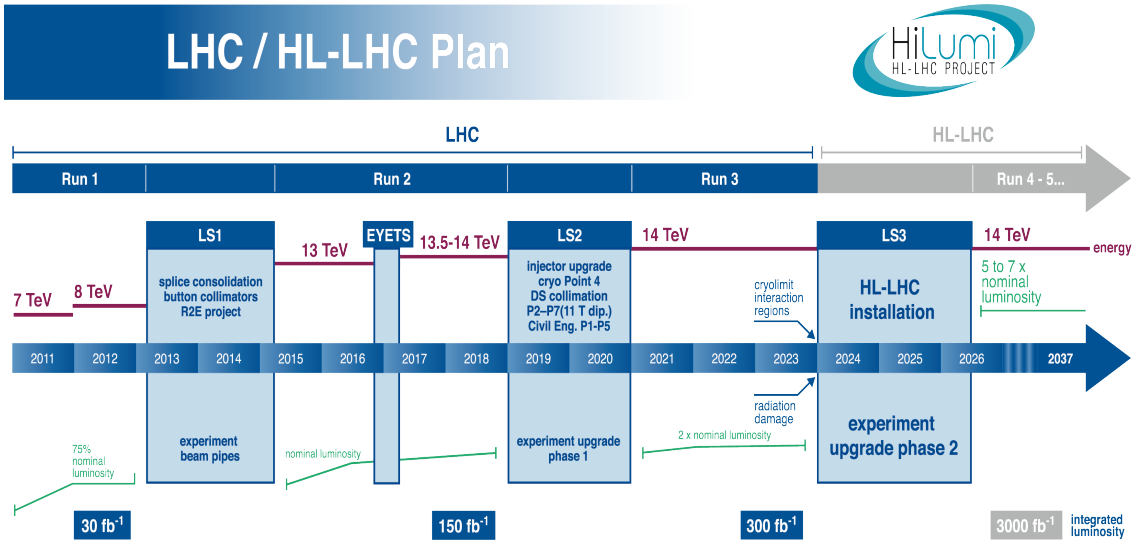

Figure 3.3: *HL-LHC upgrade schedule [36].*

- *Phase* -I: This period started at 2010 and will undergo until 2020. The LHC will achieve its designed (nominal) luminosity at Run II which started at 2015 and will undergo until the end of 2018. Towards the end of the Phase the LHC should reach double the designed luminosity $2 \times 10^{34}\ cm^{-2}s^{-1}$, providing an integrated luminosity of over 300 fb^{-1} . The upgrades of the machine will be done with two major shutdowns of longer than a year, $LS1$ which was accomplished between the years 2013 -2014 and $LS2$ which will be accomplished between the years 2019 -2020 . In this upgrade period there will not be major upgrade changes [37]

- *Phase-II*: After 2019 -2020 the increase in statistics will become negligible if the accelerator is still operated at its design luminosity value. For example a reduction of the statistical error by a factor of 0.5 would require more than 10 years of further operation. Thus there will be major upgrades of the LHC machine with an extended shutdown in order to achieve much greater integrated luminosity to the two general purpose experiments Atlas and CMS,such as 13 T superconducting focusing magnets. By 2023 there will be another long shutdown, LS3, that will further improve the LHC machine performance, producing a

significant increase in the LHC luminosity. The instantaneous luminosity will be increased up to peak value of $5 \times 10^{35}\ cm^{-2}s{-}1$, and will deliver 250 fb^{-1} per year and has the scope of reaching the threshold of 3000 fb^{-1} in 10 -12 years of further operation, this implies to major challenges in terms of radiation tolerance,for both sensors and readout - detector electronics as they will have to cope with a pileup 3 of up to 100 events per bunch crossing (as compared to 19 for nominal LHC parameters) [37].

3.4 The Compact Muon Solenoid (CMS)

The Compact Muon Solenoid (CMS) 3.4,is a large multi -purpose experiment located at the northernmost beam crossing point of the LHC, designed with an hermetic 4π layout. Different layers of detectors measure different particles, and use this data to build up a picture of events at the heart of the collision. Each layer has special properties to track, stop or measure the particles generated by the collisions.

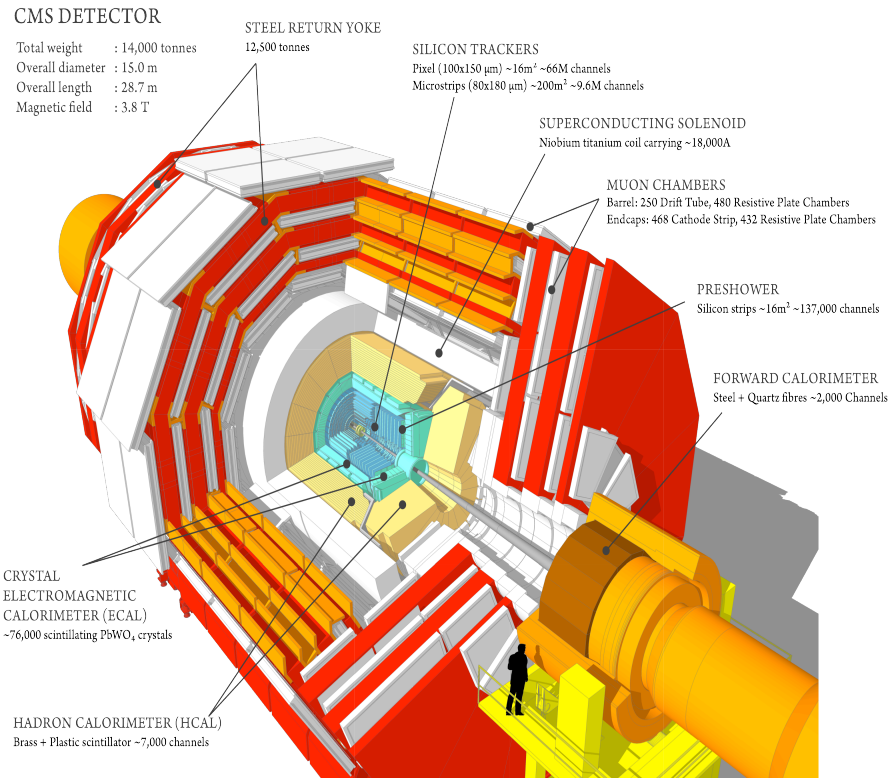

Figure 3.4: *3D -schematic of the CMS detector that shows its different parts (sub -detectors) of CMS. The LHC beams collide at the center of the CMS cylinder. The products of the collision are detected from the different parts of the detector. Every layer in the detector has a different purpose. [38]*

The CMS name originates to three key characteristics: compactness, muon chambers and the superconducting solenoid. CMS experiment is bound to have a very precise muon detection system in order to identify muon jets caused by proton-proton interactions. This led to a design incorporating a strong superconducting magnet system enabling the muon chambers to be relatively small. CMS detector is 15 m in diameter, 21.6 m long. ATLAS experiment is 8 times bigger

in terms of volume but the total mass of CMS of 12500 tons is twice the mass of ATLAS.

The main features of CMS that distinguish it from other experiments are the high field super conducting solenoid, a full silicon inner tracker and a homogeneous electromagnetic calorimeter based on scintillating crystals without non-active absorbers.

The detector can be divided in three larger parts the Tracker , the calorimeters and the muon chambers 3.5.

- The most inner part is the Tracker, which is composed of a silicon pixel and strip detectors. The main goal is the recording of trajectories of charged particles. The strong magnetic field bent the trajectory of each track which indicate the particle momentum as well. The Tracker is surrounded by the electromagnetic and the hadronic calorimeter (ECAL and HCAL). Neutral hadrons, such as neutrons are traversing the tracker in a straight line, not exciting any signal.

- The Electromagnetic Calorimeter ECAL measures the energy of Light particles such photons and electrons which are interacting electromagnetically and are stopped in the ECAL. The HCAL detects particles made up of quarks. These inner parts are encircled by a superconducting solenoid inducing a homogeneous magnetic field strength of $4\,T$. This immense bending power is necessary to achieve the good momentum resolution for particles.

- Muons are the only charged particles that escape the calorimeters. Which are then detected by the muon chambers in the outermost layer.

Neutrinos cannot be detected anywhere in the detectors. The only way to get information about them is to sum up the energies and momenta of all other particles and attribute the missing fraction to the neutrinos.

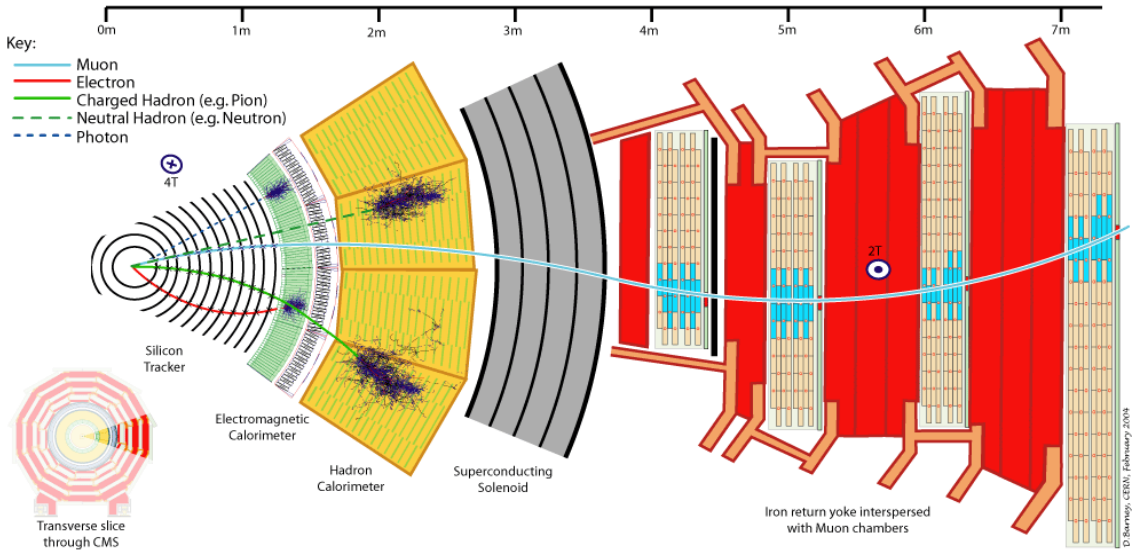

Figure 3.5: *Traverse picture of the CMS detector showing the different parts. [39]*

3.4.1 The CMS Tracker

The inner part of the CMS is the tracking system (Tracker) which is consisted totally from silicon detectors. Silicon detectors are placed in layers on concentric cylinders surrounding the interaction point and has a length of 5.8 m and a diameter of 2.5 m. It contains multiple layers of silicon detectors covering an area up to 206 m^2, which makes it the world largest silicon device [40].

It is designed to provide a precise and efficient measurement of the trajectories of charged particles emerging from the LHC collisions which allow a precise reconstruction of primary and secondary vertices while minimizing interaction. Therefore as little material as possible was used. The vertex of a particle is reconstructed and its creation point is determined. The reconstructed tracks have to be very precise and must be able to distinguish two very close spaced vertices.

The tracker is consisted of a two stage system, a small pixel device for the innermost layers close to the interaction point, surrounded by the silicon strip detector. The silicon strip detector is consisted of the inner barrel detector (TIB), the inner discs (TID), the outer barrel (TOB) and of the two end cap detector systems (TEC+ and TEC-). The over all length of the tracker is 5.4 m. A cross-section of one quadrant is shown in 3.7 and a full 2D schematic of the tracker can be shown in 3.6.

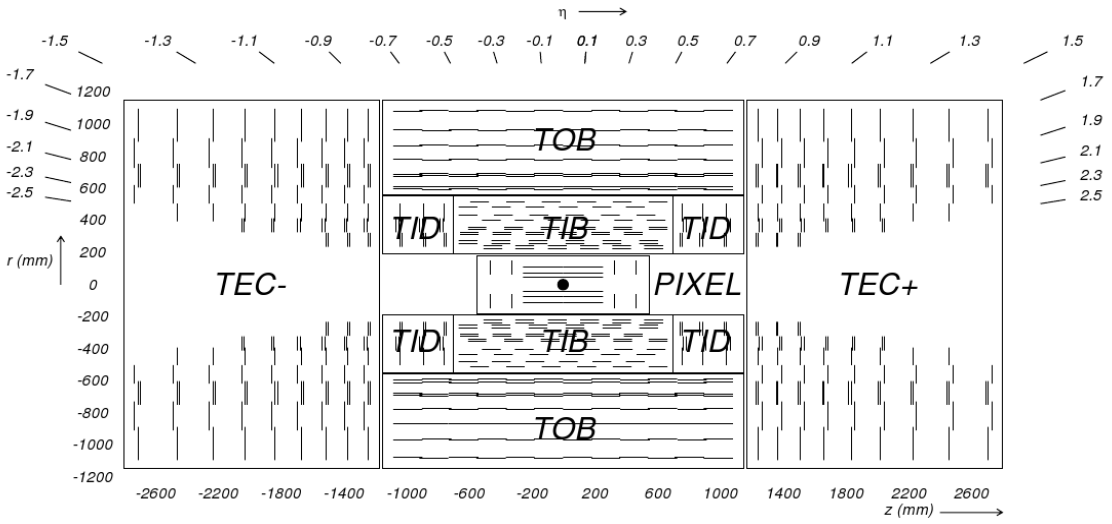

Figure 3.6: *Schematic of the Tracking system of CMS. It has different parts with a cylindrical shape. The innermost part of the Tracker is the Pixel detector (TPB) which circulates the interaction point. Outside the (TBP) there is the silicon strip detector which is divided to the inner silicon strip detector (TIB) with the inner discs (TID) and the Outer Strip detector (TOB) with the end cap detector systems (TEC+) and (TEC-). [41]*

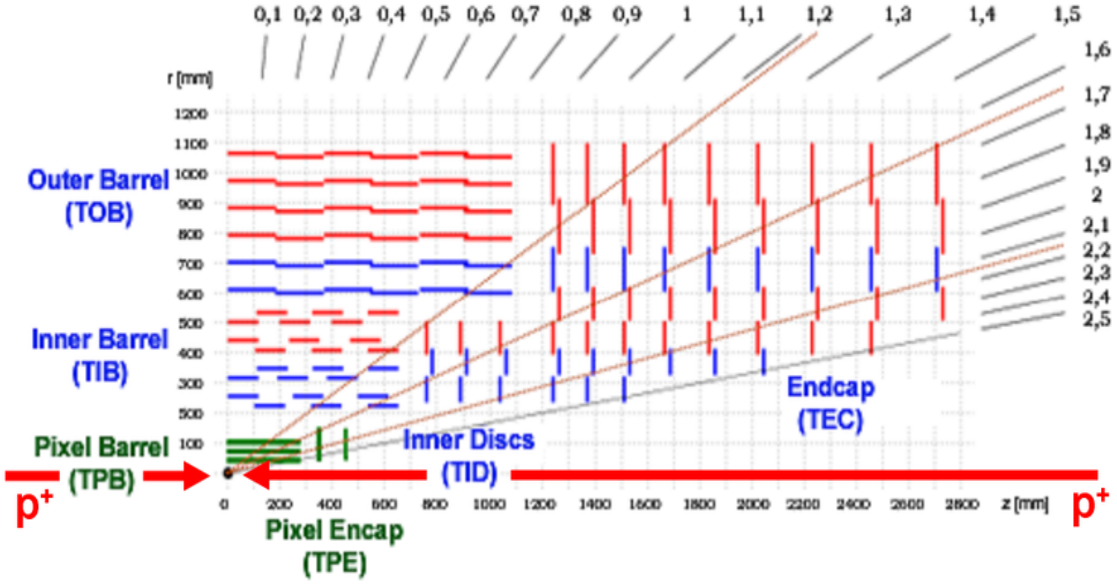

Figure 3.7: *Schematic of the one Quarter of the CMS Tracker in the r-z plane where* $r = \sqrt{x^2 + y^2}$*, while the axis above and right of the Figure is the pseudo-rapidity* (n)*. The green layers is the Pixel detector. The blue layers are the microstrip detectors with a double layer of sensor and the red layers are the micro -strip with a single sensor.[42]*

The Pixel Detector

The pixel detector 3.8 which is closest to the primary vertex, where the particle flux is highest has to meet extreme requirements in terms of radiation tolerance and rate capability. It is composed of three barrel layers with silicon pixel detectors at radii 4.4 cm and 7.3 cm and 10.2 cm and two end-cap discs at $z = \pm 34.5$ and $z = \pm 46.5$ cm resulting to a 3D coverage up to ($\mid n \mid < 2.5$). The main task of this detector is vertex finding and flavor tagging. An efficient tagging of particles like b -quark, c -quark and tau which requires tracking as close as possible to the interaction vertex. The need of very high spatial particle track density close to innermost tracking makes it necessary to be composed by pixel detectors which could provide fine granularity (the extent to which a material or system is composed of distinguishable pieces) in three dimensional space [43].

The overall length of the barrel is 53 cm and it has a total of 66 million readout channels (768 modules in the barrel plus 672 modules in the forward disks). The individual pixel cells are rectangular with a size of 100×150 μm^2 and thickness of about 270 and 285 μm. The pixel sensors are based on a n-in-n process which means that the signal is read out from n^+ doped electrodes in a high resistivity n type substrate. The electron readout from the n^+ doped electrodes result to a faster response due to the fast electron mobility. The back plane is covered with a p implant which has the advantage of allowing under-depletion operation due to type inversion caused by the increasing radiation damage. The pixel system requires a cooling system and operation at low Temperatures due to the intense radiation damage in the innermost parts of the Tracker.

The achieved spatial resolution of the CMS pixel Tracker is 10 μm in r-φ direction and 20 μm along the beam z -axis. Due to its high segmentation, the pixel detector is a very efficient

system for track reconstruction, primary vertex reconstruction, electron/photon identification, muon reconstruction, tau identification and b-tagging.

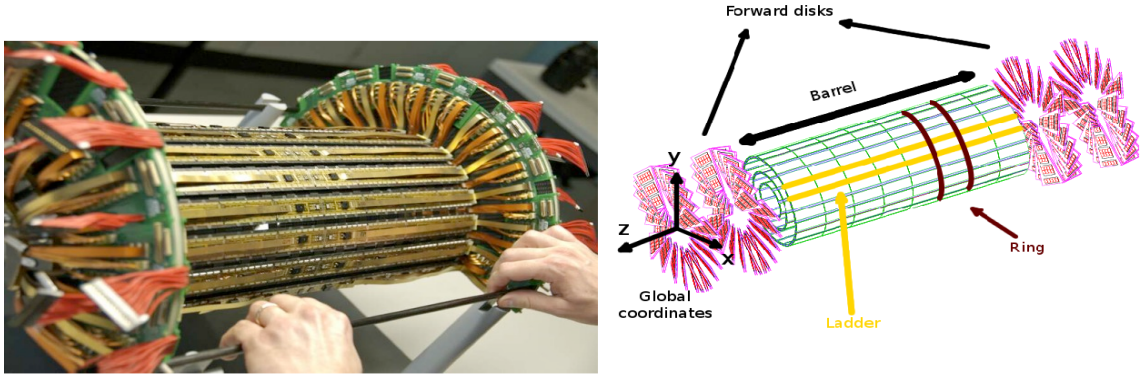

Figure 3.8: *The structure of the CMS Pixel Detector [44]*

The Silicon Strip Tracker

In the outer regions of the Tracker of CMS, where the particle rate is considerably lower than in the pixel region and extreme granularity is not required, silicon -micro strip detectors are used. The Pixel detector being subjected to fluencies up to $\Phi_{eq} = 3 \cdot 10^{14}\ n_1 MeV/cm^2$ per year at nominal LHC luminosity while the strip detector is facing only $\Phi_{eq} = 1 \cdot 10^{14}\ n_1 MeV/cm^2$ for the full 10 years of operation. As mentioned in the bigging of this section the Silicon strip detector can be divided in four parts 3.7. The modules are placed in layers with radii between $20 < r < 110\ cm$.

The inner tracker (TIB) 3.9 ($20cm < r < 55cm$) consists of 4 layers made of 320 μm thickness and strip pitch (strip width + strip separation) between 80 and 120 μm. The pitch decrease for sensors that are being placed away from the interaction point. This is done in order to provide better precision in the regions close to the calorimeter. The two innermost layers of TIB are made up of modules where two single sided sensors are mounted back -to -back (blue layers in Figure 3.7). The back sensor is placed in a way that its strips form a small angle with the front sensor at a stereo angle of 100 $mrad$. Modules with double sensors very close to each other with subtend strips in an angle provide position resolution in two dimensions since the transverse particle will be projected in two strips. The stereo angle should be small in order to avoid coincident signals ("ghost hits"). The other two outer layers (red layers in Figure 3.7) are composed of modules with single strips.

The end-cap of the inner tracker (TID) has 3 layers filling the gap between TIB and TEC and again as the barrel it has silicon strip detectors of 320 μm thickness with the strips pointing toward the beam. Again Double sensor modules placed closer to the interaction point.

In the TOB region ($55 < r < 110\ cm$) the particle flux is lower, therefore the granularity can be decreased even further, which means that the strip pitches are wider and the individual strips longer. In order to maintain the level of signal -to -noise ratio, 500 micrometer -thick silicon sensors are used. The TOB consists of six layers with strip pitches between 120 and 180 μm and the two innermost layers again feature a stereo angle [45].

The End -caps of the outer tracker (TEC) has nine discs with $500\ \mu m$ thick sensors. The number of rings for the TID is three and seven for the TEC and they are arranged in a way that they cover the maximum surface with the fewest gaps

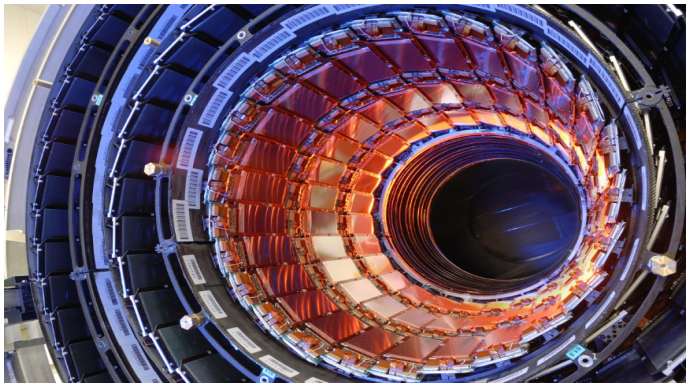

Figure 3.9: *Tracker Inner Barrel[46]*

All regions of the Silicon strip Tracker use AC coupled, ploy -silicon biased, p-on-n devices processed on $6^{"}$ wafers. This means that the readout electrodes are highly -doped $p+$ implants in a high -resistivity n -doped substrate. This is a simple and low -cost process well known in the semiconductor industry and it has been proven to be sufficiently radiation-hard for the expected flux over the nominal tracker lifetime. All sensors in the barrel are rectangular while in the End -caps are trapezoidal [45].

One thing that should be taken into account for the p -on -n silicon strip sensors is the type inversion that is caused by radiation damage with increasing flux. The effective dopping of the substrate changes from n -to p -type which cause the depletion region to start growing from the back which make the under depleted operation impossible.

In the Outer Silicon strip Tracker two sensors are wired together to one readout hybrid (daisy chained) while in the Inner each sensor has one readout. This increase the capacitance load for the Outer Tracker modules and thus the noise but it is compensated by the increased thickness.

The cooling system is common for the whole strip tracker and consists of a closed circuit system with C_6F_{14} as coolant. The thermal contact between the module frames and the piping is established by the screws that hold the modules in place on their respective support structures. The nominal coolant temperature is -15^oC, which translates to about -5^oC on the silicon sensors. [45]

3.4.2 Requirements for a new Tracker

The CMS experiment has developed a major plan for the upgrade of its tracking system in order to cope with the same accuracy to the increased fluxes of several thousands of charged particles, emerging from the collisions.

The traverse particle density within the tracker will increase significantly by going to higher luminosities. Figure 3.10α' , shows the expected absorbed dose that is distributed over the whole CMS detector for an integrated luminosity of 3000 fb^{-1} and 3.10β' shows the expected flux expressed in terms of 1 MeV neutron equivalent fluence. The expected performance will eventually

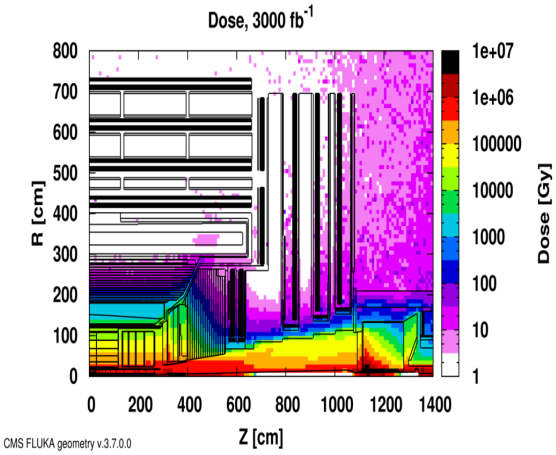

(α′) *Absorbed dose in the CMS cavern after an integrated luminosity of 3000* fb^{-1} *. R is the transverse distance from the beam -line and Z is the distance along the beam -line from the Interaction Point at* $Z = 0$.*[47]*

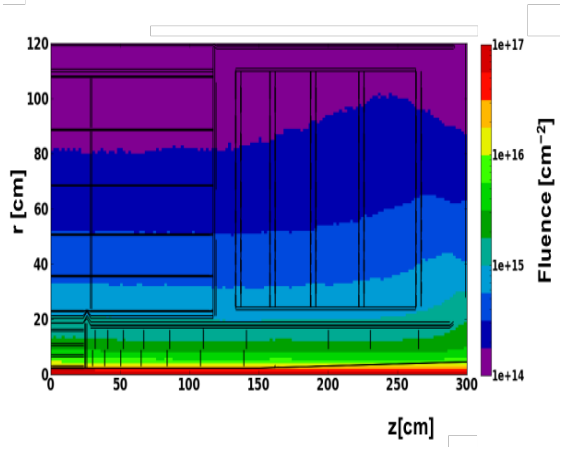

(β′) *Map of the expected particle fluence in the Tracker volume corresponding to an integrated luminosity of 3000* $fb^{-1/}$ *, expressed in terms of 1 MeV neutron equivalent fluence. The expected fluence has a strong dependence on radius, while it is almost independent of the z coordinate. [47]*

be degraded by the radiation damage. Greater radiation tolerance will be required, especially for sensors.

The luminosity increases at the LHC result in higher pileup. Pileup produces many more hits in the tracking detectors, leading to mis -measured or misidentified tracks. The detector, and the silicon detectors, will have to cope with more tracks, close to each other which it could result to one or more hits to one strip. These hits can not be separated and are detected as only one hit.

The track reconstruction will lose efficiency as not all tracks will be resolved. In Figure 3.11 the track finding efficiency within $|\eta| < 2.4$, for $p_T = 10\ GeV$ muons decreases from 100% for the strip tracker without aging at 50 PU to 75–95% after $1000\ fb^{-1}$ at 140 PU. The efficiency for tracks from tt^{-}events with $p_T > 0.9\ GeV$ drops from above 85 – 95% to $50 - 80\%$, while the single track fake rate increases from less than 5% to 12 – 45%.

For all these reasons the tracker should be replaced entirely with new detectors, module, read-out electronics and layout.

The requirements that the detector needs to meet can be summarized as [47]:

- *Radiation Tolerance:* The upgraded Tracker must be able to operate efficiently in the harsh environment of the integrated luminosity of $3000\ fb^{-1}$. The Outer Tracker must fulfill these requirements without any intervention for the full years of operation after the upgrade, while the Pixel detector is designed with the possibility to be extracted easily giving the possibility to replace the inefficient modules.

  Irradiated sensors loose signal, and also produce high leakage currents which is a source of noise. As the impact of radiation to the sensor performance is crucial, an upgraded tracker needs more radiation hard sensors.

- *Increased Granularity:* The increased particle flux inside the Tracker will increase the occupancy of each detector causing the track finding efficiency to decrease dramatically. In

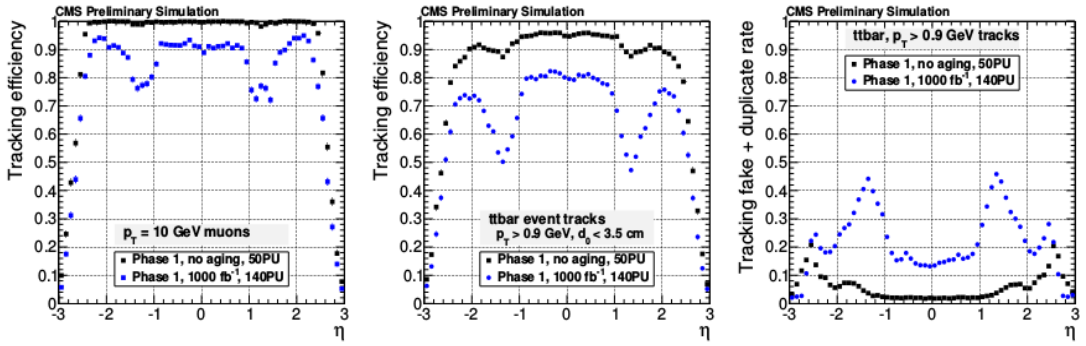

Figure 3.11: *Left: efficiency for $p_T = 10\ GeV$ muons as a function of pseudorapidity for the Phase-I detector before and after the Outer Tracker has been aged by an equivalent of $1000\ fb^{-1}$. Center: same plot for charged particles from $t\bar{t}$ events for which the particles have $p_T > 0.9\ GeV$ and are produced within $3.5\ cm$ of the interaction region (in the transverse direction). Right: fake rate, the fraction of reconstructed tracks that are not matched to a simulated charged particle, for the same selection of particles in tt^- events [47]*

order to ensure efficient tracking a higher channel density will be required. This can be translated to increased number of detectors with increased segmentation to each sensor. In order to provide more strips and more pixels per surface inside the Tracker.

- *Reduced material:* The volume and the material density of each detector (read -out electronics, sensors) and the overall construction of the Tracker should be reduced as much as possible. The CMS will be greatly benefit from a lighter tracker which will improve the event reconstruction as well as the performance of the calorimeter, due to the fact that the particles will lose less energy through their path inside the Tracker.

- *Modules that contribute to Level-1 Trigger* CMS detects hundreds of millions of collisions each second, only a handful of which are useful for physics studies. The job of the CMS Trigger is to select only the few hundred useful events while discarding the rest. The first level of the two -stage trigger, known as the Level-1 (or L1) Trigger, selects a maximum of a hundred thousand events each second for more detailed selection by the second level, known as the High-Level Trigger more details can be found at [48] [49].

  As not all data can be transferred and recorded, the data reduction on the detector level is necessary. The trigger rate of the Level -1 trigger has to stay below $100\ kHz$, to ensure the higher level trigger to keep the final output rate of about $100\ Hz$ for storage and analysis. As the charged particle transverse momentum spectrum, mainly consists of low p_T tracks that are not interesting, cutting p_T tracks below a certain threshold away would substantially reduce the number of tracks and thus the trigger rate, helping to keep it below $100\ kHz$. The possibility of including real-time track-based information in the Level -1 trigger decision, allowing for immediate identification of high p_T tracks and thus greatly reducing the amount of data that has to be processed .

- *Improved Pattern Recognition:* The upgraded Tracker should allow quick and effective track reconstruction. Each signal from different detectors modules should be efficiently and

quickly find the tracks of each traversing particle.

- *Improved two* -track seperation: In order to have good statistics in the High Luminosity era the separation between two closely spaced tracks should be improved. This can be achieved by shortening and increasing the number of strips. This will make possible to detect two different tracks on two strips, instead of two hits on one long strips resulting in only one hit.

- *Extended acceptance:* A new layout of the Tracker will be needed that would give better acceptance especially at the End -caps in order to cover as much as possible the whole 4π stereo angle.

3.5 The CMS Tracker Upgrade

The upgrade of the CMS Tracker will be done in several stages following the upgrade schedule of the LHC 3.3 with the two main phases (I and II). Between LS1 and LS2, during the extended Technical stop (2016-17), the pixel detector is replaced with the "Phase-I" upgrade.

Following LS3 (2023-2025) the high luminosity program with the upgraded LHC is referred to as High- Luminosity LHC (HL-LHC) or "Phase-II". The schedule of the Phase-II upgrade can be summarized in 3.12. The pixel detector will be replaced again entirely, while there will be major upgrades on the Outer Tracker.

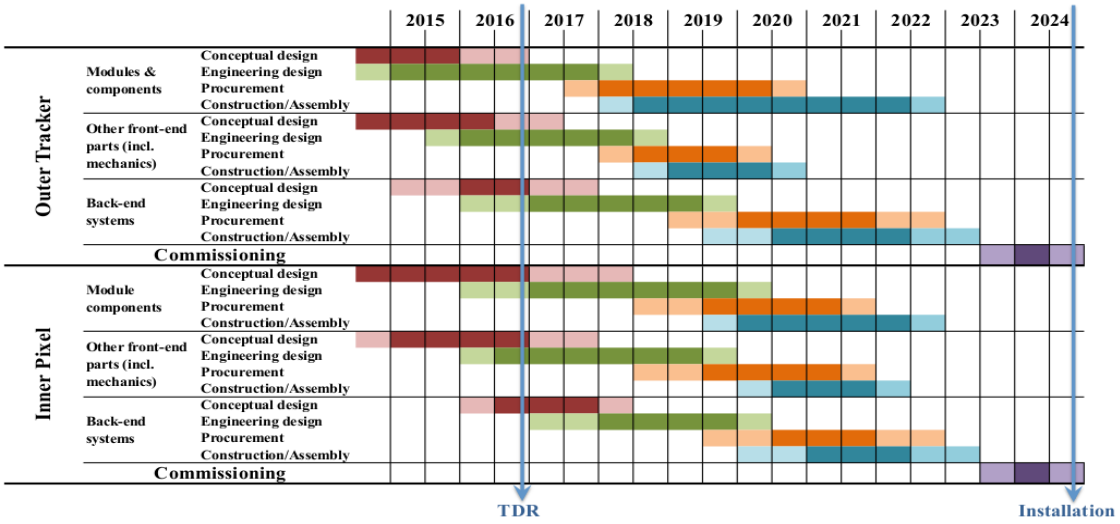

Figure 3.12: *Phase II Upgrade Schedule for the CMS Tracker [47].*

3.5.1 Phase- I Upgrades

Phase I of the CMS upgrade focuses on making the detector ready for the increased peak luminosity which is provided by the LHC after LS2 following the sLHC -PP project and prepare it for Phase II. In this phase there are not any changes concerning the Outer Tracker, while the pixel detector has been upgraded for the first time but with no significant changes in the pixel sensors. The Upgrade has already been performed in the winter of 2016/2017.

The baseline was to replace the Pixel tracker with a new ultra -lightweight construction support with less material for minimizing the impact parameter on data taking. A new cooling system with CO_2 as coolant than the C_6F_{14} used before allow smaller exchanger and pipes.

There is a 4 -layer barrel and 3 disk End -caps, with the forth extra barrel being placed at a radii of 16.0 cm and the third extra end -cap being placed at positions $\pm 51.6\ cm$ from the interaction point. This extends the Pixel Tracker coverage with four hit tracking up to $|n| < 2.5$ in contrast with the 3 hit coverage that was used so far because of the 3 barrel layers and 2 end-cap discs which was leading to $10 \div 15\%$ inefficients at $|n| < 1.5$ and larger inefficients at $1.5 < |n| < 2.5$.

The radii of the innermost layer is closer to the interaction point it is placed at a radii of 3.0 cm while the space between the layers has been increased.

The electronic boards and connections has been moved out of the tracking volume for material reduction. A new readout chip with reduced data loss at higher collision rates, high bandwidth readout electronics and links as well as DC-DC power converters also have been developed.

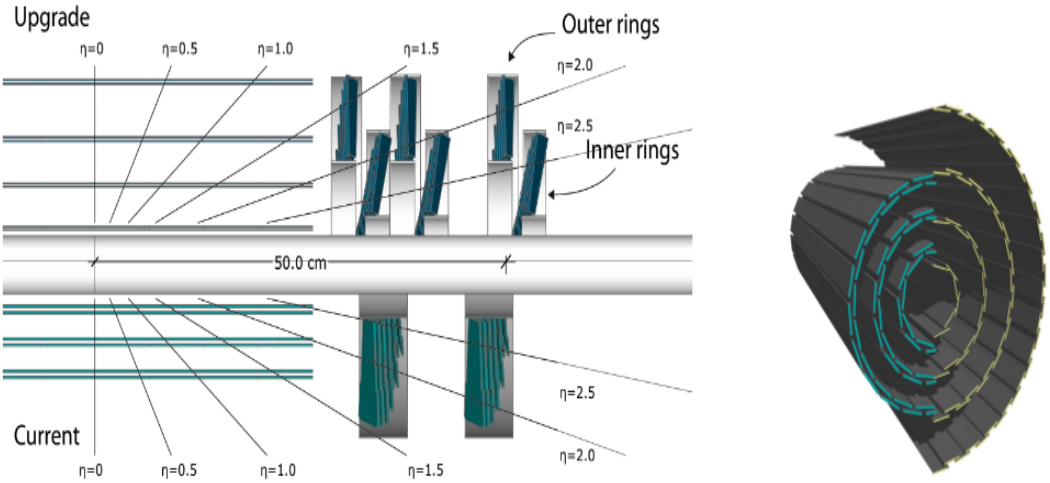

Figure 3.13: *Conceptual layout comparing the different layers and disks in the current and upgrade pixel detectors. The disks are placed in order to maximize the 4 -hit η coverage 4 layers will be placed instead of 3 with a larger space between them and the first layer closer to the surface. The Pixels discs are three instead of 2 which will provide better resolution in* $|n| > 2.5$ *Right: Transverse view comparing the pixel barrel layers in the two detectors. [47].*

3.5.2 Phase -II Upgrades

The Phase -II upgrade involves the replacement of the whole Tracker. In Figure 3.14 there can be seen the new Tracker layout in the form that it will take after the two upgrades.

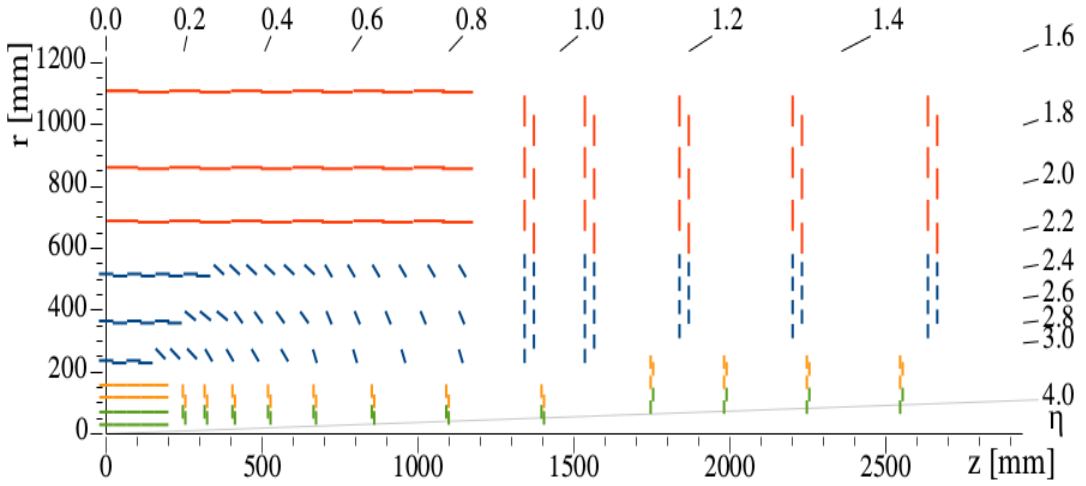

Figure 3.14: *Sketch of one quarter of the tracker layout in r -z view. In the Inner Tracker the green lines correspond to pixel modules made of two readout chips and the yellow lines to pixel modules with four readout chips. In the Outer tracker the blue lines correspond to PS modules, while red lines correspond to 2S modules. [50]*

In the inner Pixel detector green (yellow) layers in Figure 3.14 the detector will have 4 barrels with 8 small double-disks and 4 larger discs per side. Each double-disc is physically made of two layers, which facilitates to mount modules onto four planes. The extended Pixel detector will have a surface of approximately $4\ m^2$ compared to $2.7\ m^2$ in the Phase-I. The acceptance extends to $|\eta| \approx 4$. The design of the Inner Tracker will allow to replace degraded parts over an extended year-end technical stop, which requires the possibility to extract and insert the detector without removing the CMS beam pipe. [50].

The pixel sensors that are considered for the Phase -II of the upgrade will be processed with the n -in -n planar technology that it will be adopted from Phase -I. The pixel aspect ratio that has be taken into account is $25 \times 100\ \mu m^2$ and $50 \times 50\ \mu m^2$. The sensors have to be radiation hard up to $2.3 \times 1016 neq/cm^2$. Thin sensors are preferred over thick ones since the advantage of a larger signal in thicker sensors disappears with the increased number od traps that will be present at large fluencies Thinner sensors need smaller operational voltages and produce less leakage current. The active thickness of the planar pixel sensors will be in the range $100–150\ \mu m$. Oxygen -rich float zone silicon, or the deep -diffused variant studied by CMS, are good candidates for the pixel sensors while magnetic Czochralski is a viable alternative, at higher costs. Also an alternative option that is under consideration is the possibility to use 3D silicon sensors. 3D sensors have higher radiation resistance because of the shorter charge collection distance. The production process is more expensive and thus not suitable for large volumes, the use of 3D sensors could be limited to the regions of highest particle fluencies

The Outer Tracker will require major changes in these phase of the upgrade. As mentioned earlier it will require higher granularity and radiation tolerance. The vast amount of data with

combination of bandwidth limitations makes the selection of interesting physics events from the Level -1 trigger very challenging. To overcome this issue, the modules for the Phase II will require a discrimination logic for reducing the amount of data and keeping the most interesting events. It will have 6 hermetic cylindrical "barrel" layers in the central region, covering the region of $|z| < 1200\ mm$, complemented on each side by five hermetic double. Three sub -detectors are distinguished, the Tracker Barrel with PS modules, TBPS; the Tracker Barrel with 2S modules, TB2S; and the Tracker End -cap Double -Discs, TEDD [50].

The Outer Tracker will provide data both for the L1 reconstruction (for each bunch crossing every $25\ ns$) in order to maintain the first level Trigger rate to its current value of $100\ kHz$. At present tracking data is used only in the High Level trigger In order to deliver information to the Level -1 trigger the system has to send signals at a rate of $40\ MHz$, feasible only by reducing the sent data to maintain the overall bandwidth at an acceptable level.

The modules that are currently under consideration will be closely spaced sensors with the capability of rejecting signals from low p_T particles. These can be achieved by taking advantage the strong bending power of the CMS solenoid magnet of approximately $3.8\ T$. As the particles move in the magnetic field their trajectories are curved according to the Lorentz Force. The bending depends on the particles charge, their transverse momentum and the field. The momentum perpendicular to the Magnetic filed can than be determined by

$$p_T = qBR \tag{3.4}$$

where q is the charge B the magnetic field and R the radius of the bended curvature.

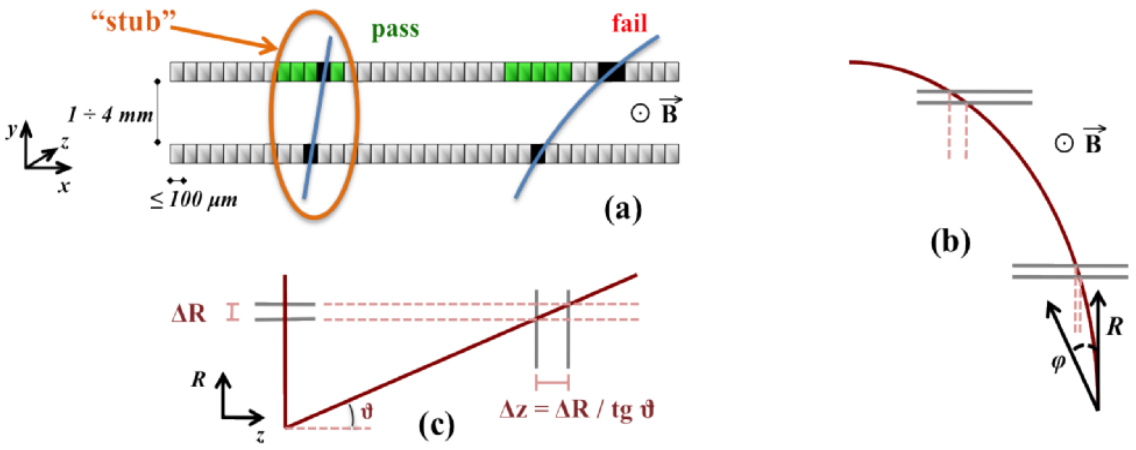

Figure 3.15: *Correlation of signals in closely -spaced sensors enables rejection of low -p_T particles; the channels shown in light green represent the "selection window" to define an accepted "stub". (b) The same transverse momentum corresponds to a larger distance between the two signals at large radii for a given sensor spacing. (c) For the end -cap disks, a larger spacing between the sensors is needed to achieve the same discriminating power as in the barrel at the same radius. The acceptance window can therefore be tuned along with the sensor spacing to achieve the desired p_T filtering in different regions of the detector.[50]*

The transverse charged particles with low p_T follow a more bended trajectory than the high

p_T particles. By combining the hit information from the close spaced sensors one can estimate the transverse momentum p_T locally in each detector module, as shown in Figure 3.15. A threshold of around 2 GeV corresponds to a data volume reduction of roughly one order of magnitude, which is sufficient for the purposes of L1 data transmission [50].

The whole procedure is called stub finding logic and is implemented in the new read-out chip of the modules. The read -out chip is called CMS binary chip (CBC) providing binary data suitable for the above described p_T discrimination. The front -end hybrids are connected at the edges of the two sensors, significant inactive surface on the two ends of the sensors is unavoidable. In order to overcame this issue hermetic layers are used, overlap between modules is required on all four edges of the sensors.

The first three barrel layers, that will be populated with PS modules, will be tilted, nearly perpendicular to incident particles over the entire barrel length. This done in order to prevent inefficiencies in the stub finding when the incident particles cross the module near the center with a large incident angle[50].

There are three type of sensors under consideration for being implemented with the discrimination logic described above.

The 2S module

The 2S consists of, two strip sensors read out at the edges by the same set of front-end ASICs that implement the correlation logic. The two sensors will cover an a area of $10 \times 10\ cm^2$ with 5 cm long strips and a pitch of 90 μm and they have their strips in parallel. The strip length is half of the sensor length with both sensor having 2032 (2 rows of 1016) strips with a width to pitch ratio of 0.25. The distance between the sensors will be $1.8\ mm$ to $4.0\ mm$ depending on where they are located inside the Tracker. These modules will be used in the end-cap disks as well as also at the central barrel region of the Tracker at the outer regions, above $R \approx 60\ cm$ (red layers oat Figure 3.14)[47].

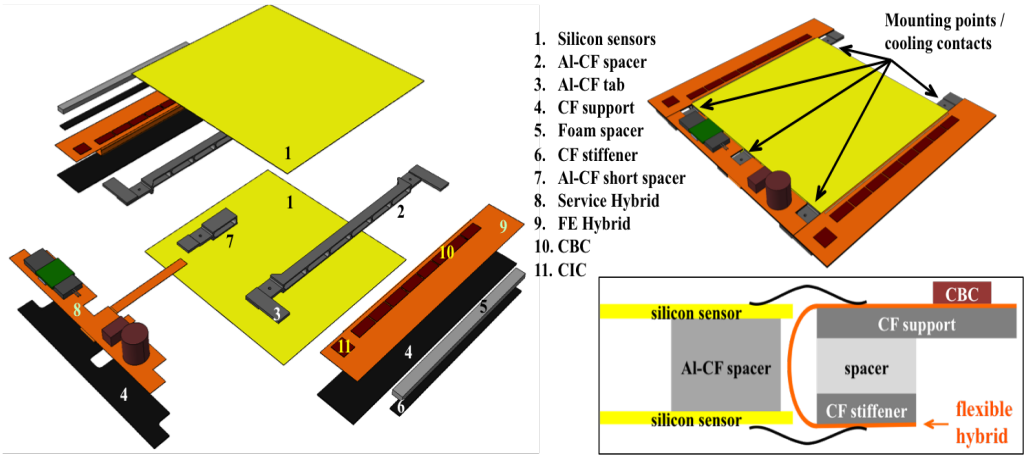

Figure 3.16: *3D schematic of the 2S module components (left), 3D view of the assembled module (upper right), and a sketch of the FE Hybrid folded around its support (lower right). The module is mounted on five cooling elements on the mechanical support structure[47]*

Figure 3.16 shows a schematic of the 2S module. The two sensors are mounted together on a

mechanical structure that provides support and cooling. The sensors are glued to two long carbon fiber aluminum elements that provide support and heat dissipation (AL -CF spacers).

On each end of the 2S sensor module, both sensors strips are wire bonded to the flexible front end (FE Hybrid) which is folded over a carbon fiber spacer matching the separation distance of the two sensors. Each front end (FE) hybrid hosts 8 CMS binary chips CBCs. This Binary chips incorporate logic of stub finding. It process data from 254 strips (127 bottom and 127 top) and identifies wide cluster of hits that correspond to low p_T particles , then for each cluster in the inner sensor a search is made for a hit in a coincidence window in the outer sensor [51].

The sensors are wire-bonded from top and bottom to the readout hybrids, which each carry eight CMS Binary Chips (CBCs). This Binary chips will incorporate logic to identify L1 trigger primitives in the form of "stubs". The signals of the CBCs are fed by a CIC concentrator chip to the service hybrid which transmits the data via a multi -gigabyte transceiver.

The main limitation of this type of module is the lack of segmentation in the z direction. In addition, the relatively long strips limit the use of this module to the radial region above 40 cm, because of occupancy.

The PS module

The other type of modules with p_T discrimination logic that will be implemented are modules composed of two sensors with a whole surface of $5 \times 10\ cm^2$. The one sensor is segmented into strips (called PS-s) of $2.5\ cm$ long strips and $90\ \mu m$ pitch, and the other segmented into "macro-pixels" of size $100\ \mu m \times 1.5\ mm$ which is called PS -p sensor The PS -s sensor will be an AC -coupled sensor, while the PS -p will be a DC sensor [47].

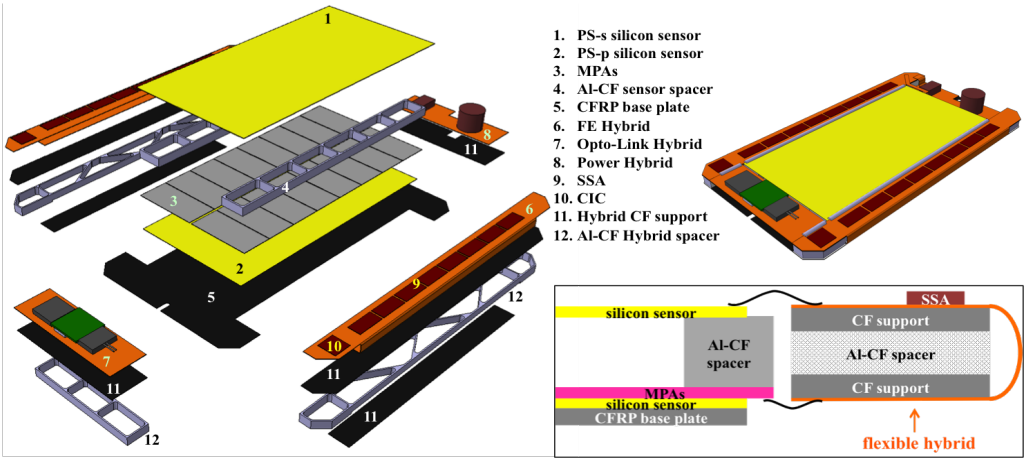

Figure 3.17: *3D schematic of the PS module components (left), 3D view of the assembled module (upper right), and a sketch of the FE Hybrid folded around its support (lower right). The module is mounted on five cooling elements on the mechanical support structure[47]*

The PS modules will be placed closer to the interaction point, between radii $R \approx 20\ cm$ and $R \approx 40$, due to the required higher resolution in these regions (blue regions in Figure 3.14). The pixelated sensors provide with the 1.5 mm width in the z coordinate sufficient precise measurements in the z coordinate offering an effective pattern recognition in the 3D dimensions in more sufficient way than extending the Pixel detector to larger radii.

Two different front-end chips will be developed, one that will be wire bonded to the strip sensor (PS -s) named Short Strip ASIC (SSA) and one that will be bumb -bonded to the pixel sensor (PS -p) named Macro-Pixel ASIC (MPA). The correlation of strips will be handled from the MPA chip. The SSA is connected to the FE-Hybrid in both sides of the modules it process signals from the strip sensors and sends them to the MPA.

The PS -p sensor and the readout chips can then be handled as a single module. Both sensors are attached to a carbon fiber polymer base plate that acts as carrier and provides a thermal path for heat dissipation. Between the two Sensors there is an AL-CF spacer as in the case of the 2S module.

Two rows of 8 MPA chips are bumb -bonded to the pixel sensor. It correlates the bottom macro-pixel hits with the received hits from the SSA and builds clusters and stubs. As in the case of the 2S module the input and output data are transfered from the same CIC chip which collect the data from all MPA to the Service Hybrid.

3.5.3 Electrical specifications and quality assurance

The production of the sensors will be contracted to qualified industrial partners. The qualification of suitable vendors is ongoing at the time. The final selection of material (MCz, FZ or ddFZ), physical thickness, strip isolation technique (p -stop or p -spray), and production technology (6" or 8") will depend on the capabilities and costs offered by the selected companies.

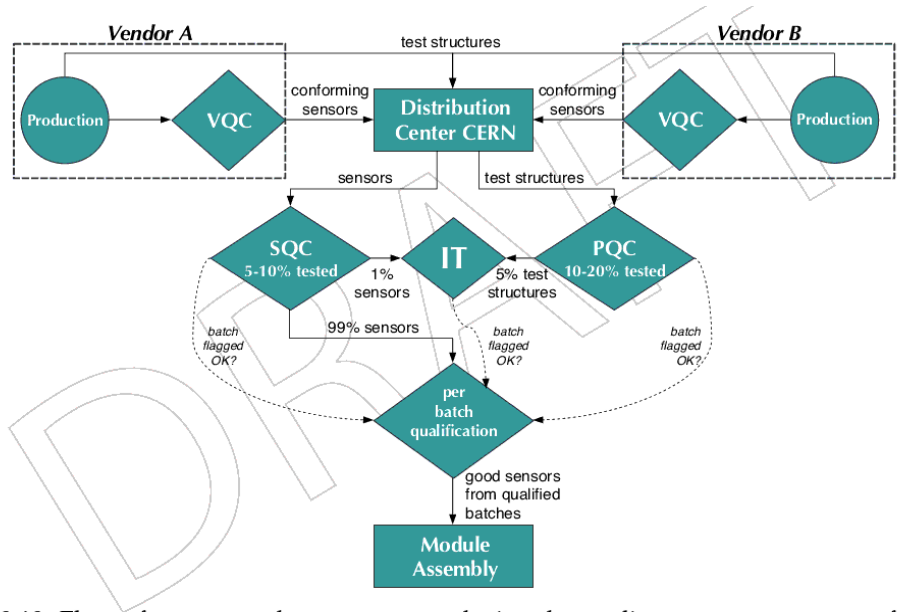

Figure 3.18: *Flow of sensors and test structures during the quality assurance program for the series production.[50]*

Sensors that can provide the expected performance over the full lifetime of the detector will be integrated into modules. To assure that sensors are of sufficient quality, each has to comply to a detailed set of electrical specifications. A preliminary set is listed in 3.19. The compliance with these specifications will be tested in four different quality control procedures, to monitor the production. The quality assurance program, including Vendor Quality Control (VQC), Sensor Quality Control (SQC)Process Quality Control (PQC) and Irradiation Tests (IT). The VQC is per-

Measurement type	Acceptance value/window	Measured at VQC	SQC	PQC	IT
Global measurements (2S, PS-s, and PS-p)					
Full depletion voltage	$V_{fd} < 150$ V for 200 μm	✓	✓	✓	✓
	$V_{fd} < 300$ V for 300 μm	✓	✓	✓	✓
Current at 500 V	$I_{500} \leq 2\,nA/mm^3$	✓	✓	✓	✓
Breakdown voltage	$V_{break} > 700$ V, $I_{700} < 3 \times I_{500}$	✓	✓	✓	✓
Longterm stability	$\lvert\Delta I_{500}/I_{500}\rvert < 30\%$ for 48 hours	-	✓[1]	-	-
Measurements after irradiation (2S, PS-s, and PS-p)					
Breakdown voltage	$V_{break} > 1000$ V, $I_{1000} < 4 \times I_{700}$	-	-	-	✓
Interstrip resistance	$R_{int} > 100\,M\Omega cm$	-	-	-	✓
Strip measurements (2S and PS-s)					
Strip current	$I_{strip} \leq 2\,nA/cm$	✓	✓	-	✓
Bias resistor					
median per sensor	median(R_{poly}) = 1.5 ± 0.3 MΩ	✓	✓	✓	-
per strip	R_{poly} = median(R_{poly}) ± 5%	✓	✓	-	-
Coupling capacitance	$C_{ac} > 1.2\,pF/(cm\,\mu m)$	✓	✓	✓	-
Interstrip resistance	$R_{int} > 10\,G\Omega cm$	-	✓[1]	✓	✓
Interstrip capacitance	$C_{int} < 1\,pF/cm$	-	✓[1]	✓	✓
Pinhole check	$I_{diel} < 1$ nA at 10 V	✓	✓	-	-
Number of bad strips	$N_{bs} < 0.5\%$	✓	✓	-	-
incl. open/shorted strips					
Macro-pixel measurements (PS-p)					
Pixel current	$I_{pixel} \leq 300\,pA/cm$	-	-	✓	-
Interpixel resistance	$R_{int} > 1\,G\Omega cm$	-	-	✓	-
Number of bad pixels	$N_{bp} < 0.2\%$	-	-	-	-
Measurements on dedicated teststructures					
Strip/pixel implant resistivity	$R_{strip} < 250\,\Omega$/square	-	-	✓	-
Strip/pixel alu resistivity	$R_{alu} < 25\,m\Omega$/square	-	-	✓	-
Dielectric breakdown	$V_{diel} > 150$ V, $I_{diel} < 10$ nA at 150 V	-	-	✓	-

[1] Only for a smaller sample of sensors, approximately 1% of the full quantity.

Figure 3.19: *Electrical specifications of sensors.[50]*

formed on each sensor by the producers, while the other procedures are performed on a sample basis by the CMS collaboration. PQC is performed on dedicated test structures only. The quality assurance program is illustrated in Figure 3.18. The electrical specifications for the characterization of sensors and test structures from the series production are derived from there and a set is shown in Figure 3.19. [50].

Chapter 4

Electrical Characterization of silicon sensors and Test structures

4.1 Introduction

In this chapter the experimental procedure of characterizing silicon detectors is described. The electrical parameters of test structures and mini -sensors, of the two new modules the 2S and PS , that will be installed at the Phase II upgrade of the CMS Outer tracker, has been measured at the laboratory of detector instrumentation of NCSR Demokritos. .

Electrical qualification of silicon sensors in High Energy Physics is an important aspect of the design of silicon detectors. Electrical parameters give access to information necessary to understand the production process and quality, but they also yield important information about radiation damage and general performance. In order to design and construct the optimum detector system a deep understanding of the different characteristics of the detector is needed. The measurements that are performed include:

- Visual inspection to identify scratches and broken parts.
- Total leakage current measurements (IV).
- Total Capacitance measurements (CV).
- Leakage current scans per strip (IV).
- Polysilicon resistance measurements on each strip (R_{bias}).
- Inter-strip Resistance (R_{int}).
- Inter-strip Capacitance (C_{int}).

The test structures and mini sensors that have been tested are the MSSD sensor (Multi geometry silicon strip sensor) from the first wafers of HPK campaign, also diodes, MOS and baby sensors from the 2S prototype wafers and PS -p light sensors from the PS -p prototype wafers.

4.1.1 The wafer and materials

The wafer has been produced with a variety of structures, each intended for a different purpose. There are test structures to qualify and monitor the quality of the production process and determine operating parameters as well as mini sensors. These allow the investigation of geometry and materials on resolution, noise and signal-to-noise ratio. More details can be found at [52], [53] In figure 4.1 the wader of HPK (Hamamatsu Photonics) campaign is shown.

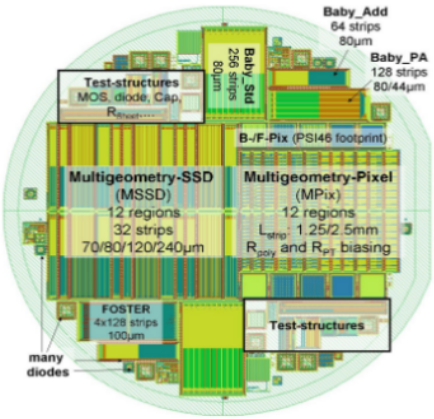

Figure 4.1: *Wafer of HPK campaign. The layout of the R&D wafer with many devices such as multi geometry strip sensors $MSSD$, multi geometry pixel sensors $MPix$), Test structures, diodes and mini sensors ($BabyStd$, $BabyAdd$),a mini -strip sensor with integrated pitch -adapter ($BabyPA$).*

Another aspect of the sensor $R \wedge D$ is the investigation of layout variations. A very important parameter is the strip pitch, which has an impact on the strip capacitance, which in turn significantly affects the sensor noise. The most important parts of the HPK campaign wafers are:

- Diodes: They are used to test material properties through electric measurements (Current over Voltage (IV),Capacitance over Voltage (CV)) and dark current measurements.
- Test Structures: They are used to qualify and monitor the quality of the production process and determine operating parameters . These include mini sensors for beam tests and source measurements and allow investigation of the influence of geometry and materials on resolution, noise and signal -to -noise ratio. The type of measurements that can be performed on this structures are: inter -strip parameters such as interstrip capacitance and interstrip resistance as well as dialectic break down voltages.
- Baby sensors: These structures are used for evaluation of radiation hardness of the different materials. IV and CV measurements, strip characterization, charge collection measurements (results presented in this paper) and Lorentz Angle measurements.
- *Multi Geometry Silicon Strip Detector* The MSSD contains 12 different regions with different pitches and width -to -pitch ratios. Each region has 32 strips with pitches from 70 to $240\mu m$. Those geometry layouts are the most probable to be used in the Phase II upgrade of the inner region of the strip CMS tracker. These sensors allow the determination of geometry and materials and the influence of them on resolution and signal to noise ratio.

The interstrip capacitances are very interesting on this multi -geometry -structure, as they dominate the load capacitance of the read-out chips and therefore the noise.

- *Multi Geometry Pixel Detector* This structure is used for characterization of a sensor with very sort strips $(1-2)\ mm$, varying pitch and biasing connection (poly-silicon resistance, punch through). The main focus of multi-geometry pixel structures are the capacitance measurements and investigation of their response to signal to noise ratio. In order to maintain a good resolution in the higher track density of the sLHC one possible solution is the use of strixels. These strixels sensors contain segmented strips with a larger area compared to the pixel detector.

The layout 4.1 has been implemented with different thicknesses and different technologies for the substrate production. It has been shown from previous $R \wedge D$ that silicon substrates with a high oxygen concentration show a higher degree of radiation tolerance. The processing techniques that are currently under investigation are:

- Float-zone (FZ): the best known material which serves as a reference and has also a high quality in terms of the high resistance values.
- Magnetic Czochralski (WCz): This growth technique results in a high oxygen concentration.
- Epitaxial : This method allows to produce very thin (25 -100 μm) active sensors by chemical vapor deposition of silicon one a carries wafer, also resulting in high oxygen concentration

4.2 Experimental Setup

Electrical measurements on silicon sensors are performed with a semi-automated probe station (Carl Susse PA 150). The whole setup is inside a light tight aluminum box which works as a Faraday cage and prevents electromagnetic interference and also provides a dark environment for the measurements 4.2α'. The signals are collected from the Electrometer (Keithley 6517) and the Impedance analyzer (HP4192A) while the whole system can be controlled by a PC running LabView 4.2β'. The whole room of the laboratory has a temperature and humidity control system 4.2δ'.

The sensor is placed onto the chuck which has vacuum pipes and also it can provide a high voltage by a contacting surface 4.2α'. The vacuum is necessary for fixing the structures to be tested and it not let the structure to move onto the chuck. The chuck is attached to a motorized table that is used in order to precisely move the sensor to X, Y and Z axis by a few micrometers. The movement can be done with a joystick semi-manually or automatically by the LabView program 4.2γ'.

The AC, DC pads and the bias line are contacted by micro manipulators which have very thin probes. Strip scans are performed by bringing these probes into contact with the pads, lowering the chuck, and moving the chuck until the next strip is located below the probes.

The biasing is applied to the contacting chuck or the bias line of the sensors. The other probes contact the AC or DC pads of each strip. The placement of the probes can be done by using the microscope for viewing the exact position of the probes.

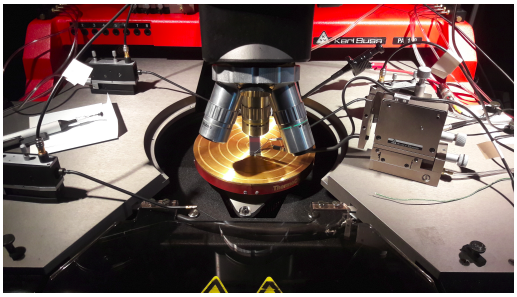

(α′) *Probe station inside the light tight box (Carl Susse PA 150)*

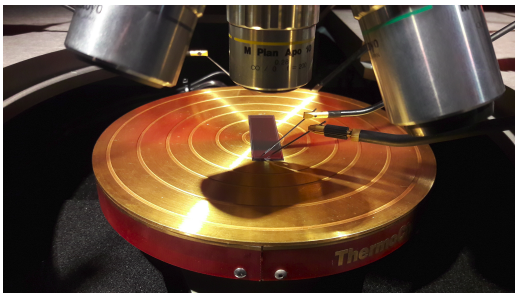

(β′) *Probe station closer look*

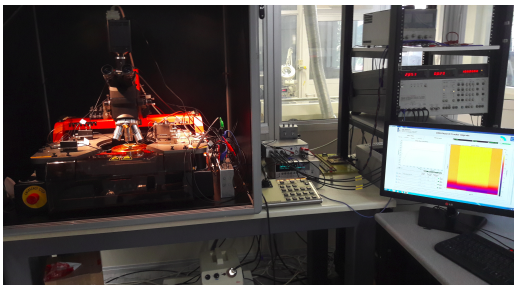

(γ′) *The whole experimental equipment for electrical characterization of silicon sensors. The whole setup is controlled by a PC that runs LabView*

(δ′) *Temperature and himidity control*

Figure 4.2: The laboratory of detector instrumentation in NCSR Demokritos where the characterization of silicon sensors is performed

The measurement equipment is consists of :

- *Electrometer (Keithley 6517)* This device has a Voltage source with a range of $\pm 1000V$, a maximum current of 1 mA and an additional electro meter which is completely isolated from the voltage source. The electro meter is used for all current measurements.
- *Impedance analyzer (HP4192A)* These LCR meters are used for capacitance measurements. It has a test frequency range from 5 Hz to 13 MHz.

4.3 Multi Geometry Silicon Strip Sensor MSSD

The Multi Geometry Silicon Strip Sensor is the largest structure of the wafer and exists twice on each wafer. Each structure has a total area of $65.74 \times 32.08\ mm$ and 384 total number of strips. The available pitches are 70, 80, 120 and 240 μm and the width -over -pitch ratios are around 0.15, 0.25 and 0.35, with slight variations.

As mentioned in the previous section, the sensors are divided in 12 regions with different pitches and width to pitch ratios.4.3. Was designed to investigate the influence of strip and sensor geometry on parameters like depletion voltage, leakage current and front -end amplifier input capacitance. The total strip capacitance, which is the sum of backplane C_b and inter -strip capacitance C_{int} as well as the leakage current determine the signal to noise ratio of the sensor. Also the inter -strip capacitance determine the charge sharing between the strips and thus the

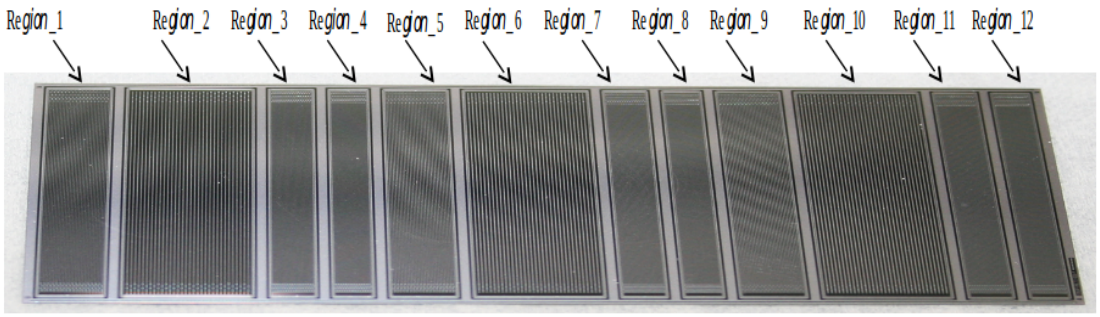

Figure 4.3: *The Multi geometry Silicon Sensor. The sensor has 12 regions with different pitches and width to pitch ratio.*

position resolution. The capacitive load of the preamplifier input, mostly depends on the strip capacitances of the sensor. So the capacitances and the geometry of the sensor play an important role in the operation of the detector.

The 12 regions work as individual sensors and all have their own bias and guard ring. All are separated by a deep n+ implant, which penetrates all the way to the backplane, and thus separates the regions. The strips are polysilicon -biased and AC -coupled for direct bonding to a front -end chip.

The geometrical characteristics of each region are described in the table 4.1.

Label	1(120)	1(240)	1(80)	1(70)	2(120)	2(240)	2(80)	2(70)	3(120)	3(240)	3(80)	3(70)
Region	1	2	3	4	5	6	7	8	9	10	11	12
Pitch	120	240	80	70	120	240	80	70	120	240	80	70
Width	16(+1)	34(+1)	10(+1)	8.5(+1)	28(+1)	58(+1)	18(+1)	15.5(+1)	40(+1)	82(+1)	26(+1)	22.5(+1)
Width Al	29(−5)	47(−5)	23(−5)	21.5(−5)	41(−5)	71(−5)	31(−5)	28.5(−5)	53(−5)	95(−5)	39(−5)	33.5(−5)
w/p	0.133 (0.142)	0.142 (0.146)	0.125 (0.138)	0.121 (0.136)	0.233 (0.242)	0.242 (0.246)	0.225 (0.238)	0.221 (0.236)	0.333 (0.342)	0.342 (0.346)	0.325 (0.338)	0.321 (0.336)

Table 4.1: *The Geometrical Characteristics of each Region of the MSSD sensor*

4.3.1 Experimental Results

The following structures have been received and tested at NCSR Demokritos.

- $FZ320P\_02\_MSSD\_1$
- $FZ120P\_05\_MSSD\_2$

These structures are made with Float Zone technique with detector thicknesses $d = 320\mu m$ and $d = 120\mu m$.

The parameters that was measured are the total leakage current, the intre -strip capacitance and the backplane capacitance by changing the voltage.

Global leakage Current

In this set of measurements the Current over Voltage curve is extracted(IV). The bias voltage is slowly increased from zero to several hundred Volts and the total current of the strips is measured on each step. These type of measurements are fundamental for the characterization of the detectors. The IV curves of the pn junctions of the detector must have a specific shape in order to work properly, similar to a reversed biased diode. If the IV curves are not showing these specific characteristics then the sensor is defected.

The bias Voltage is applied on the backplane of the detector and the connection to ground is made at the bias ring. The connection with the strip is made throw the polysilicon resistors. This ensures that all strips are at the same potential. Depending on the doping of the particular sensor, the high voltage has to have positive polarity for n -type and negative polarity for p -type.

The IV curves for sample MSSD 120 is shown in the figures 4.4α′ ,4.4β′. The measurements where performed at 23^oC and scaled to 20^oC from equation 1.55

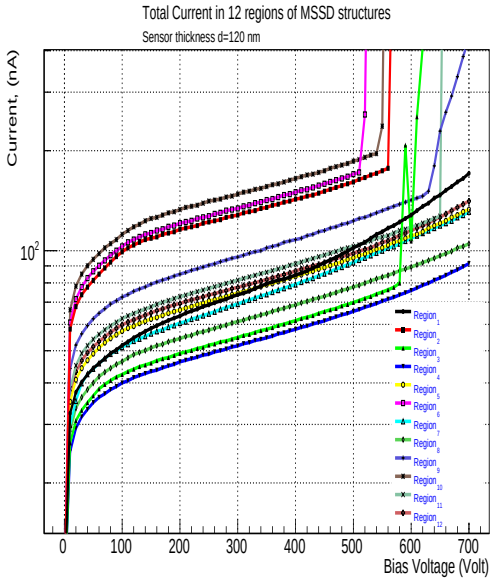

(α′) *Global current of Multi Geometry Silicon sensor with 120 detector thickness. Logarithmic scale*

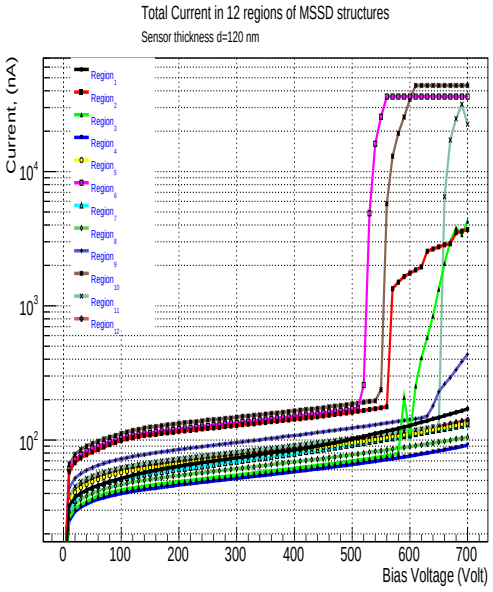

(β′) *Global current of Multi Geometry Silicon sensor with 120 detector thickness.*

The 12 regions show good Current -Voltage characteristics with a breakdown Voltage above $500V$

Backplane Capacitance

The backplane Capacitace of all the 12 regions was measured for MSSD 120, MSSD 320. The experimental results can be seen in 4.5α′ , 4.5β′.

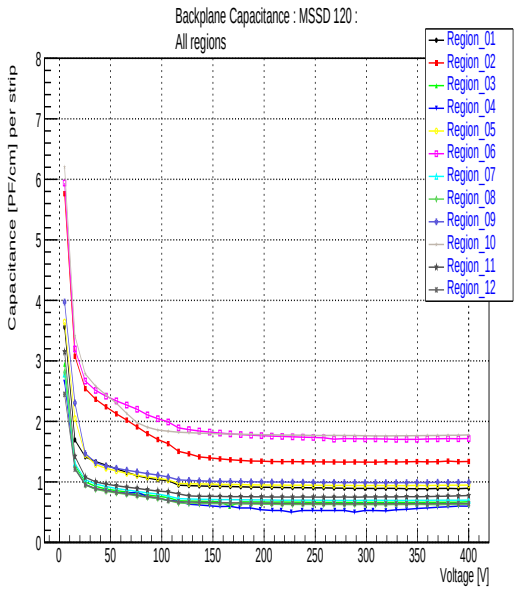

(α′) *Backplane Capacitance MSSD 120 µm*

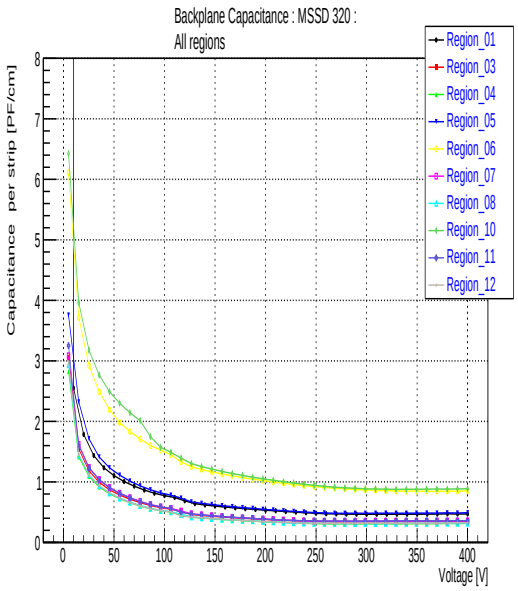

(β′) *Backplane Capacitance MSSD 320 µm*

Interstrip Capacitance

The interstrip Capacitace of all the 12 regions was measured for MSSD 120, MSSD 320. The experimntal results for region 1 of MSSD 120 and region 3 can be seen in 4.6α′ , 4.6β′.

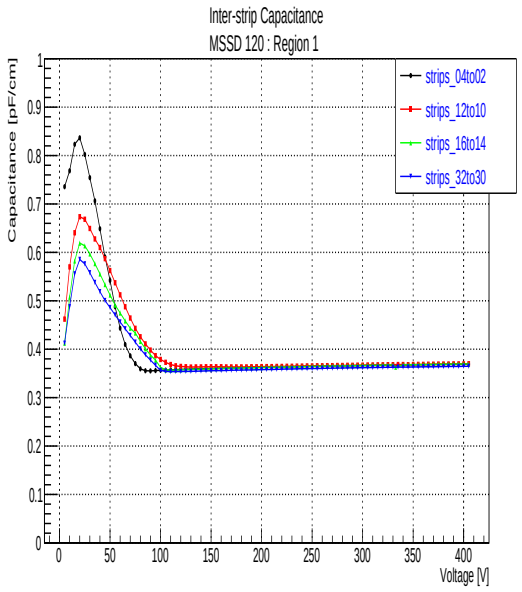

(α′) *Interstrip Capacitance MSSD with thickness 120 µm*

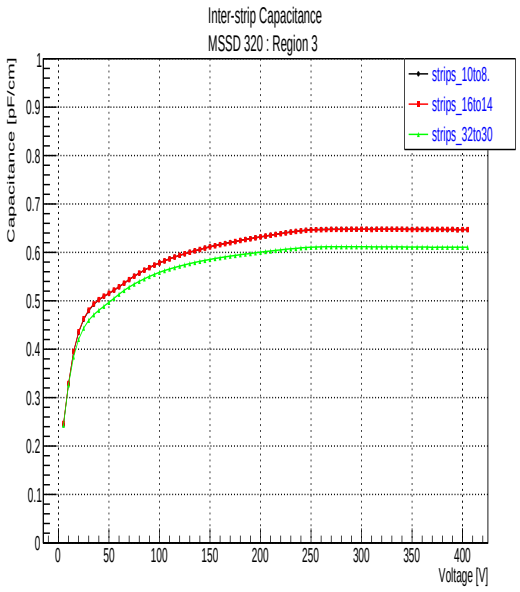

(β′) *Interstrip Capacitance MSSD with thickness 320 µm*

Comparison of Experimental and Simulated Results

In this section a comparison is made between the experimental values of the baby sensors with numerical calculations. The numerical calculations was made by a program that solves the 3D Laplace equation for silicon sensors with strip geometry. For more details about the method of the calculations and the program can be found in [54], [55].

This program can be used as a Simulation tool for approximating the Capacitances depending on the geometry The algorithm has an accuracy of 25% and has the advantages that is fast and free compared to other costly and time consuming Programs like TCAD.

In figures 4.7α′ , 4.7β′ the calculated and the experimental values of the Backplane Capacitance are shown for all the 12 regions of MSSD 120 and 320. The calculated results approximate very well the experimental and the absolute difference is less than 25%. Also in figures 4.8α′ , 4.8β′ a comparison is made for the interstrip capacitance. Two regions region 2 and 9 of MSSD 320 were damaged and have been excluded from the graphs

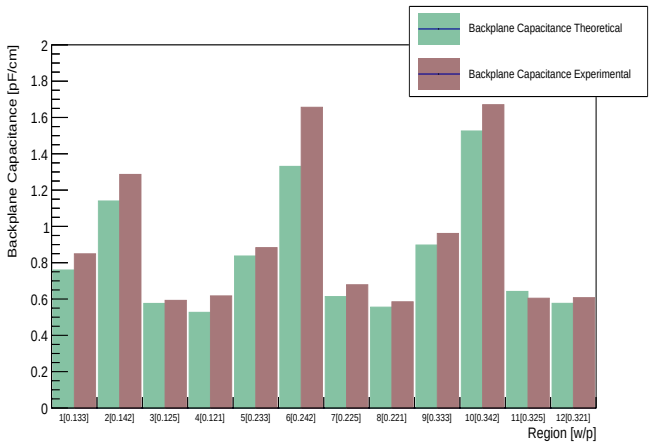

(α′) *Comparison of Experimental and Simulated values for all the 12 regions of MSSD 120 µm. Backplane Capacitance*

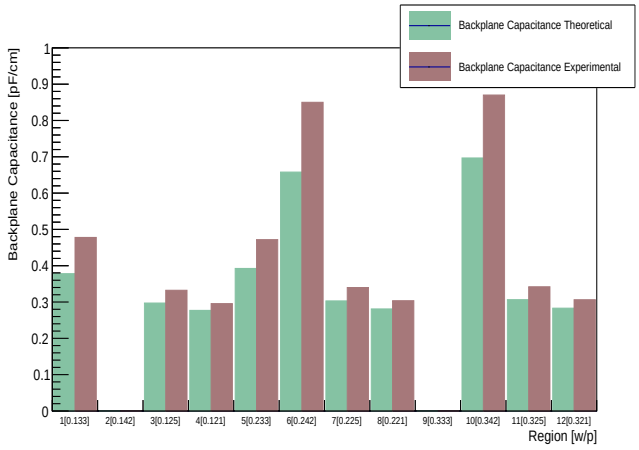

(β′) *Comparison of Experimental and Simulated values for all the 12 regions of MSSD 320 µm. Backplane Capacitance*

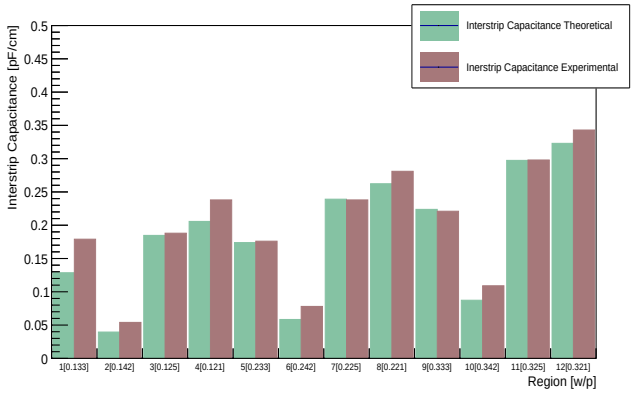

(α′) *Comparison of Experimental and Simulated values for all the 12 regions of MSSD 120 µm. Interstrip Capacitance*

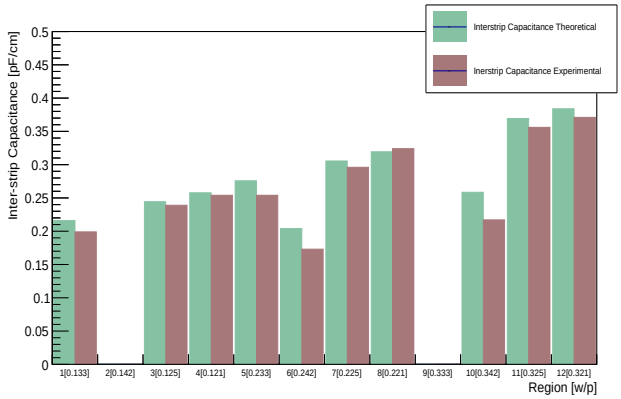

(β′) *Comparison of Experimental and Simulated values for all the 12 regions of MSSD 320 µm*

4.4 Electrical characterization on 2S wafer prototype

Sensors for the Standard 2S modules have been designed by CMS and were produced by Hamamatsu Photonics. Those are 6 -inch p -substrate FZ wafers with a resistivity of $3 - 8k\Omega cm$ and a physical thickness of $320\mu m$. Several wafers where produced with p -stop strip isolation technique while others where produced by p -spray technique . This isolation is needed to avoid accumulation of oxide charges. The active thickness is $240\ \mu m$ using the deep diffusion technique where the backside implant is deeply diffused into the bulk enabling a smaller active area.

The wafer layout is shown in 4.9. It contains the main sensor with an approximate size of $10 \times 10\ cm^2$. The total sensor is split in two rows with 1016 strips in each row (2032 in total). The sensor is AC -coupled and biased via polysilicon resistors. Each strip has a $90\ \mu m$ pitch and a strip length of $5\ cm$ with a width to pitch ratio of 0.25.The main sensor is surrounded by several test stractures, mini-sensors,diodes and MOS. 4.9.

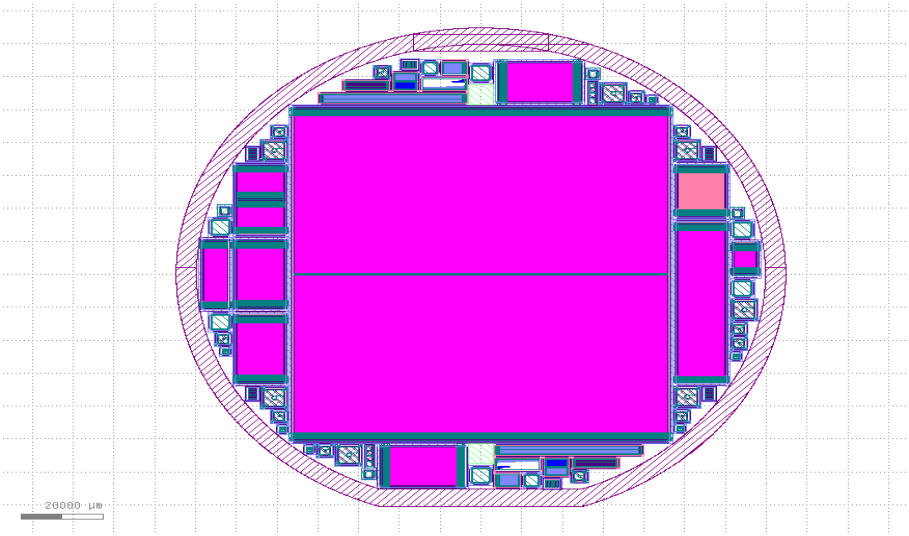

Figure 4.9: *The 2S 6" prototype wafer as it is shown from kLayout program (GDS viewer)*

Several test structures and mini-sensors of the HPK 2S 6" ddFZ240 were tested at the detector instrumentation lab at NCSR Demokritos and can be shown in the next table

	Material		Quantity	Serial Number	Chip
HPK 2S 6" ddFZ240	P-stop	Baby Sensors	2	21	6
				22	6
		PstopGeo	2	12	17
				16	17
		Test structures	2	Serial Number	Chip
		VDP Flute (Upper Left)		21 , 22	4
		D_1PS_2GR		21 , 22	13
		MOS & Diode		21 , 22	15
		Sims (Left)		21 , 22	16
		HMSet (Left)		21 , 22	18
	P-spray	Baby Sensors	1	29	6
		Test structures	1		
		VDP Flute (Upper Left)		29	4
		D_1PS_2GR		29	13
		MOS & Diode		29	15
		Sims (Left)		29	16
		HMSet (Left)		29	18

4.4.1 Diodes

Diodes are used in order to study the material, the changes of the bulk properties before and after irradiation and also giving information about the properties and the behavior of the different materials. The standard type of measurements are current over voltage and capacitance over voltage.

There are different set of diodes with different shapes and surfaces called Full diode, Half diode , Quarter diode and Round Diode 4.10 in each of the Test structures sample. Each one diode has a separate guard ring that surrounds the active area of the diode.

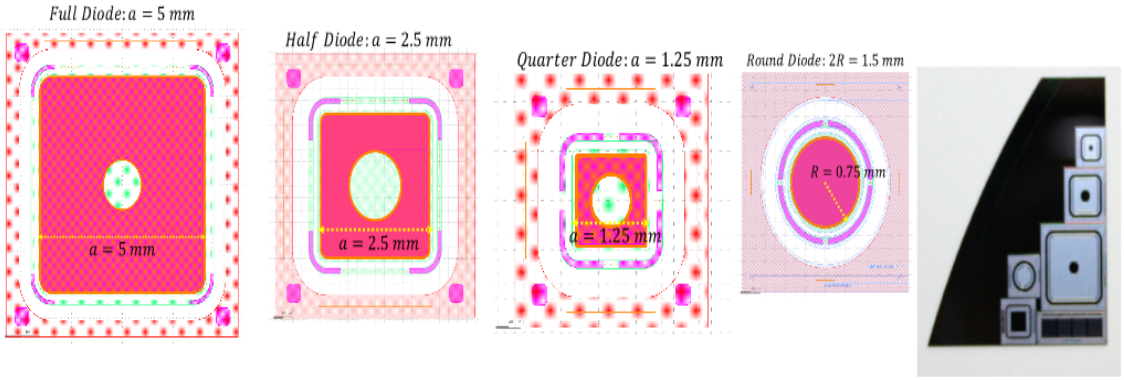

Figure 4.10: *The four different set of diode test structures and an actual picture of a sample with test structures.*

The diodes that have been tested have been made with different isolation techniques. There are two sets of diodes with p -stop isolation technique with Serial Number 21, Serial Number 22 and one set with p -spray isolation technique with Serial Number 29 as shown in the previous table. Each one has the four different set of diodes 4.10.

Capacitance-Voltage measurements

The CV measurements on diodes are made by applying the high voltage on the backplane and the low voltage to the upper surface of the diode while keeping the guard ring grounded. The silicon bulk is biased by a voltage varied between 0 and 700 V, where the capacitance is measured at steps of 5 V. After the measurement procedure the graphs of $(1/C^2)$ vs voltage are made. The capacitance of each diode is scaled with the surface. As mentioned in chapter 1 the inverse square of the Capacitance $(1/C^2)$ with applied Voltage is given by equation1.60

p -stop Diodes (Serial Number 21)

The four different diodes of sample 21 where measured. The graphs show similar characteristics 4.11α'. The Capacitance drops with the voltage increase ($(1/C^2)$ rises) until the depletion Voltage is reached where it remains stable. By making a linear fit in the horizontal part of the graph (where the capacitance is stable) and the inclined part (where capacitance drops) and by calculating the intersection of the two linear functions the depletion Voltage (V_d) is calculated

as well as the depletion Capacitance (C_d). And from the slope of the inclined graph the concentration of the substrate is calculated.

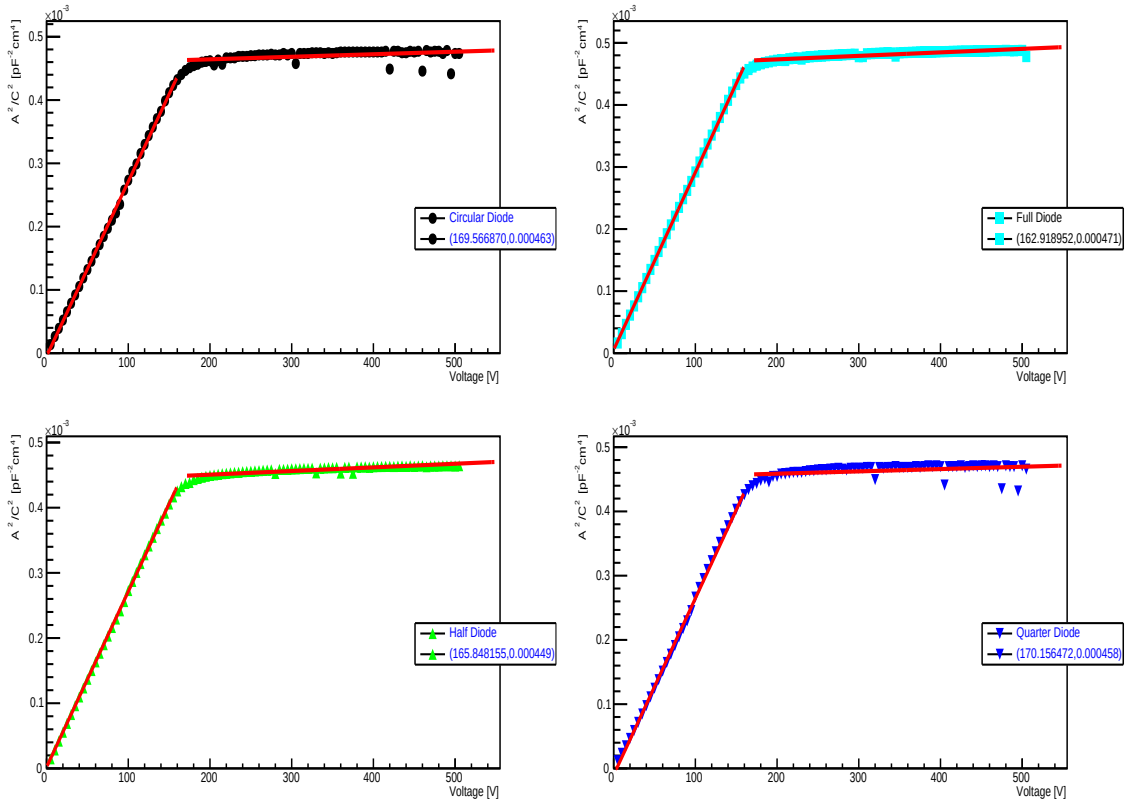

(α′) $(1/C^2)$ *versus voltage for* $SN21$ *test structure set. By fitting the horizontal and inclined part of the graph and calculating the intersection point the depletion Voltage and the depletion Capacitance are calculated, while the slope is* $\propto 1/N_d$

The results are sumarized in the table 4.2.

Diode Name	$A\ [cm^2]$	$N_d\ [cm^{-3}]$	V_d [Volts]	$A^2/C_d^2\ [pFcm^4]$	C_d
Full diode	0.2500	$4.20 \cdot 10^{12}$	162.92	$4.71 \cdot 10^{-3}$	11.51
Half diode	0.0625	$4.46 \cdot 10^{12}$	165.85	$4.49 \cdot 10^{-3}$	2.95
Quarter diode	0.0156	$4.37 \cdot 10^{12}$	170.16	$4.58 \cdot 10^{-3}$	0.73
Circular diode	0.0176	$4.35 \cdot 10^{12}$	169.59	$4.63 \cdot 10^{-3}$	0.82

Table 4.2: *Serial Number 21 Experimental Results*

p -stop Diodes (Serial Number 22)

By following the same procedure the Diodes of Serial Number 22 are characterized.

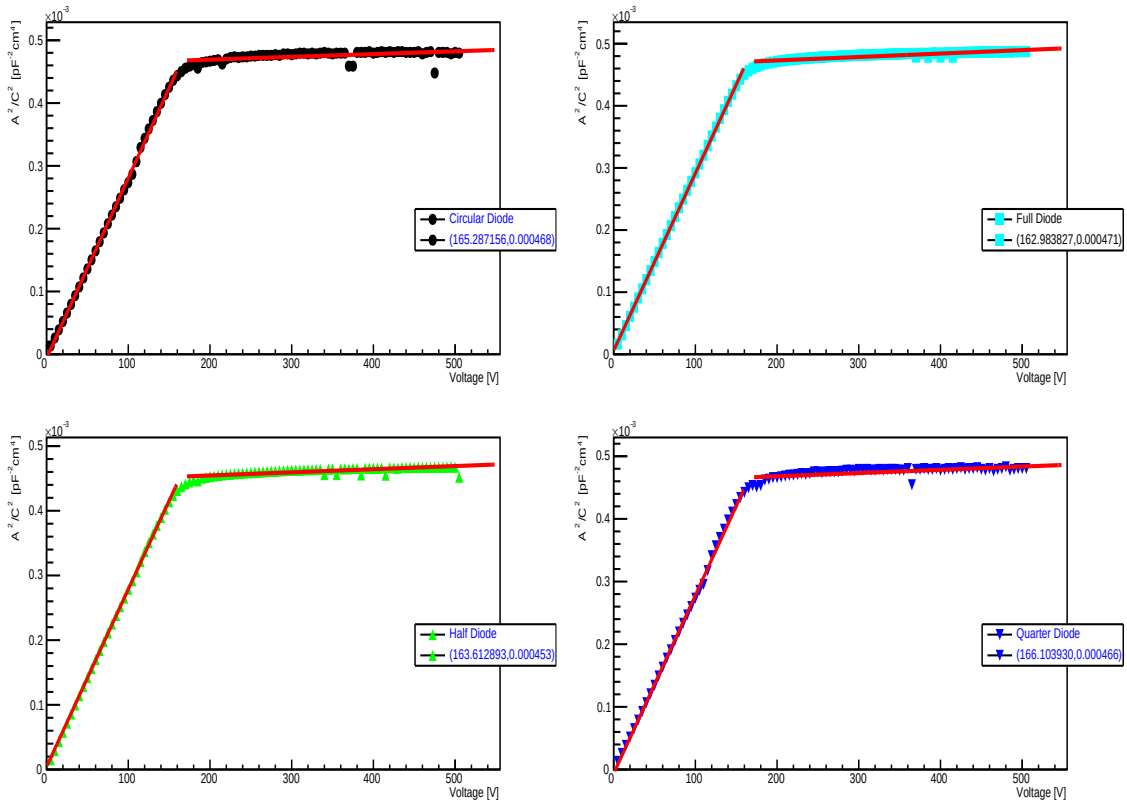

(α′) $(1/C^2)$ *versus voltage for* $SN22$ *test structure set.*

The results are summarized in the table 4.3.

Diode Name	$A[cm^2]$	$N_d\ [cm^{-3}]$	V_d [Volts]	A^2/C_d^2	C_d [pF]
Full diode	0.2500	$4.21 \cdot 10^{12}$	162.98	$4.71 \cdot 10^{-4}$	11.52
Half diode	0.0620	$4.38 \cdot 10^{12}$	163.61	$4.53 \cdot 10^{-4}$	2.94
Quarter diode	0.0156	$4.22 \cdot 10^{12}$	166.10	$4.66 \cdot 10^{-4}$	0.72
Circular diode	0.0176	$4.19 \cdot 10^{12}$	165.29	$4.68 \cdot 10^{-4}$	0.82

Table 4.3: *Serial Number 22 Experimental Results*

p -spray Diodes (Serial Number 29)

By following the same procedure the Diodes of Serial Number 29 are characterized.

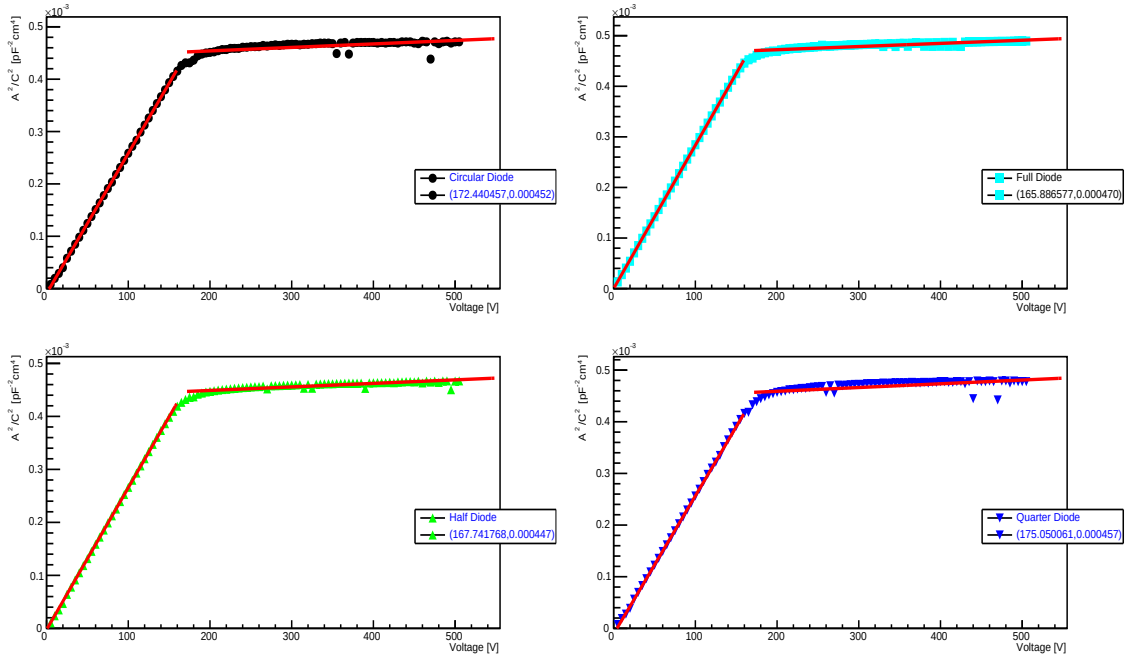

(α′) $(1/C^2)$ *versus voltage for* $SN29$ *test structure set.*

The results are summarized in the table 4.4.

Diode Name	$A[cm^2]$	$N_d\ [cm^{-3}]$	V_d [Volts]	A^2/C_d^2	C_d [pF]
Full diode	0.2500	$4.24 \cdot 10^{12}$	165.89	$4.70 \cdot 10^{-4}$	11.53
Half diode	0.0620	$4.49 \cdot 10^{12}$	167.75	$4.47 \cdot 10^{-4}$	2.96
Quarter diode	0.0156	$4.49 \cdot 10^{12}$	175.05	$4.57 \cdot 10^{-4}$	0.73
Circular diode	0.0176	$4.49 \cdot 10^{12}$	172.44	$4.52 \cdot 10^{-4}$	0.83

Table 4.4: *Serial Number 29 Experimental Results*

All 3 samples show good characteristics. The depletion capacitance is the same for the the three different samples. The SN29 which the sample with the p -spray isolation shows a bit higher value in the depletion Voltage.According to the electrical specifications of the CMS for the phase II upgrade which can be seen in table 3.19 the depletion voltage should be $V_d < 300$. At is it can be seen from the tables 4.2 , 4.3 , 4.4 the measurements are in accordance with the specifications.

Current-Voltage Measurements

The Current over voltage for all four diodes of the three test structures SN21 , SN22 , SN29 was measured. The Voltage was rumped up from 0 to 700 V with 5 V step. The measurements were performed at 23 ^oC. The guard ring of the diodes was kept floating for the diodes of $SN21$, $SN22$ while for the diodes of $SN29$ was kept grounded.

All 3 samples show ground characteristics concerning the current. The Full diode which has the biggest surface has the highest current. All 4 diodes of the three samples does not saturate above the full depletion voltage which is between (160-180V). This is due to the contribution of trap assisted tunneling to the current. The reduced thickness result in an electric field high enough that the current that is formed by tunneling effect from the conduction to the valence band is significant. The traps present due to imperfections enhance tunneling.

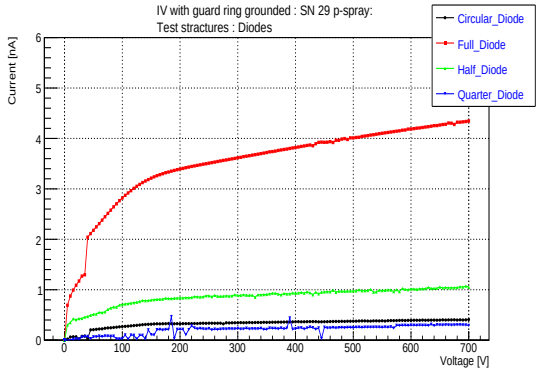

(α′) *Leakage Current of diodes Full , Quarter Half and Circular of* $SN29$ *chip* 15

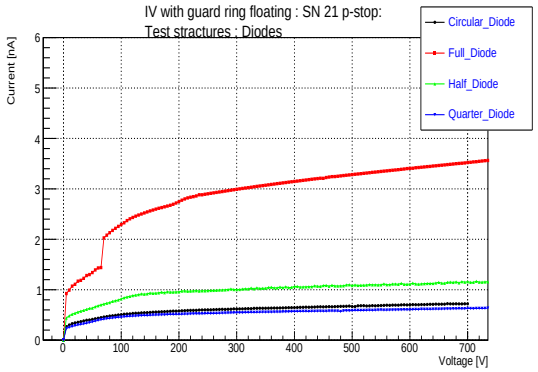

(β′) *Leakage Current of diodes Full , Quarter Half and Circular of* $SN21$ *chip* 15

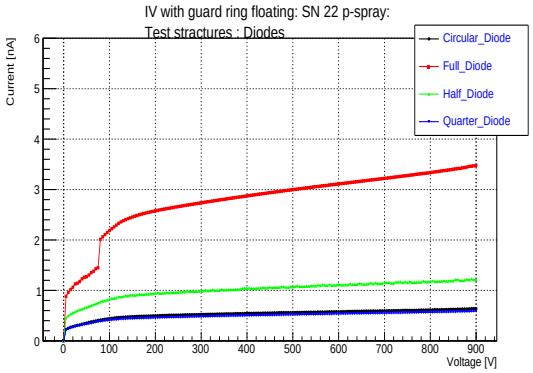

(γ′) *Leakage Current of diodes Full , Quarter Half and Circular of* $SN22$ *chip* 15

According to the electrical specifications of table 3.19 the leakage current should be $I_L < 2$ nA/mm^3 at 500 V. As it can be noticed from 4.5 the measurements are in accordance with the specifications.

Diode Name	I_L $[nA/mm^3]$		
	SN29	SN21	SN22
Full diode	0.50	0.41	0.38
Half diode	0.49	0.55	0.54
Quarter diode	0.49	1.18	1.03
Circular diode	0.67	1.18	1.00

Table 4.5: *Leakage Current at 500 V for all 4 diodes of test structures set* $SN21$ $SN22$ $SN29$

4.4.2 MOS

The MOS test structure is shown in Figure 4.15. The MOS capacitor is a very useful test device,it is the simplest test structure and still delivers extensive information. CV test results offer a wealth of device and process information, including bulk and interface charges. Many MOS device parameters, such as oxide thickness, flatband voltage, threshold Voltage, etc., can also be extracted from the CV data.

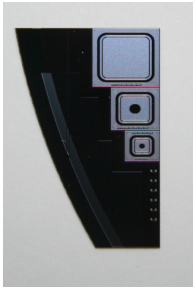

(α′) *Actual photo of the whole Test Structure set which contains an MOS and two Diodes*

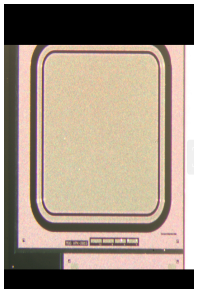

(β′) *Actual close Photo of the MOS*

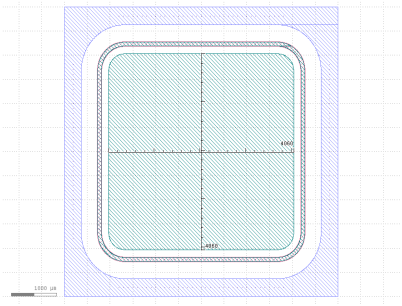

(γ′) *Schematic picture of the MOS structure as it is shown from KLayout program (GDS viewer)*

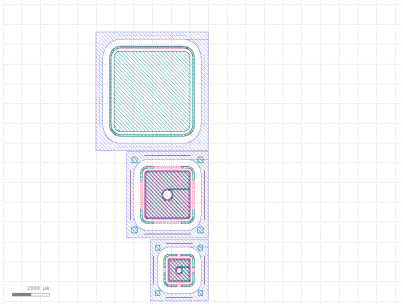

(δ′) *Schematic picture of the whole Test structure set as it is shown from KLayout program (GDS viewer)*

Figure 4.15: *MOS Test stracture*

The MOS test stractures that have been delivered and tested at NCSR demokritos are (as in the case of the diodes) the $SN21$ and $SN22$ with p -stop isolation technique and the $SN29$ with the p -spray isolation technique.

The CV measeruments on the MOS capacitors are made by applying the Lpot/Lcur at the backplane and the Hpot/Hcur at the gate.

The CV and the $1/C^2$ vs Voltage curves of the MOS capacitors are shown in figures 4.17α′ and 4.17β′. The measurements were performed at high frequency of $10\ MHz$. The MOS structure passes throw the 4 different stages described in section 1.6.2.

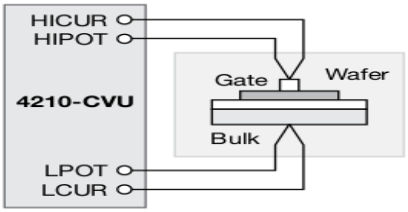

Figure 4.16: *Schematic of MOS Capacitance measurements*

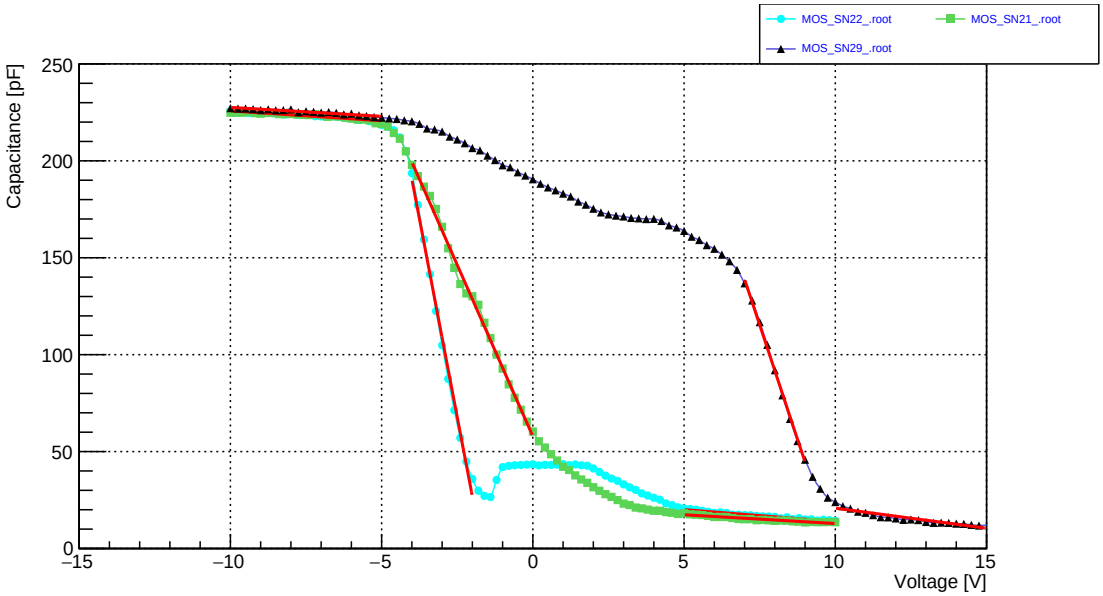

(α′) *CV curves of $SN21$, $SN22$ and $SN29$ MOS test-structures.*

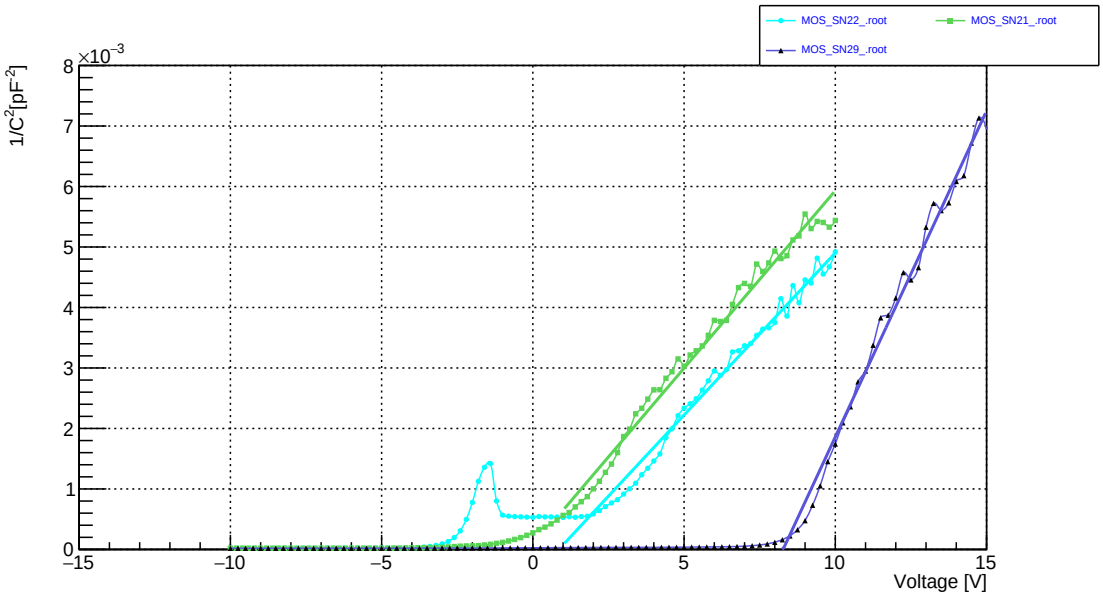

(β′) *$1/C^2$ vs Voltage. MOS test structures*

Extracting MOS Device Parameters From CV Measurements

This section describes the device parameters that are extracted from the CV taken in the three different test MOS structures.

***Oxide Capacitance* -Oxide Thickness**

The oxide capacitance (C_{OX}) is the high frequency capacitance when the device is biased for strong accumulation. In the strong accumulation region, the MOS acts like a parallel plate capacitor, and the oxide thickness (T_{OX}) may be calculated from C_{OX} and the gate area using the following equation.

$$T_{OX} = \frac{A\varepsilon_{\mathrm{OX}}}{C_{OX}} \tag{4.1}$$

where T_{OX} is the oxide thickness, C_{OX} is the oxide capacitance and ε_{OX} is the electrical permittivity of the silicon dioxide.

Flat Band Capacitance-Flat Band Voltage

The Flat Band Voltage V_{FB} can be identified by the CV curve. One way is to use the flatband capacitance method. For this method, the ideal value of the flatband capacitance (C_{FB}) is calculated from the oxide capacitance and the Debye length. Once the value of C_{FB} is known, the value of V_{FB} can be obtained from the CV curve.

The flat band voltage of real MOS structures is further affected by the presence of charge in the oxide or at the oxide -semiconductor interface. The flat band voltage corresponds to the voltage which when applied to the gate electrode yields a flat energy band in the semiconductor. The charge in the oxide or at the interface changes affect the flatband voltage. The measurement of the flat band Voltage can give information for the quality of the oxide. A low value indicates a low contamination level The flat band Voltage marks the inflection of the CV curve [11] .

The flatband Capacitance is calculated as follows:

$$C_{FB} = \frac{C_{OX}\varepsilon_{Si}A/\lambda}{C_{OX} + \varepsilon_{Si}A/\lambda} \tag{4.2}$$

where:

- A is the MOS surface
- λ is the extrinsic Debye length, which is calculated as follows:

$$\lambda = \sqrt{\frac{\varepsilon_{Si}kT}{q^2N}} \tag{4.3}$$

- $N = N_A$ or $N = N_D$ is the doping concentration

In semiconductors, majority carriers can move freely. Any electrical interaction has a limited range. The Debye length is used to represent this interaction range. Essentially, the Debye length indicates how far an electrical event can be sensed within a semiconductor.

Threshold Voltage

The threshold voltage (V_{TH}) is the point on the CV curve where the surface potential equals twice the bulk potential. This curve point corresponds to the beginning of strong inversion.

The threshold voltage of a MOS capacitor can be calculated as follows:

$$V_{TH} = V_{FB} \pm \left[\frac{A}{C_{OX}} \sqrt{4\varepsilon_{si} q |N_{Bulk} \varphi_{\mathrm{B}}|} + 2|\varphi_{\mathrm{B}}| \right] \tag{4.4}$$

where:

- φ_{B} is the bulk potential which can be calculated as:

$$\varphi_{\mathrm{B}} = -\frac{kT}{q} ln(\frac{N_{Bulck}}{N_i})(\pm 1) \tag{4.5}$$

- N_{Bulk} is the bulk doping
- N_i the intrinsic concentration
- $+$ is for p -type substrate and $-$ is for n type for both equations 4.4,4.5.

***Metal* -semiconductor work function difference**

The work function represents the difference in work necessary to remove an electron from the gate and from the substrate. It contributes to the shift in V_{FB} from the ideal zero value, along with the effective oxide charge [1]. The work function silicon -dioxide and aluminum is derived as follows:

$$W_{MS} = W_M - [W_s + \frac{E_{BG}}{2} - \varphi_{\mathrm{B}}] \tag{4.6}$$

where:

- WM is the metal work function
- W_{Si} is the substrate material work function.
- E_{BG} is the energy band gap.

And for the silicon -dioxide and aluminum equation 4.6 it is simplified at:

$$W_{MS} = 0.61 + \varphi_{\mathrm{B}} \tag{4.7}$$

Effective and total bulk oxide charge

The effective oxide charge (Q_{EFF}) represents the sum of oxide fixed charge (Q_F), mobile ionic charge (Q_M), and oxide trapped charge (Q_{OT}).

$$Q_{EFF} = Q_F + Q_M + Q_{OT} \tag{4.8}$$

The effective oxide charge can be calculated from 4.9 as defined at [56]:

$$V_{FB} - W_{MS} = -\frac{Q_{EFF}}{C_{ox}} \tag{4.9}$$

Substrate Doping Concentration

The substrate doping concentration (N) is related to the the slope of the $1/C^2$ vs V curve 4.17β′. The doping concentration is calculated from the function:

$$N_{sub} = |\frac{2}{q\varepsilon_{si}A^2\frac{\Delta(1/C^2)}{\Delta V}}| \tag{4.10}$$

The above parameters for the three different MOS test -structures have been measured using the CV curves of 4.17α′ and 4.17β′. The results have been summarized in table 4.6.

MOS CV 10 kHz	SN21	SN22	SN29
Accumulation Capacitance (C_{ox})	$220.255 \pm 0.817 \quad [pF]$	$219.786 \pm 0.765 \quad [pF]$	$213.349 \pm 0.633 \quad [pF]$
Oxide Layer Thickness (T_{ox})	$(258.345 \pm 0.958) \cdot 10^{-6} \quad [cm]$	$(258.896 \pm 0.901) \cdot 10^{-6} \quad [cm]$	$(266.707 \pm 0.791) \cdot 10^{-6} \quad [cm]$
Flatband Capacitance (C_{FB})	$137.29 \pm 0.32 \quad [pF]$	$139.416 \pm 0.31 \quad [pF]$	$118.972 \pm 0.197 \quad [pF]$
Flatband Voltage (V_{FB})	$-2.245 \pm 0.009 \quad [V]$	$-3.375 \pm 0.004 \quad [V]$	$7.423 \pm 0.004 \quad [V]$
Threshold Voltage (V_{TH})	$-1.873 \pm 0.009 \quad [V]$	$-2.989 \pm 0.004 \quad [V]$	$7.713 \pm 0.004 \quad [V]$
Bulk Potential (φ_{bi})	$-0.101568 \quad [V]$	$-0.103877 \quad [V]$	$-0.0859732 \quad [V]$
Metal Semiconductor Work function (W_{MS})	$-0.711568 \quad [V]$	$-0.713877 \quad [V]$	$-0.695973 \quad [V]$
Effective oxide charge (Q_{eff})	$2049.06 \pm 7.60 [pFV]$	$3548.82 \pm 12.35 \quad [pFV]$	$-10508.20 \pm 31.16 \quad [pFV]$
Substrate Doping (N_{sub})	$7.60023 \cdot 10^{11} \quad [cm^{-3}]$	$8.3163 \cdot 10^{11} \quad [cm^{-3}]$	$4.13833 \cdot 10^{11} \quad [cm^{-3}]$
Depletion Depth	$73.157 \quad [\mu m]$	$51.38 [\mu m]$	$69.69 \quad [\mu m]$
Debye Length (λ_D)	$0.00465824 \quad [cm]$	$0.00445318 [cm]$	$0.000631281 \quad [cm]$

Table 4.6: MOS Results

From the 3 structures the MOS $SN29$ has higher Flat -band Voltage and Flat -band Capacitance, and also it has the highest Effective Oxide charge.

4.4.3 Baby Sensors

These are sensors with identical parameters with the 2S sensors but with reduced number of strips. They are used to investigate the sensor properties before and after irradiation. The initial characterization is done in the probe-station, where all important sensor parameters as the total current and the full depletion voltage are measured as well as strip parameters such as coupling capacitance, inter -strip capacitance, bias resistors, inter -strip resistance and strip currents. Those parameters of three baby -sensors where calculated and characterized. These sensors are *chip 6*, *Serial number 29* with p -spray isolation technique and *chip 6*, *Serial number 21,22* with p -stop technique.

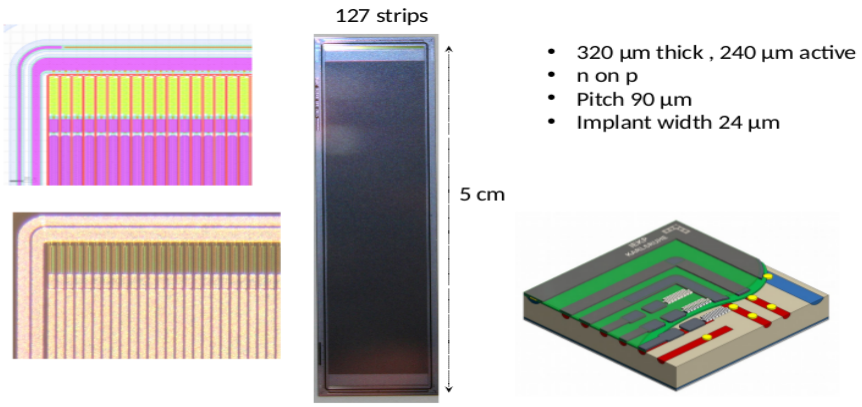

Figure 4.18: *Baby sensors is one set of the many mini sensors that have been built in the wafer for characterization proposes.*

Total Leakage Current

The total leakage current for the 3 baby sensors was measured. The backplane is on high voltage and the guard ring is connected via the electrometer to the ground. The guard ring is not connected but in floating mode. The voltage is increased from $0 - 700$ V with a 5 V step. The measurements were performed at 23^oC.

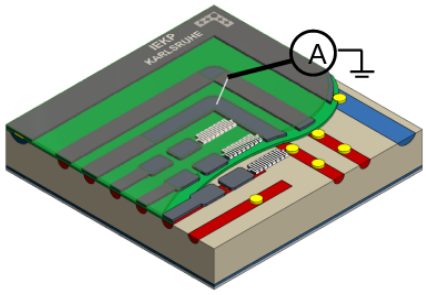

Figure 4.19: *Schematic of the setup for Total Current measurement*

The IV curves are shown in Figure 4.20. The total leakage current of $SN29$ with p -spray isolation technique exhibits an extremely high current. The leakage current of $SN21$ is slightly

higher that the $SN22$. None of the $SN21$ and $SN22$ exhibits an early breakdown. A schematic for measuring the total leakage current is shown in figure 4.19

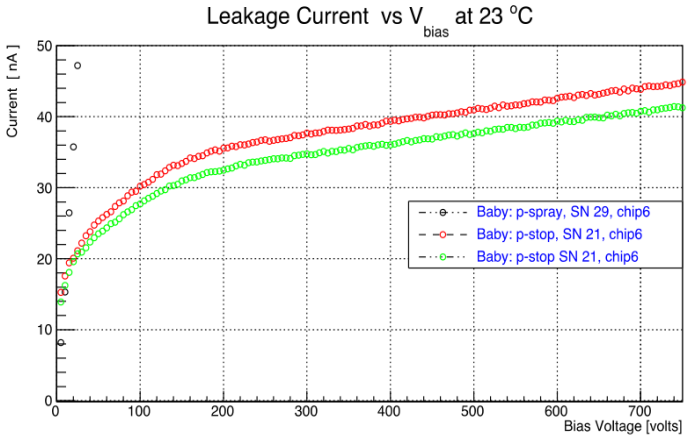

Figure 4.20: *Total Leakage Current for $SN21$,$SN22$,$SN29$ baby sensors.*

According to specifications which can be seen in table 3.19, the leakage current should be $I_L < 2\ nA/mm^3$ at 500 V. Sensors $SN21$ $SN22$ are in good conformity with the electrical specifications as it can be seen from table 4.7

	$I_L/mm^3\ [nAmm^{-3}]$
SN29	-
SN21	0.20
SN22	0.19

Table 4.7: *Leakage current per Volume at 500 V*

Backplane Capacitance

The backplane capacitance was measured for all 3 sensors by measuring the total capacitance between the bias ring and the backplane and dividing by 127 which is the total number of the strips. The backplane capacitance is measured at 1 kHz. A schematic of the setup for measuring the backplane capacitance is shown in 4.21.

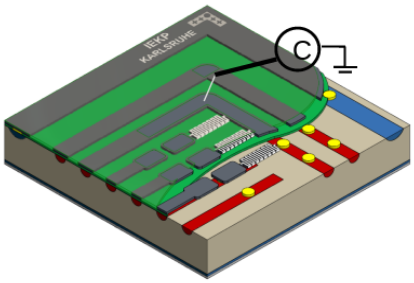

Figure 4.21: *Schematic of the setup for the Backplane Capacitance measurement*

In the following diagram the value of $1/C^2$ is plotted versus voltage. The capacitance is scaled with the surface of each strip.

With linear interpolation between the inclined part and the horizontal part of the graph and by calculating the interaction point of the two linear functions the depletion Voltage is calculated as well as the depletion capacitance. Also by the slope of the inclined part the substrate concentration is calculated. According to specifications $V_d < 300$ V.

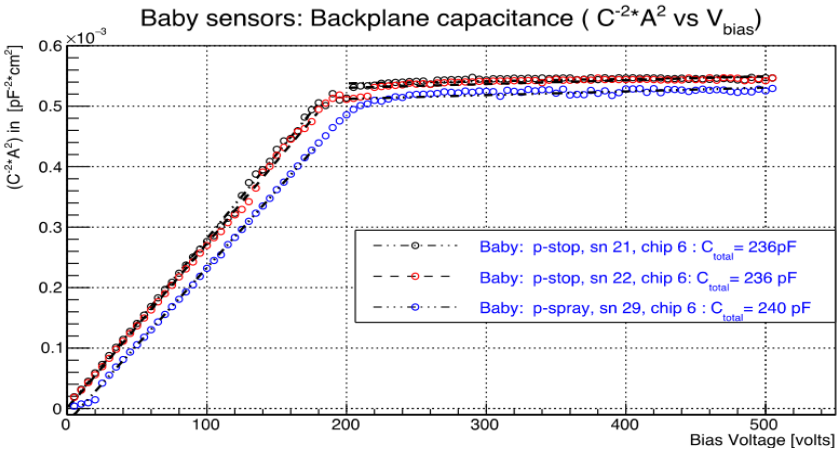

Figure 4.22: *Backplane Capacitance for Baby Sensors $SN21$,$SN22$,$SN29$*

	$N_d[cm^{-3}]$	$V_d[Volt]$	$C_{back}/strips[pF]$
SN29	4.65×10^{12}	209.25	1.89
SN21	4.25×10^{12}	191.21	1.86
SN22	4.36×10^{12}	194.21	1.86

Table 4.8: *Substrate concentration, Depletion Voltage, Backplane Capacitance*

The substrate concentration is very close to the substrate concentration of the diodes. This was expected because the diodes and the baby sensors are made on the same wafer.

The depletion voltage of the baby sensor is higher that the diodes which corresponds with 2.8

Inter -strip Capacitance

The inter -strip capacitance is measured between one strip and it's two neighbors at 1 MHz and as a function of the bias voltage. The measurement is very delicate, as even the position of the needles amongst each other influences the values.

A schematic for the measurement of the inter -strip capacitance is shown in 4.23. The bias ring is grounded. The measurement is performed between one central strip and two neighboring strips. The central strip is has been set to the low voltage and the two neighboring to the high voltage.

The measurements has been performed for the 3 three different baby sensors by taking 5 several areas of the sensors (5 triads of strips). This is because the automation of the system with

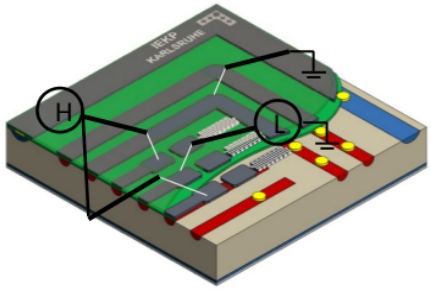

Figure 4.23: *Schematic of the setup for Interstrip Capacitance measurement*

simultaneous control of the probe station an the electrical characterization equipment was not yet developed. The graphs for each one sensor are shown in figures 4.24, 4.25 , 4.26. The graphs exhibit a sharp drop at low Voltages and most of them have a minimum between $0.5 - 3V$. After that minimum the Capacitance rises with the Voltage until it reaches the depletion Voltage where the capacitance remains stable. Figures 4.24 , 4.25 , 4.26 shows the internship capacitance between one central and two neighbor strips for sensors $SN21$, $SN22$, $SN29$.

The inter -strip capacitance should be small in order to permit a good charge sharing between the strips. All 3 sensors show a small and homogeneous inter -strip capacitance of about

$$C_{int} = 1.31 \quad [pF] = 0.27[pF/cm] \tag{4.11}$$

While according to specifications of table 3.19 $C_{int} < 1\ pF/cm$. The 3 sensors that were measured are in good conformity with the electrical specifications.

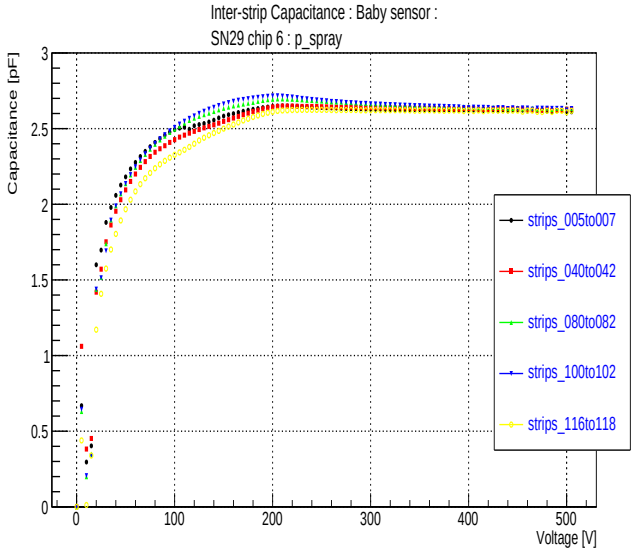

Figure 4.24: *Inter -strip Capacitance between one central strip and two neighbors over voltage for Baby sensor SN29*

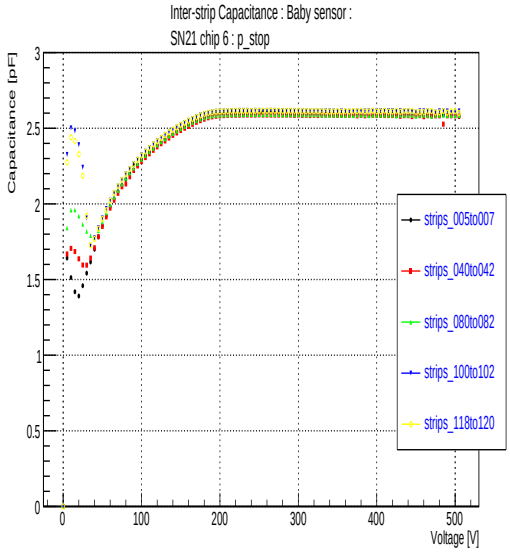

Figure 4.25: *Inter -strip Capacitance between one central strip and two neighbors over voltage for Baby sensor SN21*

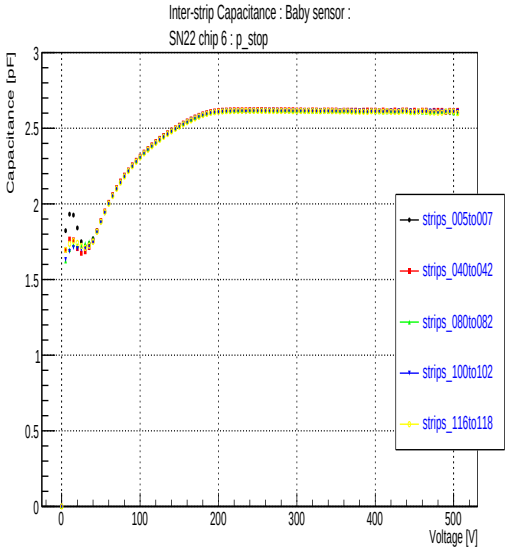

Figure 4.26: *Inter -strip Capacitance between one central strip and two neighbors over voltage for Baby sensor SN22*

Total Strip Capacitance

The total strip capacitance is the sum of the backplane capacitance of each strip and the inter -strip capacitance between the two neighbor strips.

The total strip capacitance for the 3 baby sensors was measured. In Figure 4.27 the schematic of the measurements is shown. The bias Voltage is applied to the backplane while the bias ring of the sensor is held to a ground potential. The capacitance is measured between one central strip and the ground.

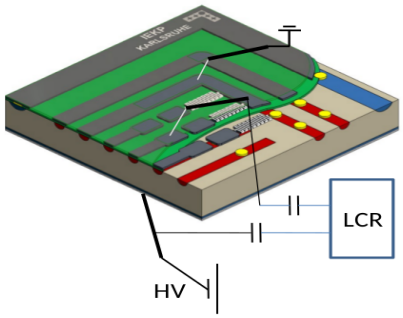

Figure 4.27: *Total Capacitance per single strip measurement setup*

In figures 4.28 , 4.29, 4.30 the CV of the total strip for the baby sensors $SN21$, $SN22$, $SN29$ are shown. The bias Voltage is increased from 0 to 500 Volt. The total capacitance drops with the voltage increase until the depletion is reached where it remains stable.

All 3 sensors show good homogeneous characteristics considering the total capacitance. Only one strip ($strip001$) show a lower capacitance in all three sensors which it was expected consid-

ering that this strip is located to the edge of the sensor and it has only one neighbor strip.

In Figure 4.31 the histograms of the total strip capacitances are shown for all 3 baby sensors. The mean values and the standard deviation of each histogram are shown in table 4.9:

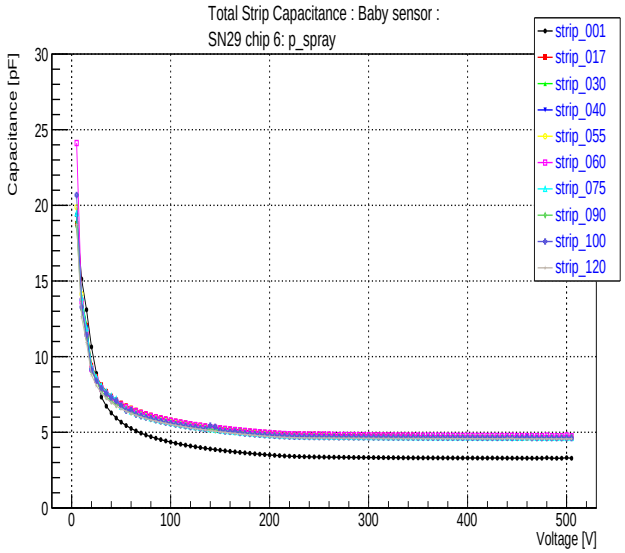

Figure 4.28: *Total Capacitance per single strip for $SN29$ p -spray sensor*

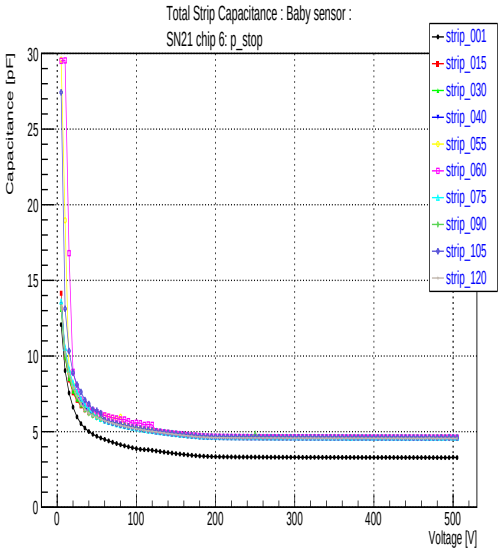

Figure 4.29: *Total Capacitance per single strip for $SN21$ p stop sensor.*

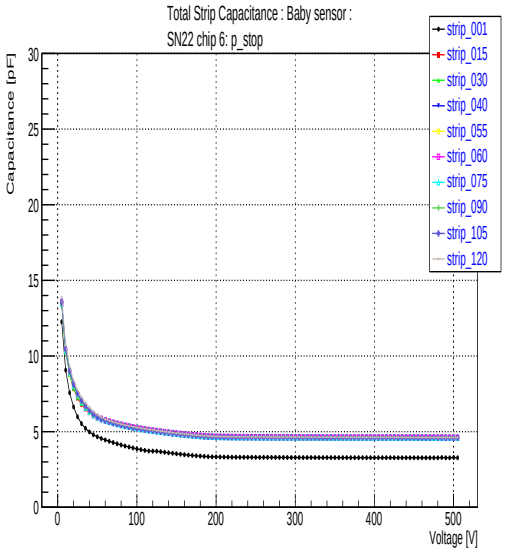

Figure 4.30: *Total Capacitance per single strip for $SN22$ p stop sensor*

This measurement does not coincide exactly with the data taking conditions. This is because in this measurement all other strips are floating while when amplifiers are connected the strips are grounded via the virtual ground of the amplifier inputs

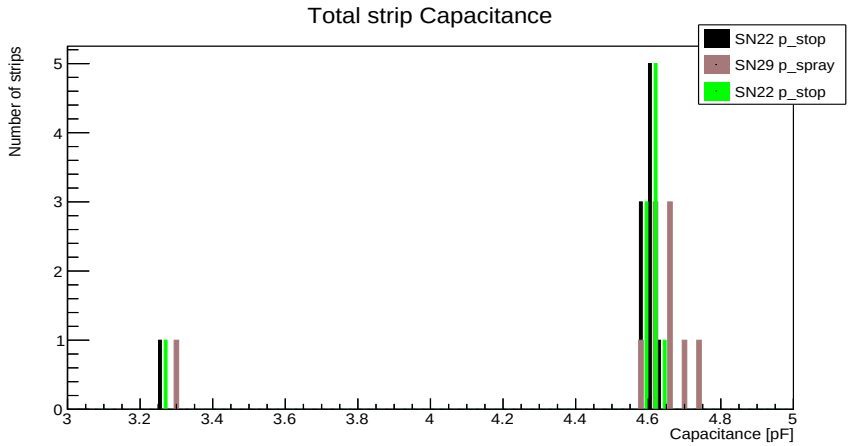

Figure 4.31: *Histogram of total Capacitance per single strip of all strips for the baby sensors $SN21$,$SN22$,$SN29$.*

	Average Total Capacitance per strip [pF]
SN29	4.64 ± 0.04
SN21	4.60 ± 0.02
SN22	4.60 ± 0.02

Table 4.9: *Mean Values of the Coupling Capacitances*

Coupling Capacitance

The coupling capacitance is measured by contacting the DC pad and the AC pad of each strip. In the CMS collaboration the measurement of the coupling capacitance (CC) is made with a measurement frequency of 1 kHz. The capacitance voltage characteristics (CV) measurements is not trivial because it is necessary to perform the measurements on low potential.

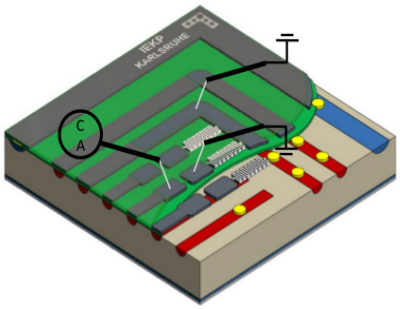

Figure 4.32: *Schematic of the setup for Coupling Capacitance measurement*

The requirements of coupling capacitance is to be homogeneous over the whole sensor and to be significantly higher than the inter -strip capacitance and the backplane. The signal is coupled out from the implant to the readout strip, where it is conducted to the readout chip. The coupling capacitance should be stable with each voltage variance.

The coupling capacitance for several different strips was measured for the 3 baby -sensors

$SN21$, $SN22$ and $SN29$. The CV plots of each sensor is shown in figures 4.33α′ , 4.33β′ , 4.33γ′.

All three sensors show a stable coupling capacitance for all the measured strips between 142 -144 [pF]. Only in one sensor SN29 p -spray one strip exceeds the average values and reaches the value of 165 [pF].

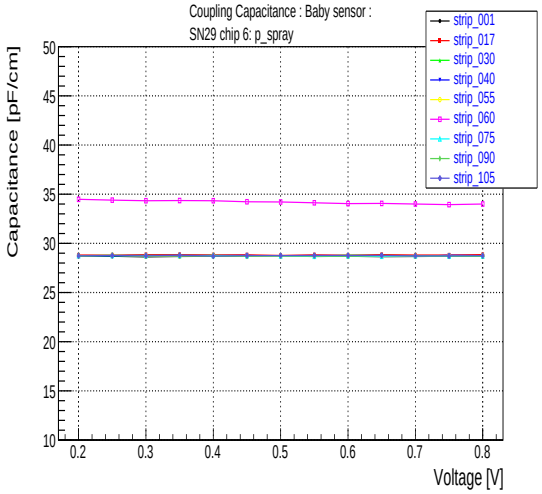

(α′) *Coupling Capacitance for $SN29$ p -spray sensor*

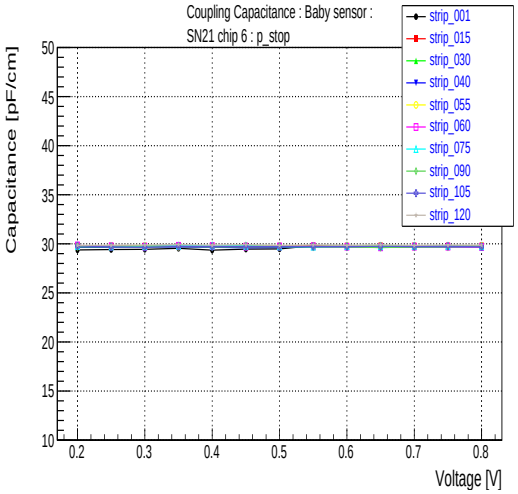

(β′) *Coupling Capacitance SN21 p -stop sensor.*

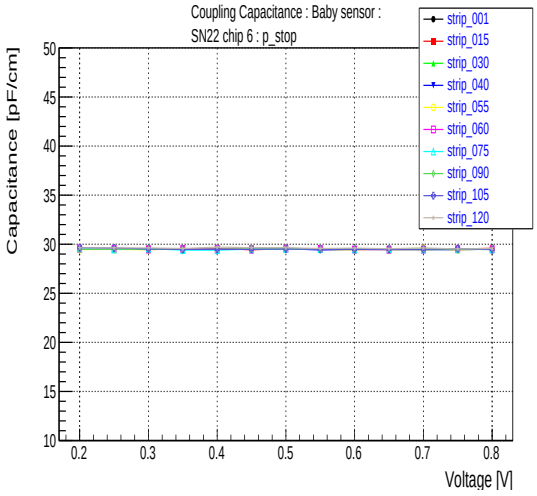

(γ′) *Coupling Capacitance SN22 p -stop sensor*

By taking the average values of each strip the below histograms are derived for each sensor Figure 4.34. The mean values for each histogram and the standard deviation are shown in table 4.10. While according to specifications $C_{ac} > 1.2\ [pF/cm]$. As it can be seen from table 4.10 the coupling capacitance of the three sensors that was measured is in conformity with the specifications. .

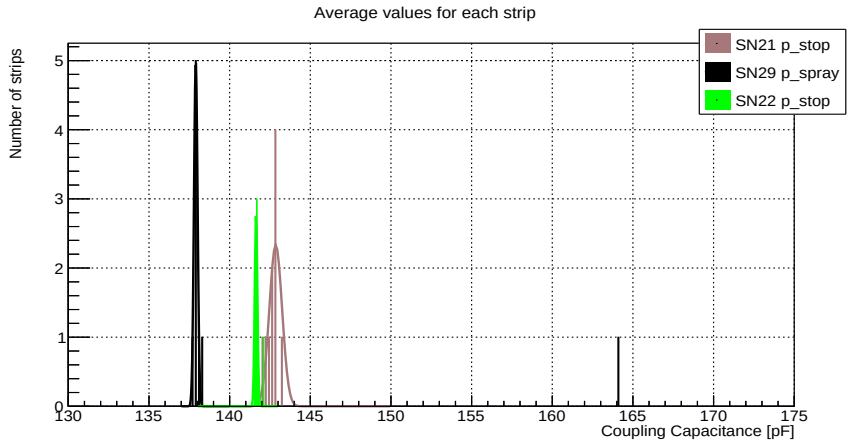

Figure 4.34: *Histogram of the average values of the Coupling Capacitance for each strips for the sensors $SN21$, $SN22$, $SN29$.*

	Coupling Capacitance [pF]	Coupling Capacitance [pF/cm]
SN29	137.90 ± 0.11	28.7 ± 0.02
SN21	142.86 ± 0.39	30.0 ± 0.08
SN22	141.63 ± 0.08	29.5 ± 0.02

Table 4.10: *Mean Values of the Coupling Capacitances*

Comparison of experimental values with numerical calculations

In this section a comparison is made between the experimental values of the baby sensors and numerical calculations. The numerical calculation is made by a program that solves the 3D Laplace equation for silicon sensors with strip geometry. For more details about the method of the calculations and the program can be found in [54], [55].

	$SN21$	$SN22$	$SN29$	Calculated
Backplane Strip Capacitance [pF]	1.86	1.86	1.89	1.85
Inter-strip Capacitance (first neighbor) [pF]	1.31	1.31	1.31	1.32

Table 4.11: *Comparison of experimental values and calculated values.*

Poly -Silicon Bias Resistor

To measure the Bias resistance a defined Voltage V_{set} is applied over the bias resistor and the current is measured I_{meas}. The bias ring is kept grounded and the Voltage is applied to the DC pads of several strips.

The bias resistance is then calculated by $R_{bias} = V_{set}/I_{meas}$. By making the Current over Voltage graph and calculating the slope of each graph the R_{bias} is calculated as it will be the inverse of the slope. Applying too high voltage may disturb the field, lowering the inter-strip resistance and thus result too low measured R_{bias}. The applying voltage is set between $0 - 2V$. In figures 4.36, 4.37, 4.38 the graphs of Current versus voltage are shown for calculating the R_{bias}

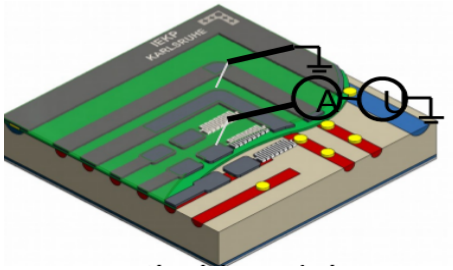

Figure 4.35: *Schematic of the setup for Bias Resistor Measurements*

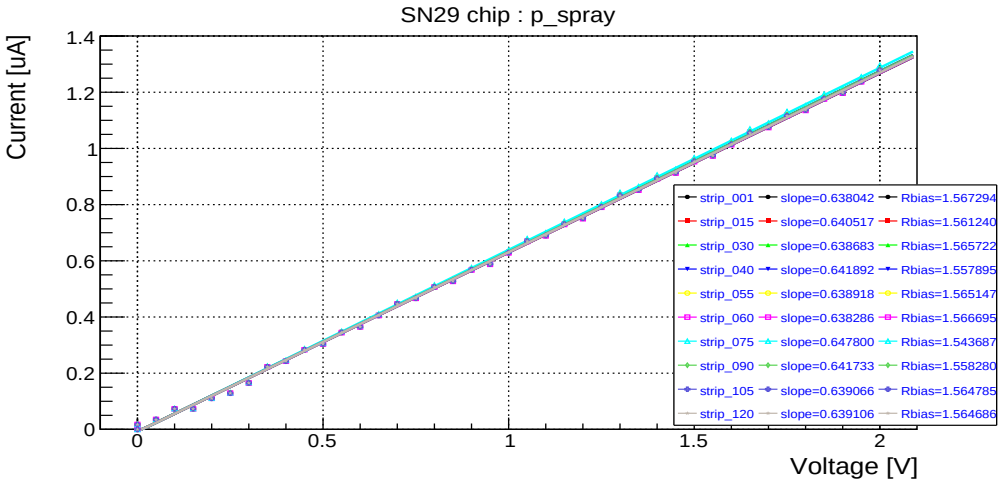

Figure 4.36: *IV measurement sensor 29 between several strips and*

From table 4.12 we can notice that the measurements of R_{bias} for the Baby sensors $SN29$, $SN21$, $SN22$ approximate the electrical specifications for the R_{bias} which give $Rbias = 1.5 \pm 0.3\ M\Omega$. Also we can notice that the Baby sensor with the p -spray isolation technique $SN29$ has the smallest deviation considering the other two sensors $SN21$ and $SN22$ which have a p -stop isoloation technique.

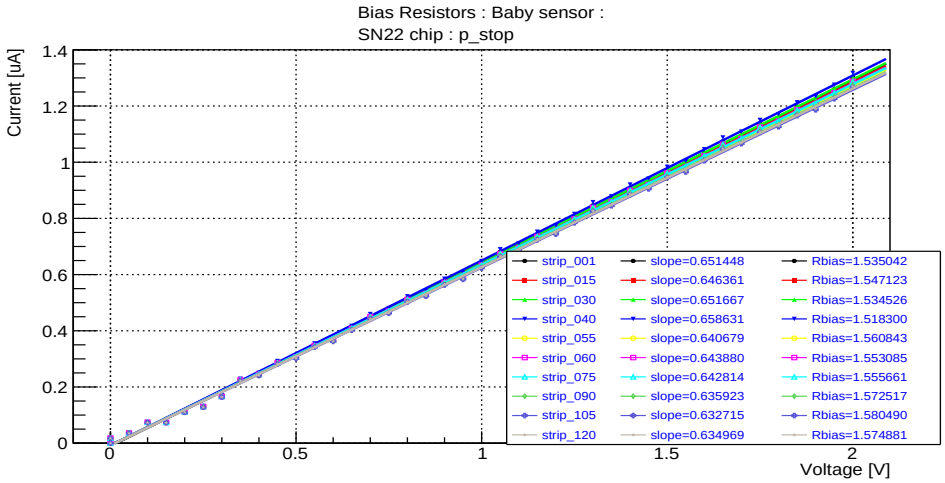

Figure 4.37: *IV measurement sensor 22 between several strips and*

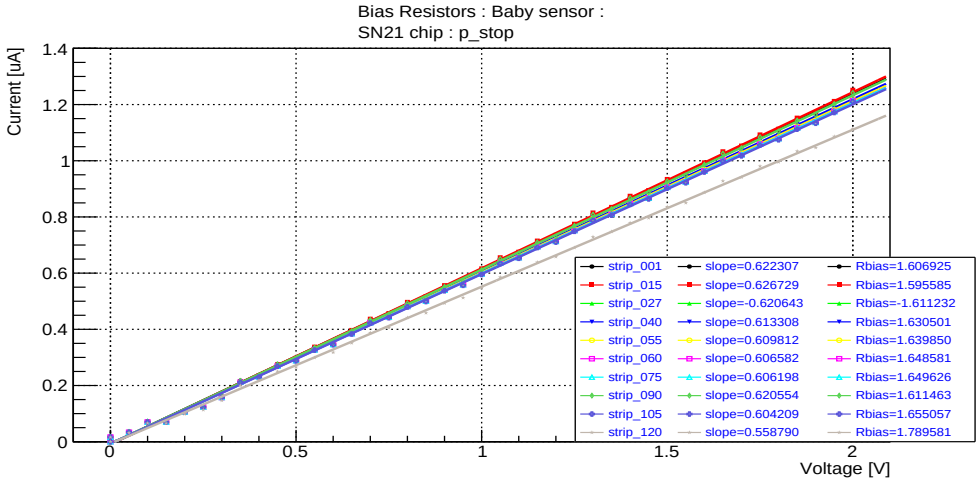

Figure 4.38: *IV measurement sensor 21 between several strips and*

	$R_{bias}\ [Mohm] SN29$	$R_{bias}\ [Mohm] SN21$	$R_{bias}\ [Mohm] SN22$
strip 1	1.567	1.535	1.607
strip 15	1.561	1.547	1.596
strip 30	1.566	1.535	1.611
strip 40	1.558	1.518	1.630
strip 55	1.565	1.561	1.640
strip 60	1.567	1.553	1.649
strip 75	1.544	1.556	1.650
strip 90	1.558	1.572	1.611
strip 105	1.565	1.580	1.655
strip 120	1.565	1.575	1.790
Average value	1.561 ± 0.007	1.553 ± 0.019	1.644 ± 0.053

Table 4.12: *SN21 , SN22 ,SN29 Experimental Results*

4.5 Electrical characterization on PS -p light sensors

The PS -module consists of a macro -pixel sensor (PS -p) and a strip sensor (PS -s) of n in p -bulk substrate. As mentioned in 3.5.2 the PS -p is a DC -coupled sensor of approximately 5×10 cm^2 with 32 rows of macro-pixels. The macro -pixels are 1.5 mm long with 100 µm pitch and an implant width of 25 µm which leads to a 0.25 width to pitch ratio.

For testing purposes a smaller prototype sensor was made. The PS -p light sensor has 6 rows of 48 columns which lead to 288 macro-pixels with the same aspect ratio as the foreseen PS -p sensor 4.40α′. The design was made by CMS and several wafers with p -stop and p -spray isolation were produced. Each wafer contains several PS -p light sensors. They are manufactured on p -type float -zone (FZ) silicon of 4 -inch wafers with a thickness of 200 µm and a resistivity between $4 - 8$ $k\Omega cm$ on a DC -process Figure 4.39.

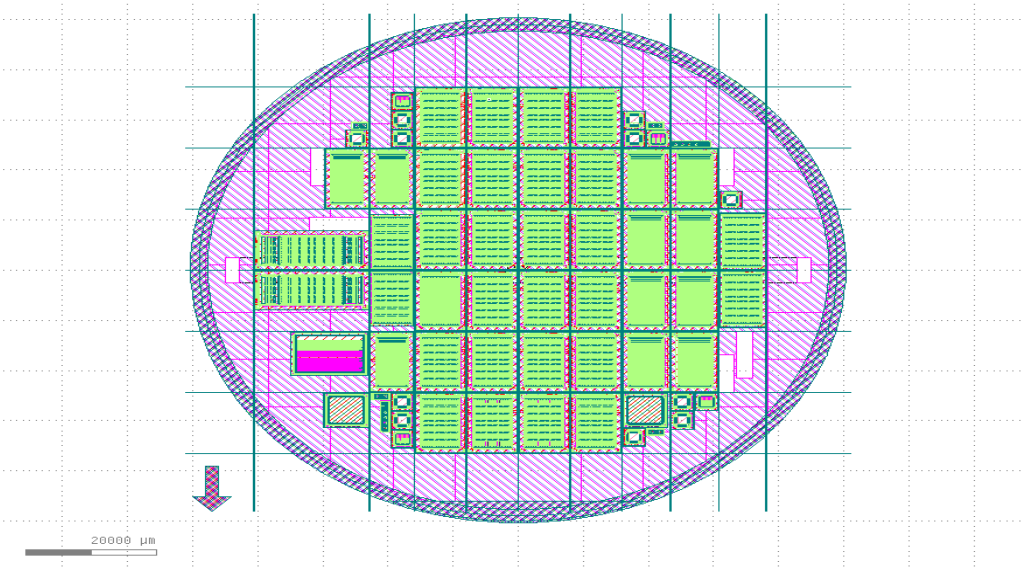

Figure 4.39: *PS -p light wafer as it can be shown in the KLayout (GDS viwer).*

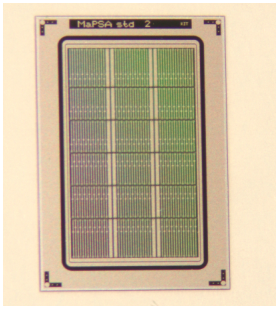

(α′) *PS -p light sensor.*

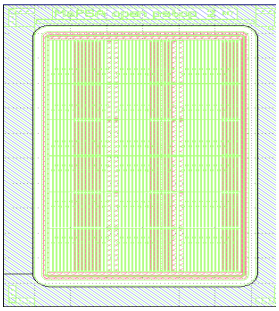

(β′) *PS -p light sensor (KLayout)*

Several PS -p light sensors were sent and tested. The measurements that were contacted are the Total current, Backplane Capacitance and IV -macropixel scans.

Backplane Capacitance

The backplane Capacitance for the 4 PS -p light sensors was measured. The results are shown in Figure 4.41

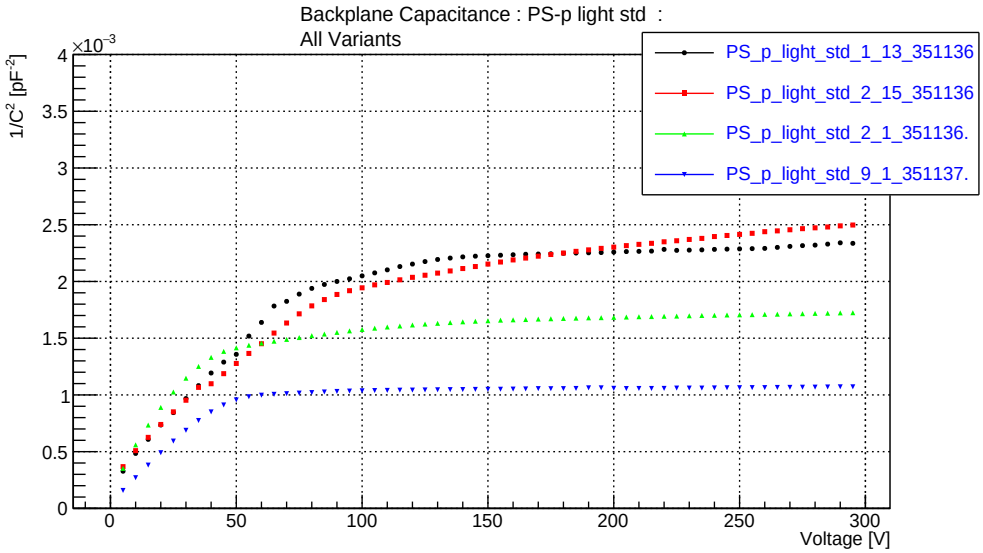

Figure 4.41: *Backplane Capacitance for all 4 Variants*

The Backplane Capacitance std_1_13 and std_2_15 have a depletion Voltage at about $100V$ while the other two std_2_1 and std_9_1 have a depletion Voltage of about $80V$. Sample std_9_1 exhibits the lowest Capacitance.

Total Current

The total current was measured by connecting the backplane on low voltage and the bias ring is connected via the electro meter to the high voltage In Figure 4.42 the measurement setup of the total current is shown.

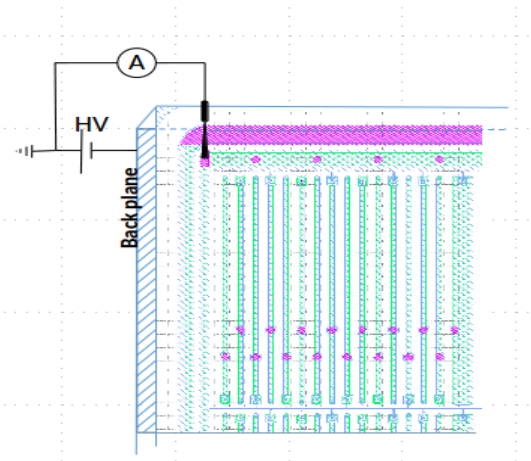

Figure 4.42: *Schematics of IV measurement*

In Figure 4.43 the total Current versus Voltage is shown for the 4 PS -p light sensors.

From the graph it can be shown that the sensors $std\_2\_1\_351136$ and the $std\_9\_1\_351136$ show similar characteristics and break-throw voltage at approximately 250 V.

The sensor $std\_9\_13\_351136$ has the earliest break -throw Voltage at 160 V while the $std\_2\_15\_351136$ show a breakdown voltage at 380 V. According to the electrical specifications 3.19 the breakdown voltage should be $V_{break} > 700\ V$. The measurements differ significantly from the specifications something that implies defects of the three sensors that have been tested.

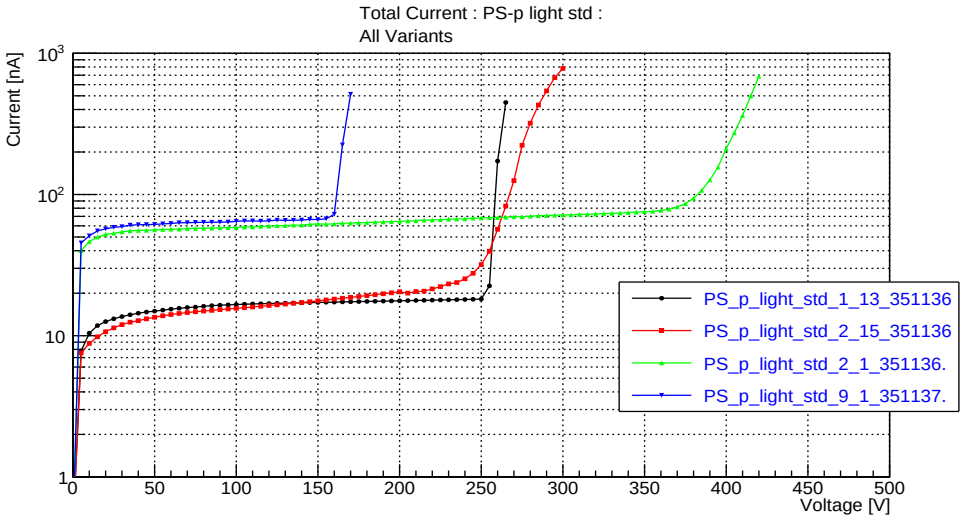

Figure 4.43: *Total Current for all 4 Variants*

4.5.1 IV macropixel -scans

The pixel currents were measured and optical inspection was done to investigate defective pixels.

The sensor is biased with high voltage which is applied to the bias ring while the backplane is connected to low potential. The strip leakage currents are measured by connecting the DC pads with the electro meter. A schematic of the measurement setup for IV strip scan is shown in Figure 4.44

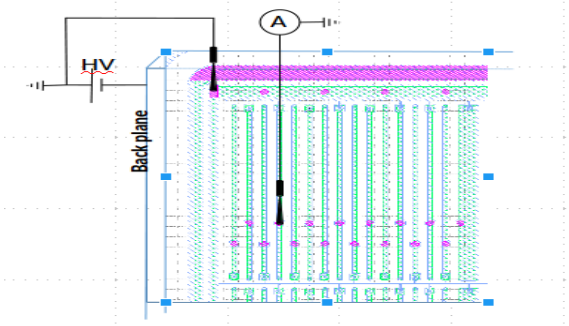

Figure 4.44: *Schematic of single macropixel leakage current measurement*

*PS_p_light_std*_2_1_351136 (Variant 1)

The Current for several macro-pixels was measured with the Voltage increasing from $0-350$ V. The IV for each macro-pixel that was measured is shown in Figure 4.45. Figure 4.46 shows a colored matrix with the cells representing the position of each macro-pixel on the sensor for fixed voltage at 200 V and 4.47 shows a matrix with the actual current values at 200 V.

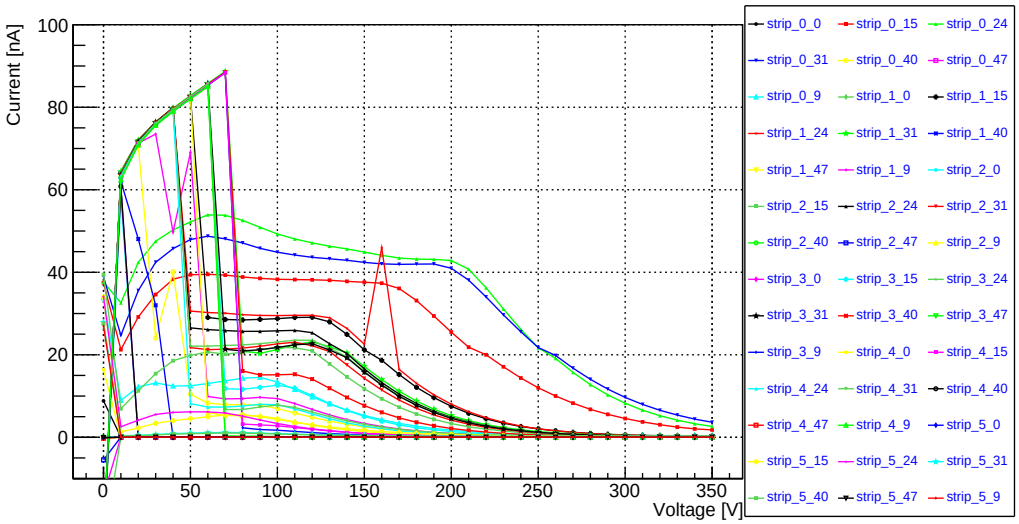

Figure 4.45: *IV strip scan for sensor* $PS\_p\_light\_std\_2\_1\_351136$.

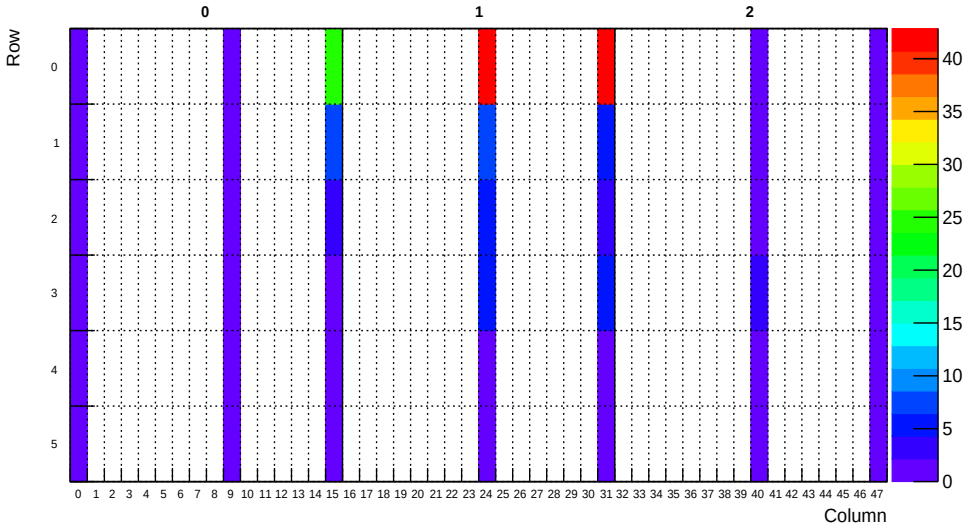

Figure 4.46: *Colored matrix of Current with fixed Voltage at* 200 *V each cell represents the position of the macro-pixel on the sensor* $PS\_p\_light\_std\_2\_1\_351136$.

From Figure 4.46 it can be shown that the current is low for most of the strips at 200 V. The strips in the middle give a higher current. Three strips strip-0-15 , strip-0-24 ,strip-0-31 give extremely high current compared to the others at $200V$. This could be the result of a defect in

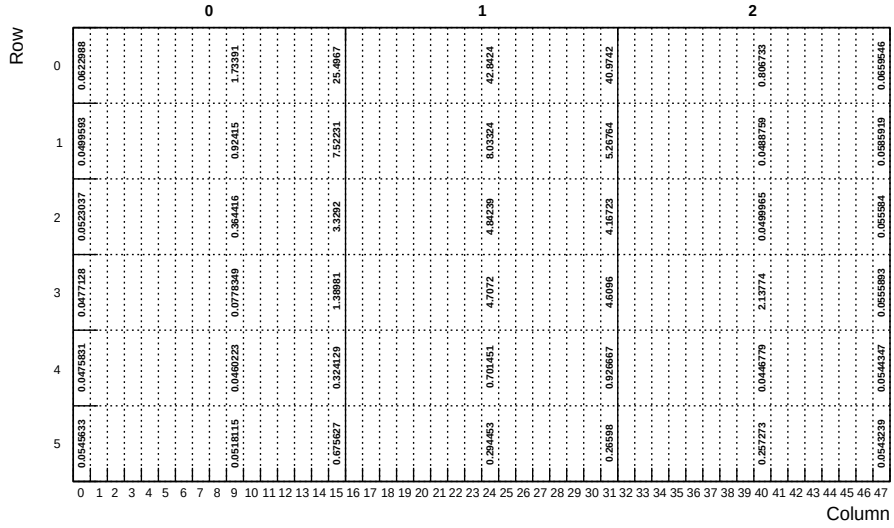

Figure 4.47: *Matrix of Current with fixed Voltage at* 200 *V each cell represents the position of the macro-pixel on the sensor.*$PS\_p\_light\_std\_2\_1\_351136$.

these macro -pixels.

$PS\_p\_light\_std\_1\_13\_351136$ (Variant 2).

In the same way the 3 other PS-p light sensors are characterized. In Figure 4.48 we can see the IV curve for all the strips that was measured. Some of them give an extremely high current at low Voltage between $0-50$ and after that it stabilizes at very low values for most of the strips.

Figure 4.49 again shows a colored matrix at 200 V. Most of them have very low current with the maximum at 0.012 nA

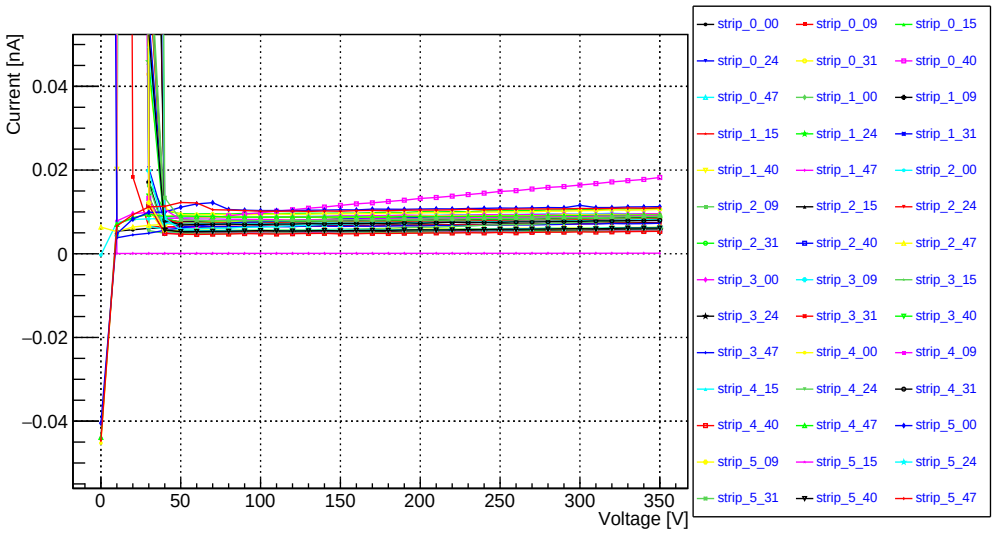

Figure 4.48: *IV strip scan for sensor* $PS\_p\_light\_std\_1\_13\_351136$.

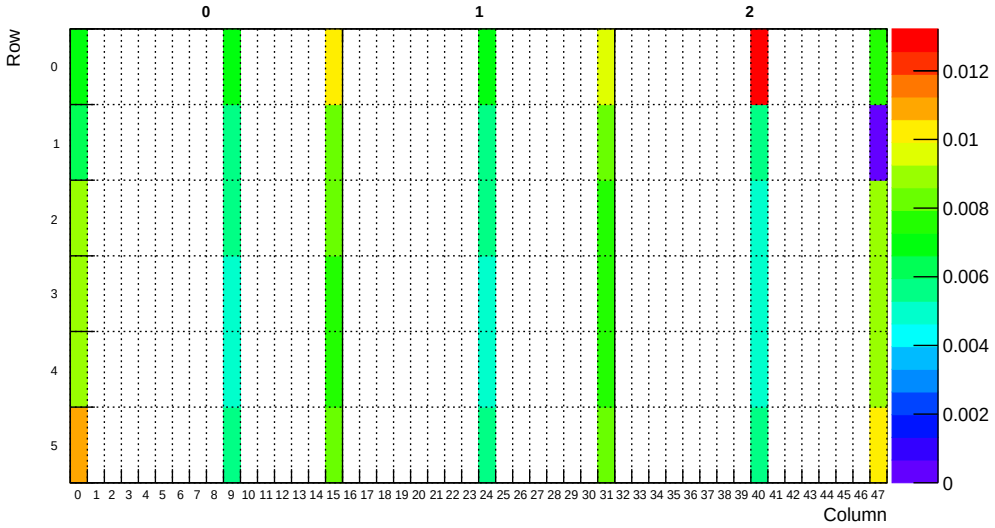

Figure 4.49: *Colored matrix of Current with fixed Voltage at* 200 *V each cell represents the position of the macro-pixel on the sensor* $PS\_p\_light\_std\_1\_13\_351136$.

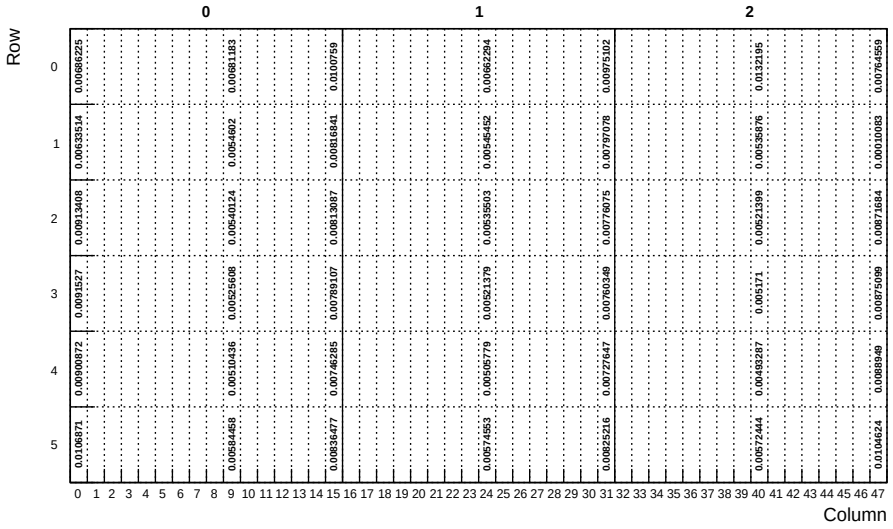

Figure 4.50: *Current matrix with fixed Voltage at* 200 *V each cell represents the position of the macro-pixel on the sensor* $PS\_p\_light\_std\_1\_13\_351136$.

*PS_p_light_std*_2_15_351136 (Variant 3)

The Current for several macro-pixels was measured with the Voltage increasing from $0-350$ V. The IV for each macro-pixel that was measured is shown in Figure 4.51.

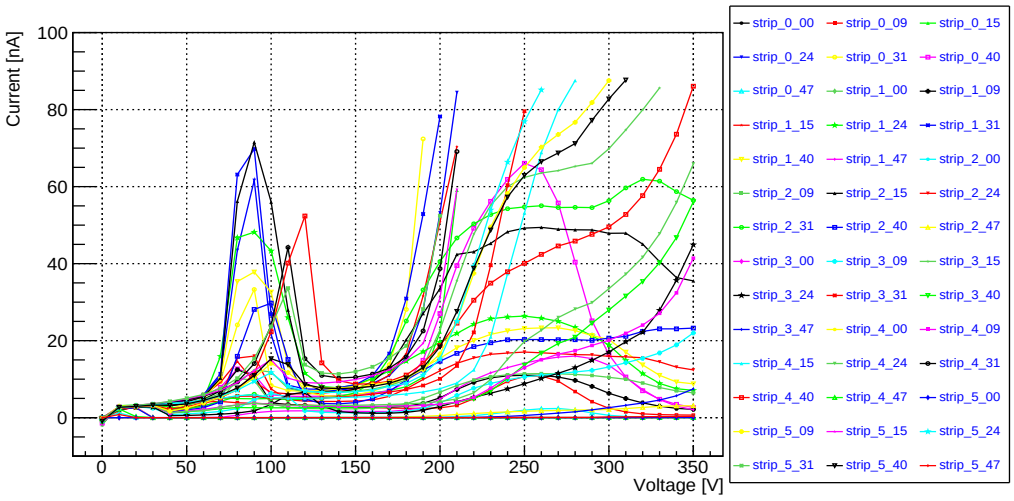

Figure 4.51: *IV strip scan for sensor PS_p_light_std*_2_15_351136.

Figure 4.52 shows a colored matrix with the cells representing the position of each macro-pixel on the sensor for fixed voltage at 200 V and 4.53 shows a matrix with current values for 200 V.

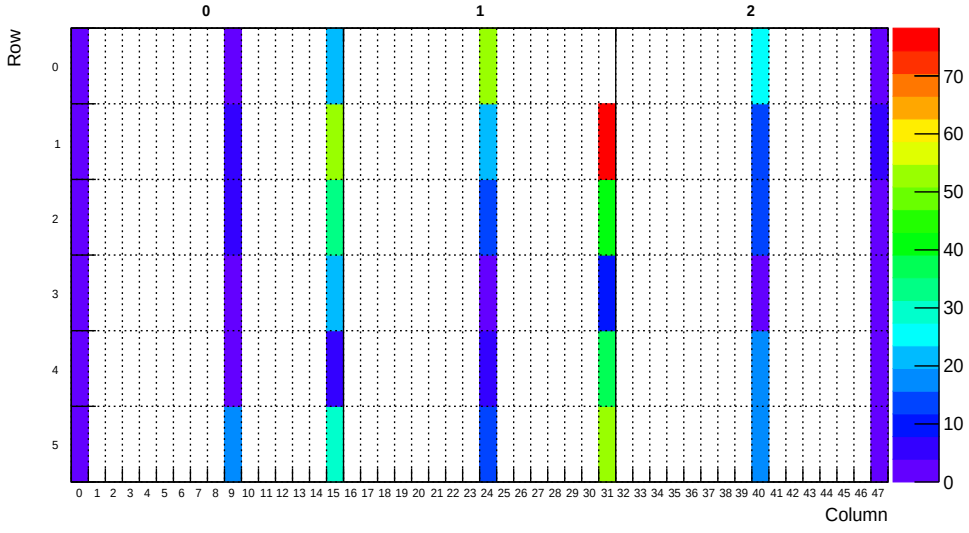

Figure 4.52: *Colored matrix of Current with fixed Voltage at* 200 *V each cell represents the position of the macro-pixel on the sensor PS_p_light_std*_2_15_351136.

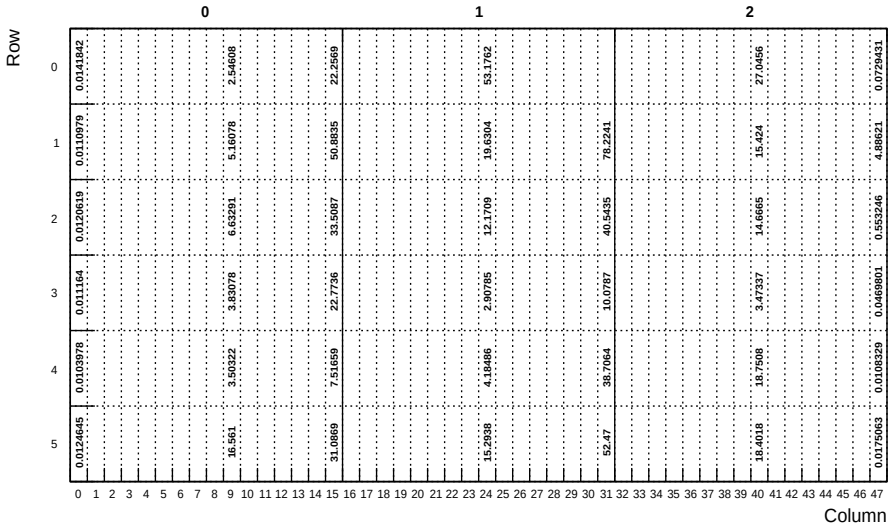

Figure 4.53: *Matrix of Current with fixed Voltage at* 200 *V each cell represents the position of the macro-pixel on the sensor.*$PS\_p\_light\_std\_2\_15\_351136$.

$PS\_p\_light\_std\_9\_1\_351137$ (Variant 4)

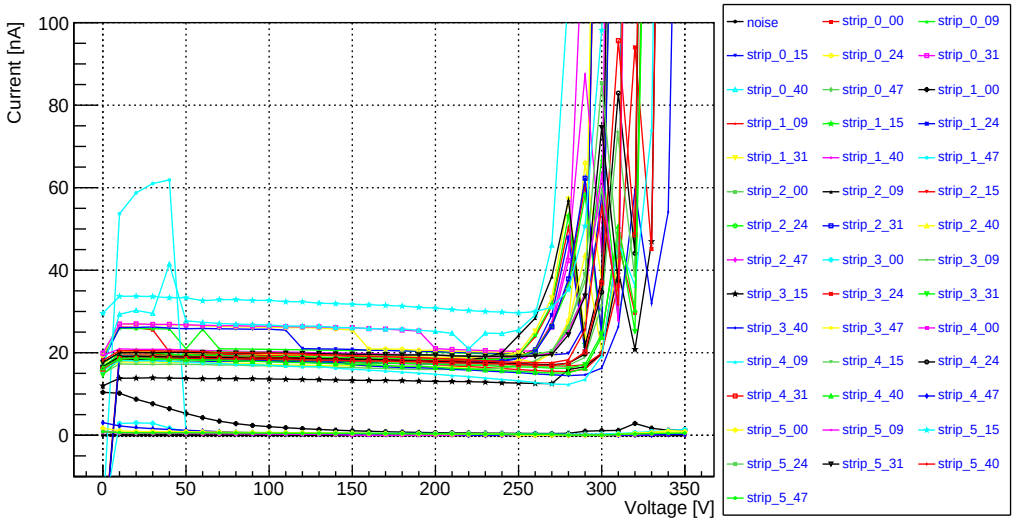

Figure 4.54: *IV strip scan for sensor* $PS\_p\_light\_std\_9\_1\_351137$.

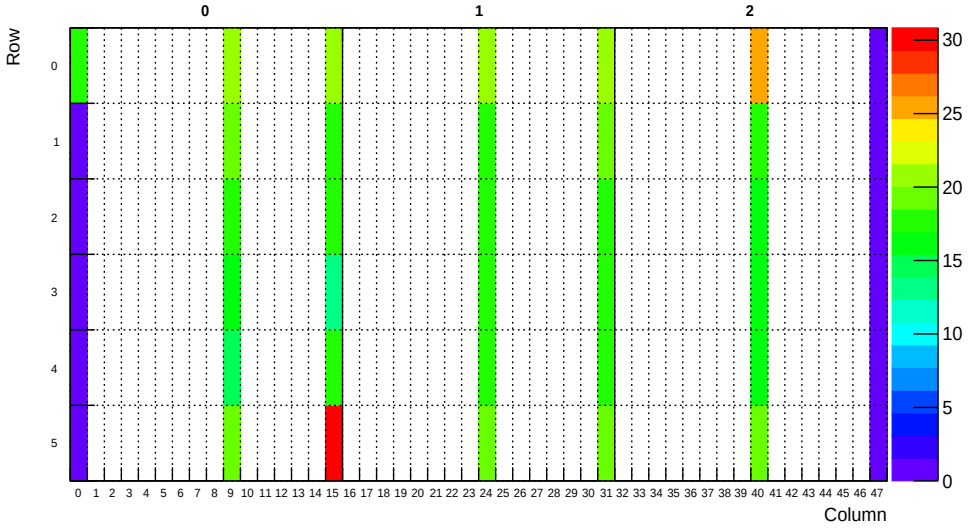

Figure 4.55: *Colored matrix of Current with fixed Voltage at* 200 *V each cell represents the position of the macro-pixel on the sensor* $PS\_p\_light\_std\_9\_1\_351137$.

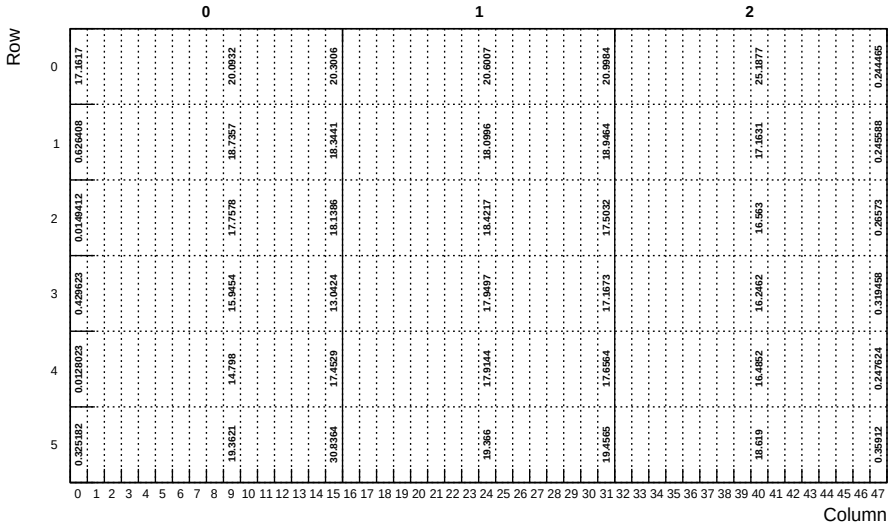

Figure 4.56: *Matrix of Current with fixed Voltage at* 200 *V each cell represents the position of the macro-pixel on the sensor.*$PS\_p\_light\_std\_9\_1\_351137$.

Chapter 5

Conclusion

Electrical characterization is an important procedure for the optimal development and the quality assurance of the silicon sensors for the Phase -II upgrade. Though this procedure electrical parameters such as the capacitances (Inter-strip,Backplane) the Resistances (Inter -strip,Rbias) as well as the Leakage current are measured. These parameters are of great importance since they influence the signal to noise ratio and the overall performance of the detectors. The sensors should be very tolerant to radiation with increased granularity and reduced material. This means the materials,the processing procedure and the geometry of each sensor should be chosen very carefully. The research and development for the silicon sensors of the CMS Tracker of phase -II has been started 10 years ago and is still on going.

The silicon sensors for the CMS Tracker will be produced in industry from suitable producers. The qualification of suitable vendors is ongoing at the time. The final selection of the design, the materials, the vendor will depend on the efficiency of the detectors in order to fulfill the requirements for Phase -II upgrade as well as ,the costs and the capabilities for this sensors to be produced in a large scale.

Before mounted into modules the quality of each sensor has to be approved. The quality assurance of the sensors is contacted in 4 stages VQC vendor quality control, SQC sensor quality control, PQC process quality control,IT irradiation tests. VQC is done by the producer while SQC, PQC and IT are contacted by the CMS collaboration at qualified centers. Electrical characterization is a part of these stages.

This master thesis is a part of a more general procedure in order to organize and upgrade the laboratory of detector instrumentation of NCSR Demokritos in order to become a SQC or PQC center.

The measurements that were performed was CV,IV on diode test structures, Backplane Capacitance , Interstrip Capacitnce , Total Capacitance and Bias Resistance on baby sensors, these are mini sensors that resembles the actual 2S sensors but with fewer strips and also total current and macro -pixel currents of the PS -p light sensors which is also made for test proposes and resembles the actual larger PS -p sensors. The results tested in Demokritos show a good quality and in conformity with specifications.

Bibliography

[1] S.M. Sze and K.K. Ng. *Physics of Semiconductor Devices*. Wiley, 2006. 10, 22, 24, 29, 30, 32, 98

[2] G Yepifanov. *Physical Principles of Microelectronics*. Mir Publishers, Moscow, 1974. 10, 11, 22

[3] H. Spieler. *Semiconductor Detector Systems*. Series on Semiconductor Science and Technology. OUP Oxford, 2005. 11, 12, 18, 50, 51, 52

[4] H. Xiao. *Introduction to Semiconductor Manufacturing Technology*. Prentice Hall, 2001. 12, 14

[5] G. Lutz. *Semiconductor Radiation Detectors: Device Physics*. Accelerator Physics. Springer Berlin Heidelberg, 2001. 14, 16, 17, 22, 30, 51

[6] Manfred Krammer. Silicon detectors, 2010. 14, 15

[7] W.R. Leo. *Techniques for Nuclear and Particle Physics Experiments: A How-to Approach*. Springer, 1994. 18

[8] P G Rancoita. Silicon detectors and elementary particle physics. *Journal of Physics G: Nuclear Physics*, 10(3):299, 1984. 20

[9] Straggling functions in silicon . http://meroli.web.cern.ch/meroli/lecture_stragglingfunction.html. Accessed: 2017-02-22. 21

[10] C. Leroy and P.G. Rancoita. *Silicon Solid State Devices and Radiation Detection*. World Scientific Publishing Company, 2012. 22, 29

[11] Frank Hartmann. Evolution of Silicon Sensor Technology in Particle Physics. *Springer Tracts Mod. Phys.*, 231:1–204, 2009. 23, 27, 29, 31, 36, 38, 39, 41, 42, 43, 45, 46, 47, 53, 54, 55, 56, 57, 97

[12] W. Shockley and W. T. Read. Statistics of the Recombinations of Holes and Electrons. *Physical Review*, 87:835–842, September 1952. 29

[13] Shockley Sah, Noyce. Carrier Generation and Recombination in P-N Junctions and P-N Junction Characteristics. *Physical Review*, 45:1228 – 1243, September 1957. 29

[14] A Chilingarov. Temperature dependence of the current generated in si bulk. *Journal of Instrumentation*, 8(10):P10003, 2013. 29

[15] SIMON RAMON. Currents induced byelectronmotion. *Proceedings of the I.R.E*, 27:584–585, 1939. 38

[16] Bortoletto Koybasi, Bolla. Guard Ring Simulations for n-on-p Silicon Particle Detectors. *Physical Review*, 57:2978 – 2986, October 2010. 41

[17] R. Turchetta. Spatial resolution of silicon microstrip detectors. *Nuclear Instruments and Methods in Physics Research A*, 335:44–58, October 1993. 44

[18] M Boronat, C Marinas, A Frey, I Garcia, B Schwenker, M Vos, and F Wilk. Physical limitations to the spatial resolution of solid-state detectors. pages 1–6, 2013. 44

[19] Yuan-hann Chang, E Chen, Suen R Hou, and Willis T Lin. A study of the charge cluster characteristics and spatial resolution of a silicon microstrip detector. 363:538–544, 1995. 44

[20] A E Chen and W T Lin. Study of energy straggling and multiple scattering in silicon microstrip detectors. 386(96):186–192, 1997. 44

[21] A Chilingarov. Temperature dependence of the current generated in si bulk. *Journal of Instrumentation*, 8(10):P10003, 2013. 45

[22] N. Demaria et al. New results on silicon microstrip detectors of {CMS} tracker. *Nuclear Instruments and Methods in Physics Research Section A: Accelerators, Spectrometers, Detectors and Associated Equipment*, 447(1–2):142 – 150, 2000. 46, 47

[23] E. Barberis, N. Cartiglia, C. LeVier, J. Rahn, P. Rinaldi, H.F.-W. Sadrozinski, R. Wichmann, T. Ohsugi, Y. Unno, H. Miyata, N. Tamura, and K. Yamamoto. Capacitances in silicon microstrip detectors. *Nuclear Instruments and Methods in Physics Research Section A: Accelerators, Spectrometers, Detectors and Associated Equipment*, 342(1):90 – 95, 1994. 46

[24] S. Braibant et al. Investigation of design parameters for radiation hard silicon microstrip detectors. *Nucl. Instrum. Meth.*, A485:343–361, 2002. 47, 48

[25] Laura Borrello, Alberto Messineo, Ettore Focardi, and Anna Macchiolo. Sensor Design for the CMS Silicon Strip Tracker. Technical Report CMS-NOTE-2003-020, CERN, Geneva, Aug 2003. 47

[26] L. Bellucci. Silicon detector developments for {CMS}. *Nuclear Instruments and Methods in Physics Research Section A: Accelerators, Spectrometers, Detectors and Associated Equipment*, 462(1–2):243 – 248, 2001. BEAUTY2000, Proceedings of the 7th Int. Conf. on B-Physics at Hadron Machines. 47

[27] P. Bloch, Y. H. Chang, A. E. Chen, A. Cheremukhin, N. Egorov, A. Go, S. Golubkov, I. Golutvin, S. R. Hou, K. Konjkov, Y. Kozlov, A. Kyriakis, W. T. Lin, D. Loukas, A. Markou, J. Mousa, A. Peisert, A. Sidorov, E. Tsoi, N. Zamiatin, and E. Zubarev. Silicon sensors for the CMS preshower detector. *Nuclear Instruments and Methods in Physics Research, Section*

A: Accelerators, Spectrometers, Detectors and Associated Equipment, 479(2-3):265–277, 2002. 48

[28] CMS Silicon Pixels. http://cms.web.cern.ch/news/silicon-pixels. Accessed: 2017-02-22. 49

[29] Enric Cabruja, Marc Bigas, Miguel Ullan, Giulio Pellegrini, and Manuel Lozano. Special bump bonding technique for silicon pixel detectors. *Nuclear Instruments and Methods in Physics Research Section A: Accelerators, Spectrometers, Detectors and Associated Equipment*, 576(1):150 – 153, 2007. Proceedings of the 8th International Workshop on Radiation Imaging Detectors. 49

[30] David J Griffiths. *Introduction to elementary particles; 2nd rev. version*. Physics textbook. Wiley, New York, NY, 2008. 59

[31] Stadard Model. https://upload.wikimedia.org/wikipedia/commons/archive/0/00/20130221160757!Standard_Model_of_Elementary_Particles.svg. Accessed: 2017-02-22. 60

[32] F. Gianotti, M. L. Mangano, T. Virdee, et al. Physics potential and experimental challenges of the lhc luminosity upgrade. *The European Physical Journal C - Particles and Fields*, 39(3):293–333, 2005. 61

[33] Burkhard Schmidt. The high-luminosity upgrade of the lhc: Physics and technology challenges for the accelerator and the experiments. *Journal of Physics: Conference Series*, 706(2):022002, 2016. 61

[34] Lyndon Evans and Philip Bryant. Lhc machine. *Journal of Instrumentation*, 3(08):S08001, 2008. 62, 63

[35] Esma Anais Mobs. The CERN accelerator complex. Complexe des accélérateurs du CERN, Oct 2016. General Photo. 62

[36] The HL-LHC project. http://hilumilhc.web.cern.ch/about/hl-lhc-project. Accessed: 2017-02-22. 64

[37] P La Rocca and F Riggi. The upgrade programme of the major experiments at the large hadron collider. *Journal of Physics: Conference Series*, 515(1):012012, 2014. 64, 65

[38] CMS Tracker. https://cms-docdb.cern.ch/cgi-bin/PublicDocDB/RetrieveFile?docid=11514&version=1&filename=cms_120918_03.png. Accessed: 2017-02-22. 65

[39] Tranverse slice through CMS. https://twiki.cern.ch/twiki/bin/view/CMSPublic/WorkBookCMSExperiment. Accessed: 2017-02-22. 66

[40] A. Affolder. The cms silicon strip tracker: Design and production status. *Nuclear Physics B - Proceedings Supplements*, 150:118 – 123, 2006. 67

[41] CMS Tracker. http://inspirehep.net/record/850264/files/fig_cmstracker.png. Accessed: 2017-02-22. 67

[42] CMS Tracker One Quarter. https://inspirehep.net/record/1255308/files/CMS2Dtracker.png. Accessed: 2017-02-22. 68

[43] S. Chatrchyan et al. The CMS Experiment at the CERN LHC. *JINST*, 3:S08004, 2008. 68

[44] M. Bartók. Simulation of the dynamic inefficiency of the cms pixel detector. *Journal of Instrumentation*, 10(05):C05006, 2015. 69

[45] M.M Angarano. The silicon strip tracker for {CMS}. *Nuclear Instruments and Methods in Physics Research Section A: Accelerators, Spectrometers, Detectors and Associated Equipment*, 501(1):93 – 99, 2003. Proceedings of the 10th International Workshop on Vertex Detectors. 69, 70

[46] CMS Tracker. http://cms.web.cern.ch/news/tracker-detector. Accessed: 2017-02-22.

[47] D Contardo, M Klute, J Mans, L Silvestris, and J Butler. Technical Proposal for the Phase-II Upgrade of the CMS Detector. Technical Report CERN-LHCC-2015-010. LHCC-P-008. CMS-TDR-15-02, Cern, Geneva, Jun 2015. Upgrade Project Leader Deputies: Lucia Silvestris (INFN-Bari), Jeremy Mans (University of Minnesota) Additional contacts: Lucia.Silvestris@cern.ch, Jeremy.Mans@cern.ch. 71, 72, 73, 74, 77, 78

[48] J. Brooke. Performance of the CMS Level-1 Trigger. *PoS*, ICHEP2012:508, 2013. 72

[49] A Tapper and Darin Acosta. CMS Technical Design Report for the Level-1 Trigger Upgrade. Technical Report CERN-LHCC-2013-011. CMS-TDR-12, Cern, Jun 2013. 72

[50] CMS collaboration. CMS Technical Design Report for the Phase-2 Tracker Upgrade. Technical report, CERN, Geneva, 2017. 75, 76, 77, 79, 80

[51] G. Hall, M. Pesaresi, M. Raymond, D. Braga, L. Jones, P. Murray, M. Prydderch, D. Abbaneo, G. Blanchot, A. Honma, M. Kovacs, and F. Vasey. Cbc2: A {CMS} microstrip readout {ASIC} with logic for track-trigger modules at hl-lhc. *Nuclear Instruments and Methods in Physics Research Section A: Accelerators, Spectrometers, Detectors and Associated Equipment*, 765:214 – 218, 2014. 78

[52] A Dierlamm. Silicon sensor developments for the cms tracker upgrade. *Journal of Instrumentation*, 7(01):C01110, 2012. 82

[53] G Auzinger. Silicon sensor development for the cms tracker upgrade. *Journal of Instrumentation*, 6(10):P10010, 2011. 82

[54] S. Kavadias, K. Misiakos, and D. Loukas. Calculation of pixel detector capacitances through three dimensional numerical solution of the laplace equation. *IEEE Transactions on Nuclear Science*, 41(2):397–401, Apr 1994. 88, 108

[55] Panagiotis Assiouras. Program development in Java for the fast calculation of capacitances in silicon detectors for the upgrade of the tracker detector of the C.M.S. experiment in Super L.H.C., 2015. 88, 108

[56] E. H. Nicollian and J.R. Brews. *MOS (metal oxide semiconductor) physics and technology.* Metal Oxide Semiconductor Physics and Technology. Wiley, 1982. 99